A Search for the Large Angular Scale Polarization of the Cosmic Microwave Background

by

Brian Keating

B.Sc. Case Western Reserve University, 1993
Sc.M., Brown University, 1995

Dissertation

Submitted in partial fulfillment of the requirements for the
Degree of Doctor of Philosophy
in the Department of Physics at Brown University
Providence, Rhode Island

May 2000

Abstract of "A Search for the Large Angular Scale Polarization of the Cosmic Microwave Background," by Brian Keating, Ph.D., Brown University, May 2000

The Cosmic Microwave Background (CMB) is one of the three observational pillars of modern cosmology, along with the Hubble Expansion Law and the measured abundances of the light elements. Being the fossil radiation from the Big Bang, it probes the conditions of the early universe. Three properties are necessary to fully characterize the CMB: its spectrum, spatial isotropy, and polarization. The first two properties have been measured, whereas the polarization state of the CMB remains undetected. Detection of, or an improved upper limit on, the polarization of the CMB at large scales holds great promise for the determination of several fundamental properties of the standard cosmological model, such as the ionization history of the Universe and the contribution of gravitational waves to the spectrum of primordial perturbations. Most models predict that the magnitude of the polarization of the CMB at large angular scales is less than 1μK. This is at least an order of magnitude below both the large scale anisotropy level of the CMB, as well as the best existing upper limits on its polarization. In this thesis I calculate the magnitude of the CMB polarization in various cosmological scenarios, and outline the fundamental challenges to measuring these signals. Following, I describe the design of the POLAR (Polarization Observations of Large Angular Regions) experiment, which is the first dedicated polarimeter to study the CMB in more than a decade. POLAR is a ground-based, centimeter-wavelength correlation polarimeter designed to detect the polarization of the CMB at 28, 31, & 33 GHz. POLAR is the first correlation polarimeter ever used for CMB work and has the widest bandwidth of any correlation radiometer ever used for investigations of the CMB. POLAR has been constructed and is currently acquiring data at the University of Wisconsin – Madison.

This dissertation by Brian Keating is accepted in its present form by
the Department of Physics as satisfying the
dissertation requirement for the degree of
Doctor of Philosophy

Date ....
Peter Timbie, Director

Recommended to the Graduate Council

Date ....
Robert Brandenberger, Reader

Date ....
Gregory Tucker, Reader

Approved by the Graduate Council

Date ....
Peder J. Estrup
Dean of Graduate School and Research

Acknowledgments

So many people have helped me, both personally and professionally, in my years of schooling. I have been honored to know each and every one of you, and I have benefited enormously.

First of all to my advisor, I am reminded of the old proverb that states: "When the student is ready, he will find his teacher." I am quite lucky to have found Peter Timbie. Peter possesses so many gifts – it's difficult to list all of them here. He has the gift of powerful physical insight when there are problems to solve. He has patience when things go wrong, a sense of humor when things *really* go wrong, and most of all: the integrity, compassion, and soul needed to lead young people today. Peter, thanks for putting up with me for these 6 years and turning me into a physicist. And thanks for "letting" me beat you in basketball *so* many times.

I've been privileged to have known two men who have been wonderful mentors throughout my brief career. Prof. Alex Polnarev taught me most of what I know about theoretical physics and cosmology. Continuing the traditions passed on by his mentor Y.A. Zel'dovich, he also taught me that "Nine women cannot have a baby in one month!" Alex, I'm honored to be your "Cosmological Son". Dr. Lucio Piccirillo was there to solve the hard problems that were essential to the success of POLAR. In the lab he is a wizard – "The Master" takes the *cry* out of cryogenics, and puts it into chess – thanks for *never* letting me win. Thanks, also, for giving me the tools I needed to get to the next level as an experimentalist.

Next we come to the folks who helped shape POLAR. First of all is my little buddy, Nate (Dogg) Stebor. Nate, thanks for working so hard, for so long. Thanks for catching my mistakes before they became disasters, doing and re-doing so many things without complaint. Thanks for listening to me sing off-key for hours in the lab, and thanks for putting up with my (mostly unintentional) attempts to electrocute you. Chris (Codfish) O'Dell has built a great many things that have improved the quality of POLAR's life immensely. Sorry I made you re-build the ground screen ten times just to increase its length by a few microns. I leave POLAR in your skilled hands.

Several undergraduates have helped in the development of POLAR. At UW, Kip Hyatt designed and built the outer ground screens – an engineering feat that would make the ancient Egyptians tremble. Jessie Sincher made several of the figures in this thesis, and has been a good sport in the lab. Back at Brown, there were two undergraduates who helped define the direction POLAR would later take. Brendan Crill helped construct the "Proto-Polarimeter" which allowed numerous systematics to be diagnosed, and performed the calculations which estimated the polarization of the atmosphere. Melvin Phua continued in Brendan's shoes, refining the data acquisition technique, building many components of the original polarimeter, and in general, was a great help to me during in-lab testing.

I have also benefitted from innumerable conversations with the "New Guard" Theorists: Wayne Hu, Arthur Kosowsky, and Matias Zaldarriaga. Cosmology is in good hands with you three gentlemen. Josh GundersEn, cosmology's only Rabid-Hacker Packer-Backer built the $K_{\rm a}$ Band feedhorn, and participated in countless discussions on the status and future of POLAR. Ed Wollack – The Hardest Working Man in Microwaves – bailed me out on so many occasions. His energy, insight, and skill motivate me. Ed, I hope someday I can repay you!

Grant (Wingman) Wilson is an interesting character. He is a throwback to the old-school of experimental cosmologists. Well versed in experimental techniques, *and* theory, he has done a great deal for POLAR and for me personally. By asking the hard questions such as "Are you *sure* you want to do that???" and "You *can't* be serious!?", he has helped define the shape of POLAR from the very beginning.

Back at UW there were two people who made my life as a grad student much more enjoyable. Donna Garcia is a wizard – she keeps our group together with her knowledge, organization, and cheerful attitude. Lee Potratz and entire the Staff of the Physics Instrument Shop at UW turn ideas into metal. Lee was essential to the success of POLAR. He taught me a great deal about machining, motorcycles, and life in the Badger State.

Now to my friends who have supported me much more than they know. My oldest friend, Shane Diekman, was always there for me when I needed him. Erica Cushin has been the sunshine that has always brightened my spirits. My friends from Case Western: Joe Scharpf and Adam Greenberg make me proud. Jeff (Jefe) Tseng is my kindred (Taiwanese) spirit. Back at home in Purdys, Tom Gustinis and the entire Freeman family have always treated me right. At Brown two guys kept me entertained for many years. Matt Parry is proof that theoretical cosmology is in great shape. And, finally, to my Soul Brother, Stephon Alexander: your passion, insight, strength, and wisdom inspire me to be a better physicist.

"Think where man's glory most begins and ends, and say my glory was I had such friends." -W.B. Yeats

Dedication

This thesis is dedicated to my first and best teachers: my family, without whom I'd be lost...

My Dad Raymond's sense of humor and intellect have always been great resources for me. He has consistently injected precision doses of wisdom and wit, whenever I have needed them.

I'd be nothing without my little brothers Nick and Chris. They make me laugh (mostly) and cry (rarely), but I am so proud of them. Just knowing they are in the world fills my life with joy.

My older brother Kevin is my hero; my rock. He is my best friend, my inspiration, my guardian. He made me what I am.

My mother Barbara taught me everything I know about life. Words cannot capture what she means to me – I owe her everything. "If I could find a twinkling star, one half so wondrous as you are, that star would be, like my heart and me – dedicated to you."

Contents

List of Figures

List of Tables

Introduction

The 2.7K Cosmic Microwave Background (CMB) radiation is a vital probe of all modern cosmological theories. This radiation provides a "snapshot" of the epoch at which radiation and matter decoupled, approximately 300,000 years after the Big Bang, and carries the imprint of the ionization history of the universe. This information has been used to tightly constrain theories of cosmological structure formation, and has ushered in the era when "cosmological accuracy" is no longer a pejorative term.

The CMB was definitively identified in 1965 by Penzias and Wilson [1]. The three defining characteristics of this relict radiation are: its spectrum, spatial anisotropy, and polarization. Since that time, numerous experiments have characterized its spectrum and spatial anisotropy:

Spectral Measurements

The *COBE* Far-Infrared Absolute Spectrophotomer (FIRAS) has determined the thermodynamic blackbody temperature of the CMB to be 2.725 ± 0.002 K [2]. However, since this instrument probes the CMB over a limited spectral range ($\nu \sim 10$ to 600 GHz), to probe the blackbody nature of the CMB over the widest possible range of frequencies we must also consult supplemental experimental evidence from lower frequency measurements, see *e.g.* [3]. These lower frequency measurements do more than simply confirm

the results of FIRAS, they serve to constrain deviations from the Planck spectrum to (nearly) negligible levels. Most notably, these low-frequency measurements constrain the so-called "chemical potential" distortion, which results in a decrement of the Planck spectrum at low frequencies. Photons, being bosons, have a number density in equilibrium of $n = \frac{1}{e^{h\nu/k_bT+\mu_o}-1}$. The Planck spectrum sets $\mu_o = 0$, but the existence of a non-zero μ_o can not be ruled-out at present. The best 95% confidence upper-limits suggest that $|\mu_o| < 4 \times 10^{-4}$ [4].

At frequencies near the peak of the Planck spectrum a *Compton-y* distortion might be expected from Compton scattering of photons by electrons heated by a hypothesized energy release prior to decoupling at a redshift of $z \sim 10^5$. This type of distortion has a characteristic spectral signature in that the hot electrons increase the frequency of scattered photons while conserving photon number density. The y-factor parameterizes the temperature difference between the hot electrons and cooler photons: $y = \int d\tau k_b(T_e - T_{\rm cmb})/m_e c^2$,where T_e is the kinetic temperature of the electrons. The result of a Compton-y distortion is a spectral decrement below the peak frequency of the CMB, and a spectral increment above the peak. The best upper limits on the Compton-y factor suggest $|y| < 1 \times 10^{-5}$ [5],[6].

Anisotropy Measurements

Large Scale Anisotropy

There are at present a plethora of detections of anisotropy of the CMB, the largest of which is the dipole anisotropy resulting from the earth's proper motion with respect to the nearly isotropic Planckian spectrum mentioned above. This effect is non-cosmological, so it is never included in models which predict the anisotropy of the CMB. Expanding the observed temperature pattern on the celestial sphere into spherical harmonics we

have: $\frac{\Delta T}{T_{cmb}}(\theta,\phi) = \sum_{\ell,m} a_{\ell,m} Y_{\ell,m}$. The first cosmologically significant anisotropy is the *quadrupole*, with an expectation value of $C_2 = T_{cmb}^2 \langle |a_{2,m}|^2 \rangle = T_{cmb}^2 \sqrt{\frac{1}{5}\sum_{m=-2}^{m=+2} |a_{2,m}|^2}$. The RMS quadrupole is used to normalize the CMB power spectrum. The amplitude of the power spectrum is defined to be:

$$Q_{rms} = \sqrt{\frac{5C_2}{4\pi}}.$$

Since the angle subtended on the celestial sphere by a spherical harmonic multipole ℓ scales as $\theta \sim \pi/\ell$, the quadrupole anisotropy is a large-scale anisotropy ($\theta \simeq 90^\circ$. The best limits on Q_{RMS} come from the *COBE* DMR experiment, which at 95% confidence are $4\mu K < Q_{RMS} < 28\mu K$, where the relative imprecision is attributed primarily to contamination by galactic emission [7]. In the angular range $90^\circ < \theta < 10^\circ$, the DMR also provides the most precise measurement of temperature anisotropy. On 10° scales, COBE detects $\Delta T \simeq 30\mu$K [8].

Intermediate and Small Scale Anisotropy

There has been an intense effort to measure the anisotropy of the CMB at smaller scales because the fluctuations on these scales are expected to bear the imprint of microphysical processes occuring in the early universe prior to and during decoupling. All of these experiments are either ground or balloon based. We refer the reader to the recent reviews [7] and [9] for current results.

What About Polarization?

Polarization of the CMB has received comparatively little experimental attention, despite its fundamental nature. The anisotropy and polarization depend on the primordial power spectrum of fluctuations as well as the ionization history of the universe in different

ways. As I will demonstrate in Chapter 2, a detection of polarization would complement the detections of anisotropy by facilitating the reconstruction of the initial spectrum of perturbations as well as the ionization history of the universe.

The magnitude and spatial distribution of polarization is determined by factors such as: the source of the CMB anisotropy, the density parameter Ω_o, the baryon content of the universe Ω_B, the Hubble constant H_o, and the ionization history of the universe. CMB polarization is paticularly sensitive to the ionization history of the universe, which includes the duration of recombination and the epoch of reionization. The detection of, or a further constraint on, the polarization of the CMB has the potential to dramatically enhance our understanding of the pre-galactic evolution of the universe.

Similar to the CMB anisotropy power spectrum, the polarization power spectrum contains information on all angular scales. Large angular scales (larger than $\simeq 1^\circ$) correspond to regions on the last scattering surface which were larger than the causal horizon at $z \simeq 1000$. In the absence of reionization, these scales were affected *only* by the long wavelength modes of the primordial power spectrum. This region of the anisotropy power spectrum was measured by the *COBE* DMR, and establishes the normalization for models of large scale structure formation. Similarly, measurements of polarization at large angular scales will normalize the entire polarization power spectrum. Because the anticipated signal size is small at all angular scales, polarization measurements face more formidable challenges than anisotropy measurements.

The experiment described in this thesis measures polarization signals on large angular scales. While these signals may be weaker than signals on small scales, the design of a large angular scale measurement is comparatively simple and compact, with potentially lower susceptibility to sources of systematic error. A detection, or improved upper limit, at *large*

angular scales is a natural first step towards probing the polarization power spectrum on *all* angular scales. In this regard, the present state of the polarization field is reminiscent of the anisotropy field a decade ago.

In this thesis we will review theoretical arguments which suggest that the ratio of polarization to anisotropy should be in the range 0.1% to 10%, at large angular scales. The best current upper limits on polarization are comparable to the measured anisotropy level itself (see Table 1). Measurements of anisotropy, by *COBE*, and other experiments on the level of $\Delta T/T_{\rm cmb} \simeq 1 \times 10^{-5}$ indicate the required level of sensitivity to polarization must be at least $\Delta T/T_{\rm cmb} \leq 1 \times 10^{-6}$. Thus, to obtain new non-trivial information, either a positive detection, or an improved upper limit capable of discriminating between different cosmological scenarios, necessitates extremely precise measurements.

Current detector technology is capable of achieving the required level of sensitivity. However, in addition to achieving high sensitivity it is essential to discriminate the polarization from systematic effects, such as non-cosmological astrophysical sources of polarized radiation. Space-based missions, such as MAP[10] and Planck Surveyor [11] will produce full-sky anisotropy maps, and are expected to achieve the required sensitivity level to measure polarization as well. The projected sensitivity levels will allow for per-pixel detections of anisotropy with signal-to-noise ratios: SNR > 1. The polarization maps from these missions, however, are expected to have SNR< 1 for each beam-sized pixel, and will be of lower resolution than the anisotropy maps. Fortunately, polarization observations are also possible from the ground; as we will demonstrate, polarized atmospheric emission is expected to be negligible.

This thesis describes an ongoing, ground-based polarization experiment, Polarization Observations of Large Angular Regions (POLAR), optimized to measure CMB polariza-

tion at 7° scales, for ~ 36 pixels. The design incorporates many techniques developed for previous anisotropy and polarization experiments, from the ground, balloons, and space.

In Chapter 2 we review the theory of CMB polarization, which motivates POLAR's experimental design. We describe the instrument in Chapter 4, and the calibration of POLAR in Chapter 5. In Chapter 7 we focus our attention on a significant challenge to the detection of the polarization of the CMB: the discrimination of CMB polarization from polarized foreground sources. Chapter 8 presents an overview of our observing strategy, which is designed to minimize the time required to detect a cosmological signal. In Chapter 9 we present the preliminary analysis of the initial observing run of POLAR. Chapter 10 summarizes the results obtained to date, along with a formalism for comparing future data sets with temperature anisotropy data, and calculating estimates of the epoch of reionization. Finally, we speculate on the conclusions which could be drawn from a detection of CMB polarization, as well as future directions and goals of the POLAR campaign.

Table 1: Experimental Limits on Linear Polarization (95% Confidence Level)

Reference	Frequency (GHz)	Sky Coverage Dec=δ	Angular Scale	Limit $\frac{T_{\rm pol}}{T_{\rm cmb}}$
Penzias & Wilson 1965 [1]	4.0	scattered	—	0.1
Caderni *et al.* 1978 [12]	100−600	near galactic center	$0.5° < \theta < 40°$	0.001−0.01
Nanos 1979 [13]	9.3	$\delta = +40°$	15°	6×10^{-4}
Smoot & Lubin 1979[14]	33	$\delta = 38°, 53°, 63°$	7°	3×10^{-4}
Lubin & Smoot 1981 [15]	33	$\delta = -37°$ to $+63°$	7°	6×10^{-5}
Partridge *et al.* 1997 [16]	8.4	$40'^2$ at $\delta = +43.5°$	$1'$	1.1×10^{-5}
Wollack *et al.* 1993 [17]	$26 - 36$	$\sim 10°$ Cap around NCP	0.5°	9×10^{-6}
Netterfield *et al.* 1996 [18]	$26 - 46$	$\sim 10°$ Cap around NCP	0.5°	6×10^{-6}

Chapter 1

Preliminaries

This chapter is intended to serve as a reference for several chapters in this thesis. The results quoted here are, in general, not derived, and the intent is simply to compile a small repository of information which will be quoted throughout this thesis. The reader may feel free to refer to this chapter only by necessity, or skip it altogether.

1.1 Radio Astronomy Fundamentals

We first summarize some results which outline our observables and their connection to our measurement technique.

1.2 Radiometry Basics

A radio source observed in direction θ can be characterized by its *Brightness*, with units of [W/m^2/Hz/sr]. The brightness, $B_\nu(\theta)$, of a source is related to its *detected power* in an area element dA via:

$$P = \int B_\nu(\theta) \cos\theta \, d\Omega \, dA \, d\nu, \tag{1.1}$$

where $d\Omega = \sin\theta d\theta d\phi,\ dA,\ d\nu$ are infinitesimal solid angle, area, and frequency elements, respectively, and θ is the angle between the normal to the area element and the line-of-sight.

The source's *Flux Density* is defined by:

$$S_\nu = \int B_\nu(\theta) d\Omega \tag{1.2}$$

The unit of S_ν is the *Jansky* $\equiv$ Jy $= 10^{-26}$ W/m^2/Hz.

For a *blackbody*, the brightness is a function of thermodynamic temperature T:

$$B_\nu(T) = \frac{2h\nu^3}{c^2} \frac{1}{e^{\frac{h\nu}{kT}} - 1}, \tag{1.3}$$

which has a maximum brightness at a frequency $\frac{\nu_{max}}{GHz} = 58.789(\frac{T}{K})$. The number density of photons in a blackbody radiation field is $2.03 \times 10^7 T^3 m^{-3}$ [19]. At frequencies much greater than ν_{max}, we obtain the Wien Law: $B_\nu(T) = \frac{2h\nu^3}{c^2} e^{-h\nu/kT}$. In the *Rayleigh-Jeans* region of the spectrum we have

$$h\nu \ll kT \Rightarrow B_{RJ}(\nu, T) = \frac{2\nu^2}{c^2} kT.$$

From this equation we obtain the definition of *Brightness Temperature*:

$$T_B = \frac{c^2 B_\nu}{2k\nu^2}. \tag{1.4}$$

From the definition of the brightness temperature, which is independent of the receiver, we obtain the *Antenna Temperature* which *is* dependent on the beam of the radio telescope. The antenna has a *peak-value normalized beam pattern*, $P(\theta)$ which results in an acceptance

solid angle of $\Omega = \int_0^{2\pi} P(\theta) d\Omega$. The *main beam* is defined as the solid angle, Ω_M, subtended by the portion of $P(\theta)$ between its first nulls. This results in a *main beam efficiency* factor of $\eta_b = \frac{\Omega_M}{\Omega}$. Then the antenna temperature is defined to be:

$$T_A = T_B \frac{\Omega_M}{\Omega}. \tag{1.5}$$

If a radio source fills the entire beam of a radio telescope and is optically thick[1] then we see that the antenna temperature will equal the thermodynamic temperature of the source. This fact is quite remarkable, for it suggests that if we could couple the radiation received from this distant source to a blackbody in our lab, the lab blackbody's temperature would *equal* the temperature of the distant source. In this way we can literally "take the temperature" of extremely distant objects.

One final concept is useful here; that of the antenna's *effective area*. A radio telescope antenna may have *zero* physical area, as in the case of an ideal dipole antenna, yet it is defined to have an effective area of:

$$A_e \Omega_M = n\lambda^2, \tag{1.6}$$

where, n is the number of spatial modes, λ is the wavelength of the radiation received by the antenna, and Ω_M is the main-beam solid angle[20][19]. For (diffraction-limited) measurements, $n = 1$ and $A_e \Omega = \lambda^2 = \frac{c^2}{\nu^2}$. The product $A_e \Omega_M$ is, in astronomical circles, known as the *throughput* or *etendue*. The concept of antenna temperature is useful since it implies a source of flux density S_ν will produce an antenna temperature of:

[1]Meaning that it is in bulk thermal equilibrium if it is a diffuse source, such as a cloud, and has an emissivity of unity.

$$T_A = \frac{S_\nu A_e}{2k_b}, \tag{1.7}$$

which is consistent with the conventional relationship between flux and area.

1.3 Emission and Absorption of Radiation by Matter

Here we present a brief, phenomenological, description of emission and absorption as it pertains to objects frequently observed in radio astronomical applications [20].

Emission

We first consider an emitting medium, with number density of emitting particles ρ, and *emission coefficient* j_ν (which is the energy emitted by a volume element $dV = drdA$ in the intervals $d\nu, d\Omega, dt$), which produces an infinitesimal brightness:

$$dB_\nu = \frac{1}{4\pi} j_\nu \rho dr e^{-\tau}, \tag{1.8}$$

per unit thickness of the medium, dr. The *optical depth*, τ, is defined to be:

$$\tau = \int_0^R \alpha\rho dr,$$

where $\alpha\rho$ is known as the *absorption coefficient*, with units of m^{-1}, and τ is optical depth which is dimensionless.

Absorption

Now consider a collimated beam of radiation traveling a distance dr through an absorbing medium. The brightness of the radiation after traversing a distance R through the medium is related to the initial brightness, B_o by:

$$B = B_o e^{-\int_0^R \alpha\rho dr} = B_o e^{-\tau}. \tag{1.9}$$

Combining both emission and absorption by a medium, we have that:

$$B_\nu = B_o e^{-\tau} + \frac{j_\nu}{\pi\alpha\rho}(1 - e^{-\tau}). \tag{1.10}$$

Kirchoff's Law states that, in equilibrium, we have:

$$\begin{aligned} dB &= 0 \\ \Rightarrow B &= \frac{j_\nu}{\pi\alpha} \end{aligned} \tag{1.11}$$

which relates brightness of an emitting and absorbing cloud to its bulk properties in thermodynamic equilibrium.

Absorption and Scattering: Extinction

The Boltzmann equation gives the relation between the input and output intensities of a collimated beam of radiation traveling an infinitesimal distance dr through an absorbing, emitting medium:

$$\frac{dB_\nu}{dr} = -\kappa_\nu B_\nu + j_\nu, \tag{1.12}$$

where the emission coefficient, j_ν, is the energy emitted by a volume element $dV = ds\, dA$ in the intervals $d\nu, d\Omega, dt$, and $\kappa_\nu B_\nu$ is the energy absorbed from a beam of specific intensity B_ν.

Extinction, denoted by Q_e, is the combination of absorption and scattering out of a collimated beam. Extinction is parameterized by $Q_e = \frac{s_\nu}{\sigma_d}$, where s_ν is the optical scattering cross-section, and σ_d is the geometric cross section of the scatterer. Q_e varies with index of refraction of the scatterer, approaching unity as the wavelength decreases to zero, and can become $\gg 1$ at wavelengths comparable to the dimension of the scatterer.

1.4 Thomson Scattering, Polarization, and the Stokes Parameters

The description of polarized radiation appears quite frequently in this thesis, both in the theoretical description of polarization of the CMB, and the experimental description of its detection. We choose to present a unified discussion prior to embarking on either course.

We start by considering a generally polarized[2] electromagnetic wave with angular frequency, ω:

$$\vec{\mathbf{E}} = E_{y0}\sin(\omega t - \delta_y)\hat{\mathbf{y}} + E_{x0}\sin(\omega t - \delta_x)\hat{\mathbf{x}}. \tag{1.13}$$

The polarization state of the wave is completely characterized by the Stokes parameters: I, Q, U, and V.

$$I_y = \langle E_{y0}^2 \rangle \tag{1.14}$$

$$I_x = \langle E_{x0}^2 \rangle \tag{1.15}$$

[2] *i.e.*, either circularly or linearly (or both)

$$I = I_y + I_x \tag{1.16}$$

$$Q = I_y - I_x \tag{1.17}$$

$$U = 2E_{y0}E_{x0}\cos(\delta_y - \delta_x) \tag{1.18}$$

$$V = 2E_{y0}E_{x0}\sin(\delta_y - \delta_x). \tag{1.19}$$

Physically, I is the total intensity of the radiation, and is always positive. The parameters Q and U quantify the linear polarization of the wave, and V quantifies the degree of circular polarization (when $V = 0$, the radiation is linearly polarized or unpolarized). The level of polarization is defined as $\Pi = \frac{\sqrt{Q^2+U^2+V^2}}{I}$, and the polarized intensity is $I_{\rm pol} \equiv \Pi \times I$.

Note that the Stokes parameters are defined in *intensity* $\equiv$ *brightness* units, whereas our experiment measures the *antenna temperature* of the incident radiation field. If we need to convert between the two we apply equations 1.4 and 1.5.

We now turn from the phenomenological description of polarization to its generation via photon-electron scattering. Thomson scattering is the low-energy limit of Compton scattering, differing due to the fact that a Thomson-scattered photon will have the same frequency before and after scattering. We will only discuss scattering of photons by electrons, not other charged particles.

The differential scattering cross-section for Thomson scattering gives the *intensity* of radiation scattered into solid angle $d\Omega$:

$$\frac{d\sigma}{d\Omega} = \frac{3\sigma_T}{8\pi}|\hat{\epsilon}' \cdot \hat{\epsilon}|^2, \tag{1.20}$$

where σ_T is the Thomson cross-section with units of m^2, and the vectors $\hat{\epsilon}'$ and $\hat{\epsilon}$

represent the incoming and outgoing polarizations, respectively. The Thomson cross-section $\sigma_T \propto r_e^2$, where r_e is the classical electron radius. We refer the reader to figure 1.1 for definitions of coordinates used in the scattering problem.

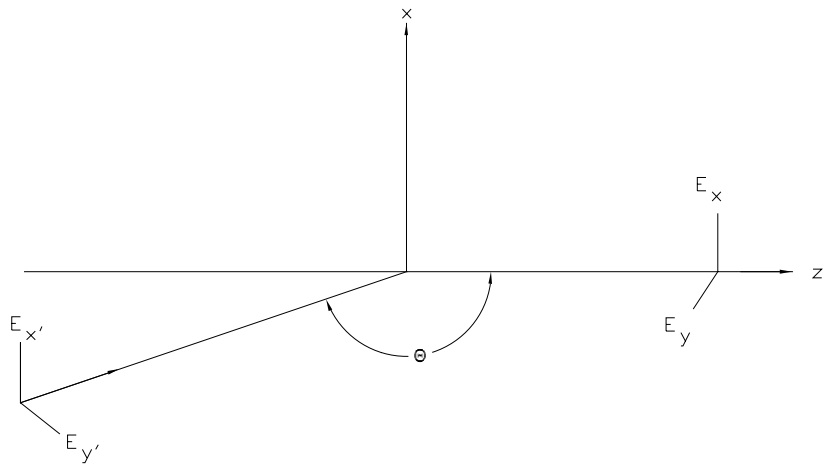

Figure 1.1: Thomson Scattering Geometry

Following Kosowsky [21], we consider an incident unpolarized plane wave of intensity I' which is subsequently scattered along the z-axis. From the scattering cross-section defined above we find that the Stokes parameters of the outgoing radiation are:

$$I = \frac{3\sigma_T}{8\pi} I'(1+\cos^2\theta) \tag{1.21}$$

$$Q = \frac{3\sigma_T}{8\pi} I' \sin^2\theta \tag{1.22}$$

$$U = 0, \tag{1.23}$$

where θ is the scattering angle. To determine the net polarization produced by an incident distribution $I'(\theta, \phi)$, we must integrate the above equations over all incoming and outgoing angles. We find, as expected, that there will now be a non-vanishing U:

$$\begin{aligned} I &= \frac{3\sigma_T}{16\pi} \int d\Omega \; I'(\theta, \phi)(1 + \cos^2 \theta) \\ Q &= \frac{3\sigma_T}{16\pi} \int d\Omega \; I'(\theta, \phi) \sin^2 \theta \cos 2\phi \\ U &= \frac{3\sigma_T}{16\pi} \int d\Omega \; I'(\theta, \phi) \sin^2 \theta \sin 2\phi. \end{aligned} \tag{1.24}$$

At this point, it is customary to expand $I'(\theta, \phi)$ into spherical harmonics, *viz*:

$$I'(\theta, \phi) = \sum_{\ell, m} a_{\ell, m} Y_{\ell, m}(\theta, \phi). \tag{1.25}$$

By the orthogonality of the spherical harmonics, we find from equations 1.24 and 1.25 that the resulting polarization is:

$$Q = \frac{3\sigma_T}{8\pi} \sqrt{\frac{\pi}{5}} a_{2,2} \tag{1.26}$$

$$U = \frac{3\sigma_T}{8\pi} \sqrt{\frac{\pi}{5}} a_{2,-2}, \tag{1.27}$$

which shows that it is the quadrupole content of the incident radiation field which determines the polarization produced.

1.5 Time and Frequency-Domain Relations

Both of the following subsections draw heavily from the excellent discussion given in Mc Donough and Whalen [22]. Results from these sections are used heavily throughout this thesis in many seemingly disparate discussions. A thorough understanding is required in order to connect the predictions of theory to the experimental observables.

1.5.1 Autocorrelation Function: ACF

We begin by considering a timestream, representing the voltage out of a detector, denoted by $x(t)$. The *expectation value* of $x(t)$ is: $\mathbf{E[x(t)]} = \int_{-\infty}^{\infty} \mathbf{x(t)p[x_t]dx_t}$, where $p[x_t]$ is the probability that $x(t) = x_t$ at time t.

Then the auto-correlation function (ACF) of $x(t)$ is defined to be:

$$R_x(t_1, t_2) = \mathbf{E[x(t_1)(x(t_2)]} \tag{1.28}$$

$$= \int_{-\infty}^{\infty} x_1 x_2 p(x_1, x_2; t_1, t_2) dx_1 dx_2. \tag{1.29}$$

If the process which generates the timestream is a *stationary* random process then $\mathbf{E[x(t)]} = \mathbf{m}$, the mean is a constant, as is the variance σ_x^2. In this case we can disregard the absolute times t_1 and t_2 in equation 1.29 and consider instead only the time difference between them, denoted by τ.

Then equation 1.29 becomes:

$$R_x(t_1, t_1 - \tau) = \int_{-\infty}^{\infty} x(t_1) x(t_1 - \tau) p[x(t_1), x(t_1 - \tau)] dx_{t_1} dx_{t_1 - \tau} \equiv R_x(\tau). \tag{1.30}$$

If $R_x(t_1, t_2) = R_x(t_1 - t_2)$ then the process is called *wide-sense* stationary. These definitions result in:

$$\sigma_x^2 = R_x(0) - m^2. \tag{1.31}$$

For a complex function $x(t)$ which is wide-sense stationary we have that:

$$R_x(\tau) = \lim_{T\to\infty} \left(\frac{1}{T}\right) \int_{-T/2}^{T/2} x(t)x^*(t-\tau)dt. \tag{1.32}$$

Note that from the definition of the ACF, $R_x(\tau) = R_x(-\tau)$. Similar definitions hold for the cross-correlation function ($\equiv R_{xy}$) of two timestreams $x(t)$ and $y(t)$, though we will not present these generalizations of equation 1.30 here.

We wish to emphasize here that, although we have been dealing in the time-domain, these results immediately generalize, for example, to functions of angle. As a toy example, let $x(\theta)$ be a scalar function of angle, on a small-enough portion of the sky which can essentially be treated as planar, or in this case, one-dimensional. Continuing with the toy example, let $x(\theta) = \cos k\theta$, then the ACF of $x(\theta)$ is:

$$R_x(\theta, \theta - \tau) = R_x(\tau) = \frac{1}{2}\cos(k\tau). \tag{1.33}$$

We see that a sinusoidal function on the sky produces a sinusoidal correlation function. This generic result will be useful when we discuss the auto and cross-correlation functions of cosmological observables, in Chapter 2, which are often assumed to be described by Gaussian random fields.

1.5.2 Frequency Domain Relations

A timestream $x(t)$ has a Fourier Transform:

$$X(i\omega) = \int_{-\infty}^{\infty} x(t) e^{-2\pi i \nu t} dt \tag{1.34}$$

as long as $\int_{-\infty}^{\infty} |x(t)| dt < \infty$. Of course this inequality does not hold for a timestream representing a physical process, such as the output from our detectors. Instead we relax this more-strict criterion, and instead require:

$$\lim_{T \to \infty} \left(\frac{1}{T}\right) \int_{-T/2}^{T/2} |x(t)|^2 dt < \infty,$$

which can usually be satisfied. In this case, we see that $x(t)/\sqrt{T}$ has a Fourier transform denoted by $X(\nu, d\nu)$, since in the limit that $T \to \infty$, we obtain an infinitesimal $\sqrt{d\nu}$. Usually, we are interested in the infinitesimal *power* contained in an infinitesimal frequency band, $d\nu$. This becomes:

$$S_x(\nu) d\nu = \mathbf{E}[|\mathbf{X}(\nu, \mathbf{d}\nu)|^{\mathbf{2}}]. \tag{1.35}$$

$S_x(\nu)$ is known as the Power Spectral Density (PSD).

1.6 Unification: PSD $\Leftrightarrow$ ACF

It is well-known that the statistical properties of a Gaussian random variable are completely determined by its first two moments: its mean and variance. It is also well-known that such a process can be completely described by its PSD. This leads us to hypothesize that the time domain is no more fundamental than the frequency domain, and we expect

that the information contained in the ACF should be related to that in the PSD.

Let us look once again at equation 1.30. Using the Fourier representation of $x(t)$ we have:

$$R_x(\tau) = \mathbf{E}[\mathbf{x(t)x^*(t-\tau)}] \tag{1.36}$$

$$= \int_{-\infty}^{\infty}\int_{-\infty}^{\infty} \mathbf{E}[\mathbf{X}(\nu, \mathbf{d}\nu)\mathbf{X}^*(\nu', \mathbf{d}\nu')\mathbf{e^{-2\pi i[\nu t - \nu'(t-\tau)]}}]\mathbf{dt} \tag{1.37}$$

$$= \int_{-\infty}^{\infty} \mathbf{E}[|\mathbf{X}(\nu, \mathbf{d}\nu)|^\mathbf{2}]\mathbf{e^{-2\pi i\nu\tau)}}] \tag{1.38}$$

$$= \int_{-\infty}^{\infty} S_x(\nu) e^{-2\pi i[\nu t - \nu'(t-\tau)]} d\nu, \tag{1.39}$$

where we have assumed that the phases of the Fourier transforms are uncorrelated to get the final equality. Thus, from equation 1.39 we have the famed Wiener-Khintchin Theorem which states that the ACF, R_x and the PSD, S_x are Fourier transform pairs. We also have that:

$$\sigma_x^2 + m^2 = R_x(0) = \int_{-\infty}^{\infty} S_x(\nu) d\nu, \tag{1.40}$$

which is used extensively in this thesis. This discussion will also be relevant in Chapter 2 when we relate the *observable* correlation functions of the CMB temperature/polarization fields to their power spectra, provided by *theory*.

1.6.1 Linear Filters

We close this section with a brief discussion on the response of linear filters. Again we follow Mc Donough and Whalen in spirit and notation.

Consider a signal $x(t)$ which is passed through a linear filter. The output from the filter is a convolution of the filter's response function $h(t)$ with the signal, *viz*:

$$y(t) = \int_{-\infty}^{\infty} h(t - t')x(t')dt'. \tag{1.41}$$

The convolution theorem states that the Fourier transforms of $y(t), h(t), x(t)$ are related via:

$$Y(\nu) = H(\nu)X(\nu). \tag{1.42}$$

If the filter's transfer function, $H(\nu)$ is known, then equation 1.42 lets us determine the signal out of the filter by a simple inverse-Fourier transform. This fact allows us to analyze numerous phenomena which are found throughout this thesis in topics as (seemingly) unrelated as POLAR's sensitivity to the polarization's angular power spectrum and noise-spectrum out of POLAR's lock-in detectors!

Chapter 2

The Standard Cosmological Model and the Polarization of the CMB

2.1 Anisotropy of the CMB and the generation of Polarization

The anisotropy of the CMB is intimately related to its polarization. If our universe *were* isotropic there would be no metric perturbations, and space-time would be completely characterized by a Friedman-Robertson-Walker metric. Metric perturbations generate the anisotropy of the CMB, which, as we will demonstrate, generates the polarization. In an unperturbed universe (indeed, even in a universe with only first order dipole anisotropy caused by the earth's peculiar velocity with respect to the last scattering surface) there would be no polarization of the microwave background. As shown in Chapter 1, polarized radiation is produced by scattering of unpolarized radiation which possesses a quadrupole moment. Monopole radiation produces no polarization upon scattering. Dipole radiation

is really just a special case of monopole radiation as measured by an observer in a moving reference frame. Since the velocity of the observer can be transformed to zero by an appropriate boost, another observer comoving witht the radiation field would observe a monopole field incident on the electron. Since the total polarized intensity by either observer is frame-independent, the only reconciliation of this (apparent) paradox is that dipole radiation can produce no scattered polarization. This is not true of a quadrupole radiation field – it cannot be transformed away by any Lorentz transformation, and this fact coupled with the orthogonality of the spherical harmonics, can be used to show that it is *only* the quadrupole content of the incident field which can produce polarization via Thomson scattering.

There are three classes of perturbation that generate anisotropy of the CMB: scalar contributions, generated by matter and radiation density inhomogeneities, vector perturbations generated by vortical flows in the photon-baryon fluid, and tensor contributions, associated with gravitational waves. All three perturbations give rise to temperature anisotropy in the CMB via the Sachs-Wolfe effect [23].

We have motivated the fact that Thomson scattering of anisotropic radiation by free electrons generates polarization [24]. From equation 1.27 we see that scattering by a single electron produces polarized radiation with an intensity approximately 10% of the anisotropy quadrupole amplitude when averaged over all directions of photon incidence and scattering. In the case of CMB polarization the exact polarization level, as well as the angular scale of the distribution of polarization on the sky depend on the optical depth along the observer's line of sight, and on the particular sources of metric perturbation ([25]; [26]; [27]; [28]). For a recent review see: [29] and [30].

We see that there are two primary ingredients in order for polarization of the CMB

to arise: free-electrons and an incident, anisotropic, radiation field possessing a non-vanishing quadrupole moment. The CMB polarization observed today roughly scales as $\sim \int_0^{t_o} n_e(t) a_{2,0}(t) \frac{d\sigma_T}{d\Omega} dt$ where $n_e(t)$ is free-electron density at time t, $a_{2,0}$ is the quadrupole component of the CMB temperature radiation at t, and the integral is to be taken along the line of sight from decoupling to today. Due to the appearance of $\sin^2$ terms in equation 1.24, and the orthogonality of the spherical harmonics, *only* the quadrupole moment on the incident photon field contributes to the Thomson scattering. However, the quadrupole condition is easily satisfied for almost any class of perturbation.

Recall that prior to recombination, matter (in the form of protons and free-electrons) and photons were tightly coupled, *i.e.* the spatial distribution and temperature of one mirrored that of the other. The "linear regime" is the epoch when the density perturbations (due to matter anisotropy) were small with respect to the global distribution of matter. In this case we can expand the perturbations induced in the metric of space-time into a spectrum of plane-waves. An individual plane wave has a multipole expansion in cylindrical coordinates which is azimuthally symmetric with respect to its wave-vector. Choosing an explicit representation for an individual plane wave, we have:

$$e^{iz\cos\theta} = \sum_0^\infty (2\ell+1) i^\ell j_\ell(z) P_\ell(\cos\theta), \tag{2.1}$$

where θ is defined with respect to the z-axis of the cylindrical coordinate system, j_ℓ is a Bessel function and P_ℓ is a Legendre polynomial.

Again, we stress that the photon anisotropy prior to decoupling will have a matching spatial distribution. The density perturbation produced by this plane wave will affect the subsequent evolution of the distribution of matter and photons. At the peaks of the

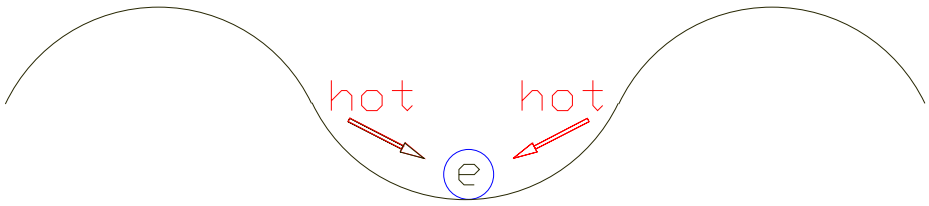

Figure 2.1: Matter falling into potential wells drags radiation with it. This radiation is blue shifted and thus appears hotter than radiation coming to the electron along the troughs of the plane-wave perturbation. The result produces a radiation field with an intensity given by the quadrupolar pattern $Y_{2,0}$.

density plane wave we are at a relative over-density in the matter distribution, and more matter will tend to accumulate here, dragging "warmer" photons with it. A peak in the density field is equivalent to a trough in the gravitational potential field. As a result, looking in directions parallel to the plane wave's wave-vector $\pm\hat{\mathbf{z}}$ we see warmer photons, while in directions along the troughs we see cooler photons (see figure 2.1).

This distribution of photons seen by the electron at rest varies as $\cos^2\theta$, or as the spherical harmonic $\propto Y_{2,0}$. Figure 2.2 shows this spherical harmonic along with the other two spherical harmonics with $\ell = 2$.

Now consider a "toy-universe" with only one density perturbation prior to decoupling[1] . An observer at the present who is looking at the surface of last scattering will see the results of Thomson scattering from electrons "seeing" their own local quadrupolar radiation fields. Due to the quadrupolar anisotropy as seen by each electron, the scattered radiation will

[1]Such a perturbation is also known as a "scalar" perturbation since, unlike "vector" or "tensor" perturbations, it has no handedness, *i.e.*, it is invariant under a parity transformation.

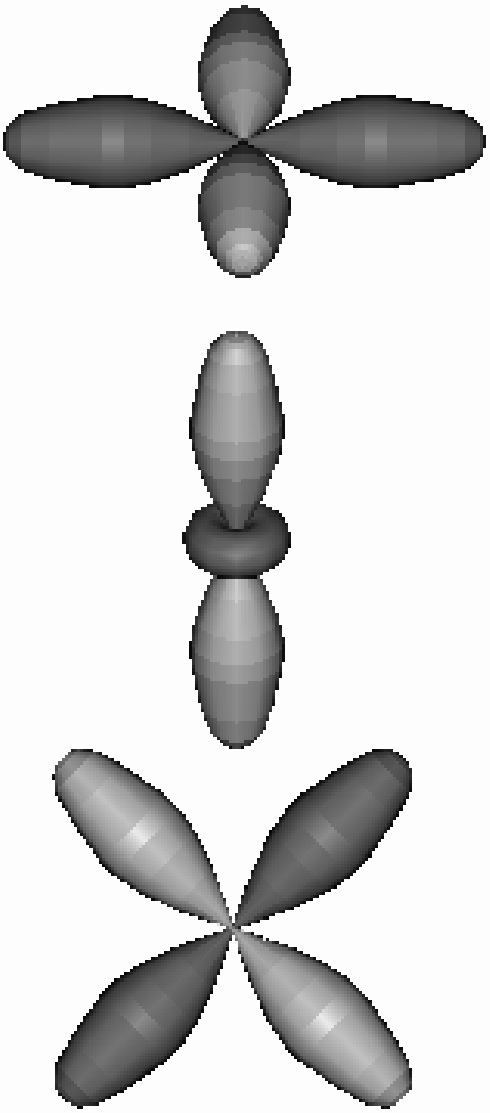

Figure 2.2: The three quadrupolar radiation fields as seen in the rest frame of an electron which can produce polarization via Thomson scattering. For each angular index ℓ there are $2\ell+1$ values of the magnetic index m. Shown here, from top to bottom, is the radiation field produced by tensor (gravitational wave) perturbations ($\ell = 2, m = \pm 2$); the radiation field produced by scalar (density) perturbations ($\ell = 2, m = 0$); and the radiation field produced by vector (vorticity) perturbations ($\ell = 2, m = \pm 1$). In this figure, the darker colors represent cooler, less intense photons, and lighter colors represent warmer, more intense photons. The polarization axis is always oriented along the direction of the more intense photons.

be polarized and will travel to the observer at present, encoding the magnitude of the quadrupole of the radiation field surrounding that electron prior to decoupling. Once generated, the magnitude of the observed polarization depends only on the orientation of the *hot-lobe* of the quadrupole with respect to the line of sight of the observer. The total polarization seen by this observer in this "toy-universe" will vary as $\propto Y_{2,0} \sin^2 \theta$, (see figure 2.3). To obtain the complete polarization pattern resulting from all density (scalar) perturbations which are observed at the present time, we must integrate the contribution of a distribution of plane waves with arbitrary wave-vectors. We note that the superposition of any number of scalar perturbations produces a polarization pattern on the celestial sphere which is curl-free. We refer the reader to [31] for an excellent discussion of the geometry of CMB polarization as produced on the sky by vector and tensor perturbations.

2.2 Ionized Epochs in the Evolution of the Universe

As mentioned earlier, the two key ingredients necessary to produce polarization of the CMB are an anisotropic radiation field, and a supply of free-electrons to Thomson scatter this radiation. To satisfy the free-electron condition we need to identify epochs in the evolution of the universe when a plasma existed. We will now describe two such epochs: recombination, and reionization. According to the standard model of the evolution of the pre-galactic medium after recombination, the previously ionized hydrogen combined[2] to form neutral hydrogen which was transparent to the CMB. However, the universe has undergone a secondary ionization of this recombined hydrogen. Gunn & Peterson [32]

[2]Showing that the term *re*-combination is a aggregious misnomer!

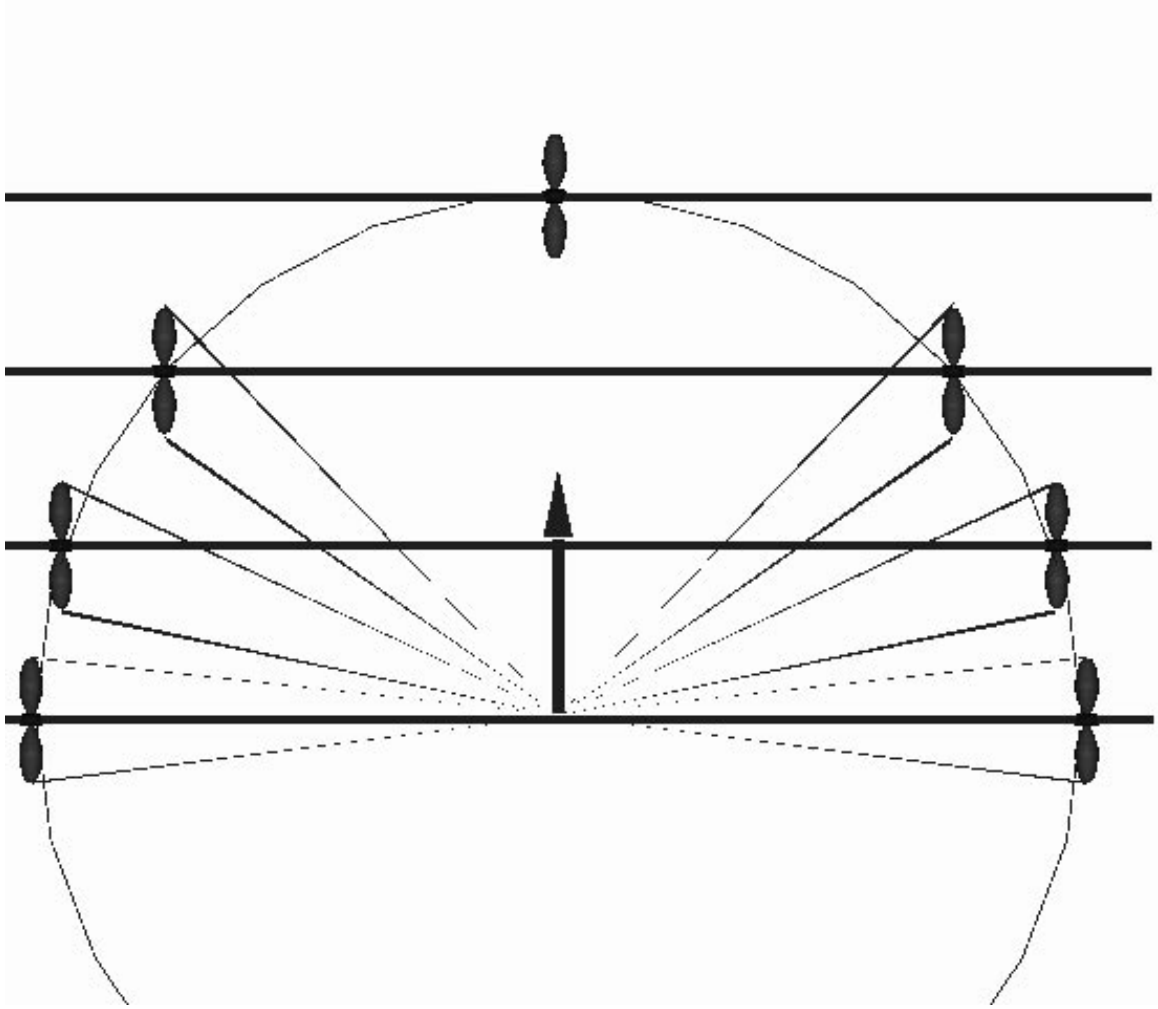

Figure 2.3: Seen here is a single plane-wave (scalar) perturbation, with wavevector $\vec{k}$ indicated by the arrow, at last scattering producing a local quadrupole for each electron located at the troughs of the potential perturbation (horizontal lines). The quadrupolar pattern $Y_{2,0}$ seen by *each* electron at the surface of last scattering produces *the same amount* of scattered radiation. The observer at the center of the diagram sees each individual scattered radiation field with an intensity which varies as $\sin^2\theta$, (θ = angle between $\vec{k}$ and the line-of sight) corresponding to the subtended angle of the hot lobe of the individual quadrupoles.

formulate a measure of the ionization fraction of the intergalactic medium using the lack of a Lyman-α trough in the observed spectra of distant quasars. Recent results show that the majority of intergalactic hydrogen is highly ionized to a redshift of at least $z \sim 5$, indicating that the universe must have reionized at an earlier epoch [33]. Several models predict reionization occurred in the redshift range approximately $30 < z_{\rm ri} < 70$ [34], [35], [36], [37], [38], [39].

In general, models of reionization often rely on structures such as an early generation of stars (Population III), or energetic proto-galaxies to provide either ionizing radiation or collisional heating mechanisms. Thus, for every model of reionization there corresponds a structure formation scenario, as well as a commensurate set of cosmological parameters to be confronted with observational evidence. We will not speculate here on the plausibility of specific models of reionization. As noted above, the Gunn-Peterson test provides definitive evidence for an ionized intergalactic medium out to a redshift of at least $z = 5$. In fact, the upper limit on the redshift of reionization is set only by the paucity of observed quasars beyond $z = 5$ and, in principle, could be much higher than this. The *COBE* FIRAS limit on the Compton-y parameter

$$y = \int d\tau k_b (T_e - T_{\rm cmb})/m_e c^2 \leq 2.5 \times 10^{-5}$$

[40], severely restricts the energy input allowed in models of reionization, but does not tightly constrain the epoch of reionization or the ionized fraction of the intergalactic medium. The limit is compatible with many early reionization scenarios.

As far as the small and intermediate-scale temperature anisotropy measurements are concerned, we refer the reader to [41], who perform a multi-parameter fit to the pub-

lished temperature anisotropy results in order to extract the earliest permissable redshift of reionization. They conclude that, for one of the currently fashionable "Cosmic Concordance" models, ($h = 0.65$, $\Omega_o = 0.3$, and $\Lambda > 0$), reionization is permitted as early as $z_{reionization} \sim 35$.

In contrast to the standard model of recombination, non-standard models invoke additional ionized epochs. These models predict a prolonged, or even non-existent, recombination and/or subsequent ionization of the recombined plasma. Since polarization is generated by scattering of photons on free electrons, its magnitude and spatial distribution could be used to discriminate between non-standard models and the standard model [42], [43], [26], [44], [45], [46], [47], [48]. An early reionization effectively introduces an additional 'last' scattering surface. This has two effects, both of which, in principle, can enhance the magnitude of the polarization on large angular scales. Primarily, the additional scattering of photons during reionization can create new, or amplify existing, polarized radiation via the Thomson mechanism discussed above. Additionally, the second 'last' scattering surface occurs at a much lower redshift, implying that the causal horizon on this rescattering surface is larger, and thus, will subtend a larger angle on the sky today.

As we will demonstrate, for reasonable non-standard models, the amplitude of polarization on 10° angular scales is on the level of 10% of the anisotropy, while for the standard model of recombination the corresponding polarization level does not exceed 1%. It is worth mentioning that all of these models predict approximately the same level of anisotropy at 10° scales, and hence all of them are compatible with the results of the *COBE* DMR experiment.

In the remainder of this section we will illustrate the important theoretical features of

the polarization of the CMB. We will first describe an analytic treatment which predicts the level of polarization for both standard and non-standard reionization histories. Next we will describe a numerical simulation of the effect of a non-standard reionization history on the polarization of the CMB. We will find that the more qualitative analytic results agree quite well with the quantitative results of our numerical simulations.

2.3 Polarization Produced by Cosmological Perturbations

We begin our discussion by developing a mathematical formalism which will allow us to describe the polarization of the CMB in a consistent fashion. With these tools, we will subsequently determine the polarization signal we expect to observe, using two different techniques. The first method is an analytic approach which will provide a physical framework for understanding the polarization of the CMB. The second approach is more quantitative, and will allow us to obtain numerical estimates of the polarization signal. In order to describe the polarization of the CMB, we will first introduce a parameterization which describes the polarization state of arbitrary radiation fields. We then apply this formalism to the polarization state of the cosmological signal which we are seeking to detect.

An alternate representation for the Stokes parameters will be of use in the following sections. We introduce a symbolic vector for the distribution function of occupation numbers of polarized radiation: $\hat{\mathbf{n}} = \frac{c^2}{h\nu^3}\hat{\mathbf{I}}$, where $\hat{\mathbf{I}}$ is the symbolic vector introduced in Chandrasekhar (1960) and is related to the Stokes parameters in the following way:

$$\hat{\mathbf{I}} = \begin{pmatrix} I_x \\ I_y \\ U \\ V \end{pmatrix}. \tag{2.2}$$

Since Thomson scattering cannot produce circular polarization, $V = 0$, we will only consider the 3-vector:

$$\hat{\mathbf{I}} = \begin{pmatrix} I_x \\ I_y \\ U \end{pmatrix}.$$

An unpolarized distribution in zero-th order approximation is given by:

$$\hat{\mathbf{n}}_{\mathbf{o}} = n_o \begin{pmatrix} 1 \\ 1 \\ 0 \end{pmatrix}.$$

As shown in [26], and further discussed in [49]; [46], polarized radiation in the presence of cosmological perturbations can be represented as:

$$\hat{\mathbf{n}} = n_o \left[\begin{pmatrix} 1 \\ 1 \\ 0 \end{pmatrix} + \hat{\mathbf{n}}_{\mathbf{1}} \right], \tag{2.3}$$

where $\hat{\mathbf{n}}_{\mathbf{1}} = \hat{\mathbf{n}}_{\mathbf{A}} + \hat{\mathbf{n}}_{\mathbf{\Pi}}$ is the correction to the uniform, isotropic, and unpolarized radiation described by $\hat{\mathbf{n}}_{\mathbf{o}}$. The Planck spectrum, $\hat{\mathbf{n}}_{\mathbf{o}}$, depends only on frequency, and $\hat{\mathbf{n}}_{\mathbf{A}} + \hat{\mathbf{n}}_{\mathbf{\Pi}}$ are the

anisotropic and polarized components, respectively, which are functions of the conformal time, η, comoving spatial coordinates, x^α, photon frequency, ν, and photon propagation direction specified by the unit vector $\hat{e}(\theta, \phi)$ with polar angle, θ, and azimuthal angle, ϕ, given in an arbitrarily oriented spherical coordinate system.

The equation of radiative transfer in terms of $\hat{\mathbf{n}}(\eta, x^\alpha, \nu, \mu, \phi)$, where $\mu = \cos\theta$, is:

$$\frac{\partial \hat{\mathbf{n}}}{\partial \eta} + \mathbf{e}^\alpha \cdot \frac{\partial \hat{\mathbf{n}}}{\partial x^\alpha} = -\frac{\partial \hat{\mathbf{n}}}{\partial \nu}\frac{\partial \nu}{\partial \eta} - q(\hat{\mathbf{n}} - \hat{\mathbf{J}}) \tag{2.4}$$

where

$$\hat{\mathbf{J}} = \frac{1}{4\pi}\int_{-1}^{+1}\int_{0}^{2\pi} \hat{\hat{\mathbf{P}}}(\mu, \phi, \mu', \phi')\hat{\mathbf{n}}(\eta, x^\alpha, \nu, \mu'', \phi'')d\mu' d\phi', \tag{2.5}$$

where $q = \sigma_T N_e a$, $\mathbf{e}^\alpha$ are the basis vectors, and the Einstein summation convention is implied. In these expressions, a is the cosmological scale factor, $\hat{\hat{\mathbf{P}}}$ is the scattering matrix described by Chandrasekhar [24], σ_T is the Thomson cross section, and N_e is the comoving number density of free electrons. In general, the effects of a particular choice of metric perturbation are manifest in the first term on the right hand side of (2.4). In the synchronous gauge we have that:

$$\frac{\partial \nu}{\partial \eta} = \frac{1}{2}\frac{\partial h_{\alpha\beta}}{\partial \eta} e^\alpha e^\beta \nu$$

[23]. After retaining terms up to first order in metric perturbations, $h_{\alpha\beta}$, and since $\frac{\partial \nu}{\partial \eta}$ is of the first order, we can replace $\frac{\partial \hat{\mathbf{n}}}{\partial \nu}$ by $\frac{\partial \hat{\mathbf{n}}_\mathbf{o}}{\partial \nu_o}$ in the source term (ν_o is the unperturbed frequency). This implies that the factor $\gamma = \frac{\nu_o}{n_o}\frac{dn_o}{d\nu_o} = \frac{d\ln n_o}{d\ln \nu_o}$ gives a universal frequency dependence for anisotropy and polarization effects, independent of the type of metric perturbations [26].

The angular dependence of $\hat{\hat{\mathbf{P}}}$ is such that

$$\frac{1}{4\pi}\int_{-1}^{+1}\int_{0}^{2\pi}\hat{\hat{\mathbf{P}}}(\mu,\phi,\mu',\phi')\hat{\mathbf{n}}_{\mathbf{o}}d\mu' d\phi' = \hat{0}, \tag{2.6}$$

(where $\hat{0}$ is the symbolic zero-vector), so we conclude in the zero-th order approximation, $\hat{\mathbf{J}} = \hat{0}$. For the first order approximation, in the following, we will understand by "$\hat{\mathbf{J}}$" actually $\hat{\mathbf{J}}_{\mathbf{1}}$, in which $\hat{\mathbf{n}}$ is replaced by $\hat{\mathbf{n}}_{\mathbf{1}}$.

After linearization and spatial Fourier transformation, the equation of transfer takes the following form (with ν_o replaced by ν):

$$\frac{\partial \hat{\mathbf{n}}_{1\vec{k}}}{\partial \eta} + ik\mu\hat{\mathbf{n}}_{1\vec{k}} = \gamma H_{\vec{k}} - q(\hat{\mathbf{n}}_{1\vec{k}} - \hat{\mathbf{J}}_{\vec{\mathbf{k}}}). \tag{2.7}$$

Here, $H_{\vec{k}} = -\frac{1}{2}\dot{h}_{\alpha\beta\vec{k}}e^{\alpha}e^{\beta}$, and "$\cdot$" $\equiv \frac{d}{d\eta}$. We have specified spherical coordinates in such a way that $\mu = \cos\theta$, where θ is the angle between a vector along the line of sight, $\hat{\mathbf{e}}$, and the wave vector $\vec{k}$ and ϕ is the azimuthal angle of the vector $\hat{\mathbf{e}}$, in the plane perpendicular to the vector $\vec{k}$.

For a given $\vec{k}$, $h_{\alpha\beta\vec{k}}$ can be represented as a superposition of scalar waves (below we will use subscript "S") and tensor gravitational waves (subscript "T"). Taking into account the tensorial structure of the waves, and restricting our consideration to perturbations with wavelengths longer than the cosmological horizon at the moment of equipartion (i.e. at the moment when the energy density of matter equals that of radiation, see for example [50]), we can write

$$H_{\vec{k}} = \frac{1}{15}\eta k^2\mu^2\kappa_S(k) - \frac{3}{2k^3}(1-\mu^2)\cos 2\phi\frac{d}{d\eta}\left[\frac{1}{\eta}\frac{d}{d\eta}\left(\frac{\sin k\eta}{\eta}\right)\right]\kappa_T(k) \tag{2.8}$$

Here, the $\sqrt{|\kappa_{S,T}(k)|^2}$ are the amplitudes of the corresponding metric perturbations at the moment when their wavelengths are equal to the cosmological horizon.

For $k\eta \ll 1$ we have:

$$H_{\vec{k}} \simeq \frac{1}{15}\eta k^2 \mu^2 \kappa_S(k) - \frac{3}{2}(1-\mu^2)\cos 2\phi \kappa_T(k) \tag{2.9}$$

while for $k\eta \gg 1$,

$$H_{\vec{k}} = \frac{1}{15}\eta k^2 \mu^2 \kappa_S(k) + \frac{3}{k\eta^2}(1-\mu^2)\cos 2\phi \cos k\eta \kappa_T(k) \tag{2.10}$$

For a plane wave perturbation with wavevector $\vec{k}$, the anisotropy and polarization can be described [26] as:

$$\hat{\mathbf{n}}_{\mathbf{A}} = \alpha_S(\mu^2 - \frac{1}{3})\begin{pmatrix} 1 \\ 1 \\ 0 \end{pmatrix} + \frac{\alpha_T}{2}(1-\mu^2)\begin{pmatrix} 1 \\ 1 \\ 0 \end{pmatrix}\cos 2\phi \tag{2.11}$$

$$\hat{\mathbf{n}}_{\mathbf{\Pi}} = \beta_S(1-\mu^2)\begin{pmatrix} 1 \\ -1 \\ 0 \end{pmatrix} + \beta_T \begin{pmatrix} (1+\mu^2)\cos 2\phi \\ -(1+\mu^2)\cos 2\phi \\ 4\mu \sin 2\phi \end{pmatrix} \tag{2.12}$$

Substituting (2.11) and (2.12) into the integro-differential Equation of Radiative Transfer, (2.4), we obtain the following system of coupled ordinary differential equations for $\alpha_{S,T}$ and $\beta_{S,T}$:

$$\dot{\beta}_{S,T} + \frac{3}{10}q\beta_{S,T} = -\frac{1}{10}q\xi_{S,T} \tag{2.13}$$

$$\dot{\xi}_{S,T} + q\xi_{S,T} = F_{S,T}, \tag{2.14}$$

where $\xi_{S,T} = \alpha_{S,T} + \beta_{S,T}$, and $F_{S,T}$ is the appropriate source function for scalar or tensor perturbations. This system of coupled equations illustrates the intimate relation between anisotropy and the generation of polarization. Integrating this system of equations we obtain the following general solution for $\beta_{S,T}$:

$$\beta_{S,T} = \frac{1}{7}\int_0^{\eta} F_{S,T}\left[e^{-\tau} - e^{-\frac{3}{10}\tau}\right] d\eta' \tag{2.15}$$

where $\tau(\eta, \eta') = \int_{\eta''}^{\eta} q(x^{\alpha})dx^{\alpha}$ is the optical depth with respect to Thomson scattering.

2.4 The First Ionized Epoch: Recombination

We are now in a position to investigate the effects of a prolonged recombination of the pre-galactic plasma. Recall that the contribution to the perturbation spectra for scalars and tensors is parameterized by $F_{S,T}$. By specifying the form of $F_{S,T}$ we are effectively enforcing a particular choice for our model. We will see that the polarization we observe today depends only weakly on the effect of the details of recombination, and is more sensitive to $F_{S,T}$.

For wavelengths large in comparison with the cosmological horizon at the moment of decoupling, η_D, ($k\eta_D \ll 1$), the source function, $F_{S,T}$ at this moment can be approximated by[49]:

$$F_{S,T} = \frac{\gamma}{15}\eta k^2 \begin{cases} \kappa_S(\vec{k}) \\ -\frac{2}{3}\kappa_T(\vec{k}) \end{cases} \tag{2.16}$$

It can be shown that the source functions are rather insensitive to the exact functional form of the variation of the optical depth with respect to time [26], [44]. These functions are primarily characterized by the epoch and duration of decoupling. Following [46], we adopt the following approximation for the time variation of the optical depth:

$$d\tau = -\frac{d\eta}{\Delta\eta_D}\tau$$

(see also [26] , [44] for a more detailed discussion). Here $\Delta\eta_D$ is the characteristic time scale of the duration of decoupling. Approximating the source functions under the integral (2.15), by their values at the moment of decoupling η_D, which gives the main contribution to polarization, we have

$$\beta_{S,T} \simeq \frac{1}{7}(F_{S,T})|_D \Delta\eta_D \int_0^\infty \left[e^{-\tau} - e^{-\frac{3}{10}\tau}\right] \frac{d\tau}{\tau} \tag{2.17}$$

$$= \frac{1}{7}\ln\frac{10}{3}(F_{S,T})|_D \Delta\eta_D$$

Hence,

$$\hat{\mathbf{n}} = -\frac{1}{105}\ln\frac{10}{3}\eta_D\Delta\eta_D k^2\gamma \left\{ \frac{1}{2}\kappa_S(k)(1-\mu^2) \begin{pmatrix} 1 \\ -1 \\ 0 \end{pmatrix} - \frac{3}{4}\kappa_T(k) \begin{pmatrix} (1+\mu^2)\cos 2\phi \\ -(1+\mu^2)\cos 2\phi \\ 4\mu \sin 2\phi \end{pmatrix} \right\}. \tag{2.18}$$

Comparing equation (2.18) with equation (2.12), we find that the polarization generated by a single perturbation mode with wavevector $\vec{k}$ is given by:

$$\Pi_{\vec{k}} = -\frac{2}{105}\ln\frac{10}{3}(\eta_D k)(\Delta_D k)\gamma\left\{\kappa_S(k)(1-\mu^2) - \frac{3}{4}\kappa_T(k)\left[(1+\mu^2)\cos 2\phi + 2\mu\sin 2\phi\right]\right\}. \tag{2.19}$$

Now we can calculate the root mean square (RMS) polarization measured by an antenna with an full-width-at-half-max (FWHM) Θ_A. The main contribution to the RMS polarization, $\Pi(\Theta_A)$, is contributed by modes with $k < k_{\max}(\Theta_A) \approx \frac{2\pi}{\Theta_A} = \frac{360^\circ}{\Theta_A{}^\circ}$:

$$\Pi(\Theta_A) = \sqrt{\langle\Pi^2\rangle_{k>\frac{2\pi}{\Theta_A}}} \tag{2.20}$$

$$= \frac{2}{105}\ln\frac{10}{3}\eta_D\Delta\eta_D\gamma\sqrt{Q_S B_S + Q_T B_T}, \tag{2.21}$$

where:

$$B_S = \int_{-1}^{1}(1-\mu^2)^2 d\mu = \frac{16}{15} \tag{2.22}$$

$$B_T = \frac{9}{8\pi}\left[\int_{-1}^{1}(1+\mu^2)^2\int_0^{2\pi}\cos^2 2\phi d\phi + \int_{-1}^{1}4\mu^2 d\mu\int_0^{2\pi}\sin^2 2\phi\right] = \frac{36}{5}. \tag{2.23}$$

Here $Q_{S,T} = \int_0^{k_{\max}(\Theta_A)} k^4|\kappa_{S,T}(k)|^2\frac{dk}{k}$, with $|\kappa_{S,T}(k)|^2 = \kappa_{0_{S,T}}k^{n_{S,T}}$, and $\sqrt{|\kappa_{0_{S,T}}|^2}$ are the amplitudes of perturbations with wavelengths equal to the cosmological horizon at the present moment ($n = 0$ corresponds to a scale invariant Harrison-Zeldovich spectrum). These amplitudes are normalized to the *COBE* DMR anisotropy quadrupole detection which is approximately equal to 2×10^{-5}. Assuming that $n_S = n_T = n$, we obtain

$$\Pi(\Theta_A) = \frac{8}{105\sqrt{15}} \ln \frac{10}{3} \eta_D \Delta\eta_D \frac{1}{\sqrt{4+n}} \left(\frac{360^\circ}{\Theta_A{}^\circ}\right)^{2+\frac{n}{2}} \gamma \sqrt{\kappa_{o_S}^2 + \frac{27}{4}\kappa_{o_T}^2}. \tag{2.24}$$

Taking into account the relationship between redshift and conformal time, $z \sim \frac{1}{\eta^2}$, we have that $\frac{\Delta z_D}{z_D} \sim \frac{2\Delta\eta_D}{\eta_D}$, hence

$$\eta_D \Delta\eta_D \simeq \eta_D^2 \frac{\Delta\eta_D}{\eta_D} = \frac{1}{2}\frac{\Delta z_D}{z_D^2} = \frac{1}{2}\frac{\Delta z_D}{z_D}\frac{1}{z_{SD}}\left(\frac{z_{SD}}{z_D}\right)$$

where z_{SD} is the redshift of decoupling predicted by the *standard* model of recombination, and z_D is the redshift of decoupling we are considering, *i.e.*, it is the "non-standard" decoupling redshift. Finally:

$$\Pi(\Theta_A) = 4 \times 10^{-7} \frac{\Delta z_D}{z_D} \left(\frac{z_{SD}}{z_D}\right) \left(\frac{7^\circ}{\Theta_A}\right)^{2+\frac{n}{2}} \gamma \aleph_{n,g} \tag{2.25}$$

where

$$\aleph_{n,g} = \frac{2 \times 10^{-2} \ln \frac{10}{3}}{105\sqrt{15}} \left(\frac{7^\circ}{360^\circ}\right)^2 \frac{\sqrt{\kappa_{o_T}^2 + \kappa_{o_S}^2}}{2 \times 10^{-5}} \frac{10^3}{z_{SD}} \left(1 + \frac{n}{4}\right)^{-1/2} \left(\frac{360^\circ}{7^\circ}\right)^{\frac{n}{2}} \sqrt{\frac{1 + \frac{27}{8}g^2}{1+g^2}} \tag{2.26}$$

and

$$g = \frac{\kappa_{o_T}}{\kappa_{o_S}}$$

is the ratio of the tensor perturbation amplitudes to the scalar amplitudes.

The factor $\aleph_{n,g}$ incorporates the perturbation amplitudes, normalized to the anisotropy quadrupole measured by the *COBE* DMR. It contains all information about the type of metric perturbation, allowing us to isolate factors which depend upon the nature of the

perturbations, and those which do not. For $n = 0$, and $g = 0$ (i.e., no tensor perturbations), $\aleph_{o,g} \simeq 1$. When $g = \infty$ (i.e., no scalar perturbations), $\aleph_{o,g} \simeq 1.84$. Finally, when $g = 1$ (i.e., equal tensor and scalar contributions), we find $\aleph_{o,g} \simeq 1.47$. From this we observe that $\aleph_{n,g}$ is rather insensitive to the ratio of tensor to scalar amplitudes, g.

We now emphasize the angular regions to which the preceding discussion is relevant. Equations (2.24) - (2.26) (which are based on asymptotic formula (2.9), and the approximations used in (2.17)), are valid for modes which satisfy: $k\Delta\eta_D < 1$. In terms of angle on the sky,

$$\frac{360^\circ}{\Theta_A{}^\circ}\frac{\Delta\eta_D}{\eta_D}\eta_D < 1.$$

We can apply equations (2.24) - (2.26) to an observation which has an angular resolution Θ_A, as long as:

$$\Theta_A > \Theta_{A_{\min}} = 360^\circ \frac{1}{2}\frac{\Delta z_D}{z_D^{3/2}} = \frac{180}{z_{SD}^{1/2}}\left(\frac{\Delta z_D}{z_D}\right)\left(\frac{z_{SD}}{z_D}\right)^{1/2} \simeq 6^\circ \frac{\Delta z_D}{z_D}\left(\frac{z_{SD}}{z_D}\right)^{1/2}\left(\frac{\Delta z_{SD}}{10^3}\right)^{-1/2}.$$

Specific Models of Recombination

As an example, the standard model of recombination predicts $\frac{\Delta z_D}{z_D} \simeq 0.1$, which implies that $\Theta_{A_{min}} \simeq 0.6^\circ$. For pure scalar perturbations ($n = 0$), the expected level of polarization at this angular scale is: $\Pi(0.6^\circ) \simeq 6 \times 10^{-6}$. For an observation with $\Theta_A \simeq 6^\circ$, the polarization is $\Pi(6^\circ) \simeq 5 \times 10^{-8}$. The observed polarization is suppressed by a factor of ~ 100 with this lower resolution beam.

Consider another example, a non-standard model for which $\frac{\Delta z_D}{z_D} \simeq 1$, and $z_D \simeq z_{SD}$, the angular scale is: $\Theta_{A_{min}} \simeq 6^\circ$. The polarization predicted in this scenario is: $\Pi(6^\circ) \simeq 5 \times 10^{-7}$. Finally, for $\Theta_A < \Theta_{A_{min}}$, the polarization is suppressed, and its dependence on

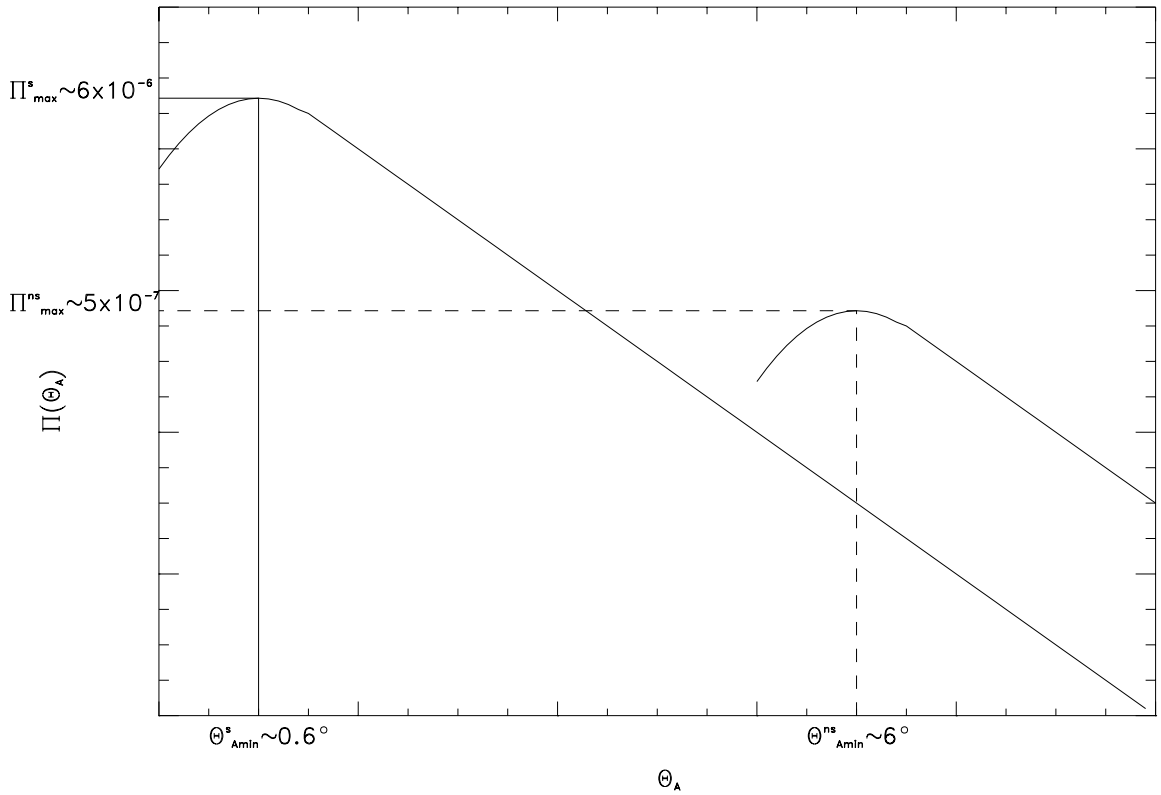

Figure 2.4: A schematic diagram showing the effects of standard, instantaneous recombination, vs. non-standard, prolonged recombination on the angular scale and magnitude of CMB polarization.

Θ_A is determined by the details of the ionization history [51] , [49] , [44] , [42] , [43].

To summarize, for a given Θ_A, the polarization level is proportional to $\frac{\Delta z_D}{z_D}$, see equation (2.25)) and is smallest for the standard model of instantaneous recombination. Alternatively, this analytic approximation applies to smaller angles in the standard model, as opposed to the larger angles predicted by non-standard models, with prolonged recombination, (see [44] for polarization in standard and non-standard models.

2.5 The Second Ionized Epoch: Reionization

For POLAR to detect a non-zero polarization signal at the large angular scales which it probes would require that the ionization history of the universe differ significantly from the

so-called "standard model". As mentioned earlier, non-standard models of the ionization history are characterized by protracted decoupling and/or non-zero optical depth along CMB photon trajectories. We have discussed the effect a of non-standard recombination using the analytic method treated above. We now wish to examine the effect of reionization on the details of the polarization of the CMB. This investigation lends itself particularly well to the numerical evaluation of the polarization power spectrum, calculated using numerical routines such as CMBFAST [52].

The effect of reionization can be parameterized in two equivalent forms. One method is specified by the optical depth, $\tau_{\rm ri}$, for photons due to Thomson scattering along a line of sight to the last scattering surface. The second method specifies the redshift of reionization, $z_{\rm ri}$, and the fractional ionization x (electron-to-proton ratio). The two parameterizations are related as follows [33]:

$$\tau_{\rm ri} = 0.0015 \left(\frac{x}{1}\right) \frac{\Omega_B}{0.05} \left(\frac{\Omega}{1}\right)^{-1/2} \left(\frac{h}{0.65}\right) (1 + z_{\rm ri})^{3/2}, \tag{2.27}$$

where h is the Hubble parameter, Ω is the total density parameter of the universe, and Ω_B is the density parameter of baryonic matter. Equation (2.27) shows the effect of curvature of the universe on the optical depth. For reionization occurring at the same redshift and ionization fraction, in an open universe ($\Omega < 1$), the optical depth will be greater than in a flat or closed universe. We also note that the physical size of regions which are in causal contact (Hubble radius) at the epoch of reionization, $t_{\rm ri}$, is of order $\sim ct_{\rm ri}$. We expect that regions smaller than this size will produce coherent polarization of the CMB, and affect the observed polarization power spectrum at angular scales which correspond to the angular scale subtended by the horizon size at the epoch of reionization. This argument is

similar to those which predict a coherence scale in the CMB anisotropy power spectrum. For example, the acoustic peaks in the CMB anisotropy power spectrum arise from causal mechanisms (i.e., sound waves propagating in the photon-baryon fluid) acting on scales of order the horizon size at the epoch of decoupling. A similar effect occurs for the CMB polarization power spectrum, though in this case it is the horizon size of the re-scattering surface, not the 'primary' scattering surface, which is imprinted in the observed power spectrum.

Following Peebles [33], we expect that the observed CMB polarization angular correlation scale will be: $\Theta_{\rm ri} \sim 0.1(\Omega_B \Omega h)^{1/3}$ rad. For $\Omega = 0.1, \Omega_B = 0.1, h = 1$ we find $\Theta_{\rm ri} \sim 1^\circ$, and for $\Omega = 1, \Omega_B = 0.05, h = 0.65$ we find $\Theta_{\rm ri} \sim 2^\circ$. This new angular scale, absent in non-reionized models, is manifested in the spatial polarization correlation function and creates a peak in the reionized polarization power spectra at angular scales $\theta \geq 0.5^\circ$.

Referring to subsection 2.6, a more quantitative prediction of the angular distribution of polarization on the sky is obtained from the angular power spectrum. Using a publicly available software routine (CMBFAST–elaborated on below) to calculate the power spectra, we have generated polarization spectra created by scalar perturbations in a Cold Dark Matter (CDM) dominated, completely reionized, universe with $x = 1, \Omega = 1, \Omega_B = 0.05, h = 0.65$. By varying the redshift of reionization in the range $0 < z_{\rm ri} < 100$, we compute multiple polarization power spectra, which are displayed in figure 2.5. The power spectra illustrate the main features expected from the theoretical principles detailed above. Large angular scales correspond to modes with wavelengths greater than the width of the last scattering surface. Prior to recombination photons and baryons were tightly coupled and the relatively short timescale for acoustic oscillations prevented the formation of long-wavelength perturbations. These effects are particularly

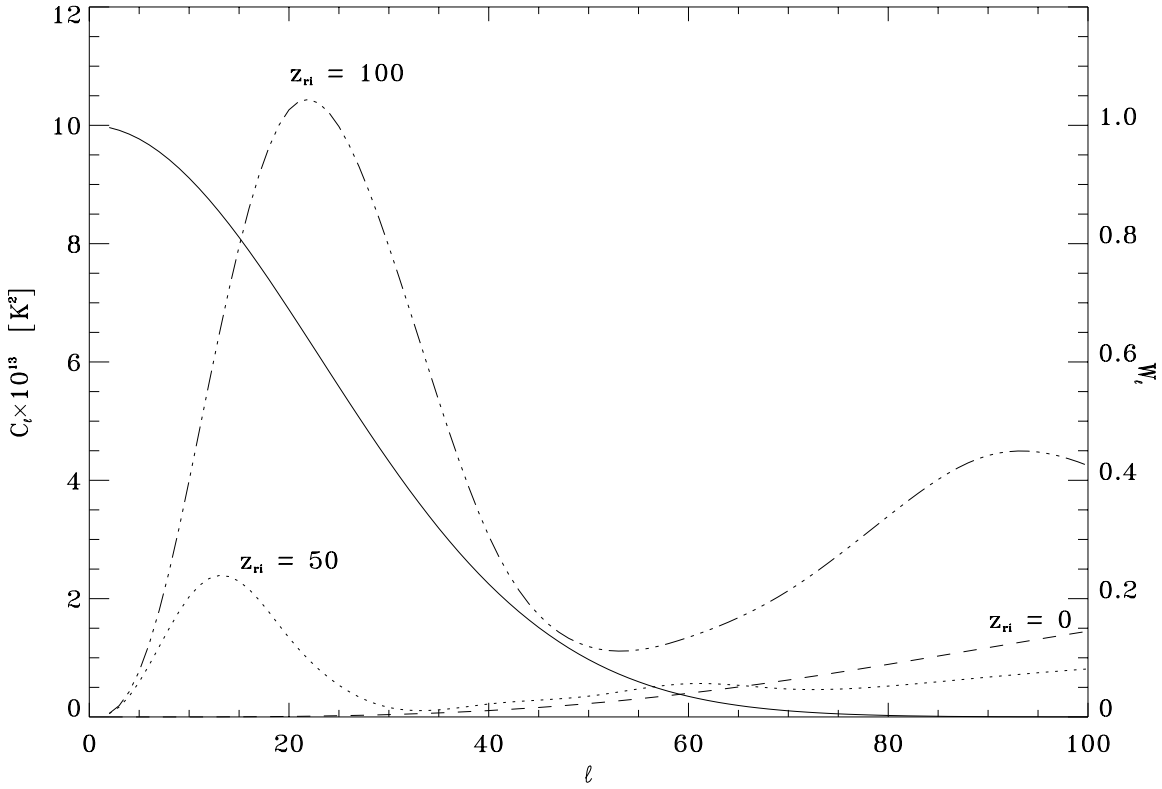

Figure 2.5: Polarization Power Spectra with and Without Early Reionization. The solid curve is the POLAR window function, W_ℓ, and the theoretical model predictions are indexed by the redshift at which reionization occured.

evident in models without reionization.

In models with early reionization, polarization at large angular scales is enhanced due to multiple photon scattering following reionization. At smaller angular scales ($\ell \sim 100$), in models with and without reionization, the polarization power spectra exhibit oscillatory behavior, caused by the same type of acoustic oscillations which generate the Doppler peaks in the anisotropy power spectra [48] , [51]. Though not relevant for the large angular scale considerations discussed here, for $\ell \gg 100$ the polarization is highly suppressed due to Silk Damping [29].

The power spectra are, effectively, predictions of the polarization which should be observable given a particular observing strategy. We will show in Chapter 8 that the

RMS polarization expected from the spectra shown in Figure 2 , with $\Theta_A = 7^\circ$, is in the range $0.05\mu\text{K} < I_{\text{pol}} < 1.0\mu\text{K}$, where the lower limit is standard recombination with no reionization, and the upper limit is for total reionization starting at $z = 105$. These limits agree well with the analytic estimates for non-standard ionization histories discussed at the beginning of this chapter. For a 6° experiment and a non-standard ionization history, figure 2.5 predicts a polarization level of $5 \times 10^{-7} \sim 1\mu\text{K}$ which agrees well with our numerical simulations of early reionization (e.g., for $z_{\text{reionization}} = 105$).

2.6 Polarization Power Spectrum

The analytic treatment above describes the essential physics responsible for the generation of CMB polarization. We have discussed the aspects of non-standard recombination which are relevant to the large scale polarization of the CMB. In order to estimate the observable polarization signature, we now detail a more quantitative approach based on the polarization power spectrum. This approach also allows us to analyze the effect of an early reionization on the observed polarization.

For quantitative estimates, the polarization and anisotropy source terms which appear in the equation of transfer can be decomposed into Legendre series. The individual modes are then evolved to the present where the spatial structure of the CMB can be computed [42], [43], [52]. Because the fluctuations in the CMB are imprint during the epoch of linear evolution of perturbations, the individual modes evolve independently. This treatment lends itself particularly well to numerical analysis [52].

We start by considering the temperature of the CMB which, being a scalar valued function, can be expanded in a spherical harmonic series on the sky, at a particular point

on the sky, $\hat{\mathbf{x}}$:

$$T(\hat{\mathbf{x}}) = \sum_{\ell,m} a_{T,\ell m} Y_{\ell m}(\hat{\mathbf{x}}) \tag{2.28}$$

where the $Y_{\ell m}(\hat{\mathbf{x}})$ are the spherical harmonics at $\hat{\mathbf{x}}$, and

$$a^{\mathrm{T}}_{(lm)} = \frac{1}{T_0} \int d\hat{\mathbf{n}}\, T(\hat{\mathbf{n}}) Y^*_{(lm)}(\hat{\mathbf{n}}) \tag{2.29}$$

are the temperature multipole coefficients and T_0 is the mean CMB temperature.

The temperature two-point correlation function is given by:

$$C_{T,\ell} = \frac{1}{2\ell+1} \sum_m \langle a^*_{T,\ell m} a_{T,\ell m} \rangle \tag{2.30}$$

The variance of the $a_{T,\ell m}$ is given by the $C_{T,\ell}$, since $\mathrm{Var}[a_{T,\ell m}] = \langle |a_{T,\ell m}|^2 \rangle - \langle |a_{T,\ell m}| \rangle^2 = \langle |a_{T,\ell m}|^2 \rangle \equiv C_{T,\ell}$ if the $a_{T,\ell m}$ are Gaussian distributed with zero mean, and $\langle \ldots \rangle$ denotes a whole-sky average followed by an average over all observational positions.

The polarization of the CMB is a tensor-valued function, with a symmetry group different from that of the anisotropy. The main complication arises since the polarization observables are coordinate dependent whereas any theoretical model worth its salt will produce frame-independent predictions. Thus we are led to consider frame-independent estimators of the power spectra. A hint at how to proceed is provided by the single heretofore neglected Stokes parameter: V. Recall that V is associated with circular polarization and hence is invariant under rotations about the line of sight. So if we can construct a "Stokes Parameter" which looks like V, but parameterizes *linear* polarization it too may be rotationally independent. The new parameter is actually two complex, linear combinations of Q and U:

$$(Q \pm iU)''(\hat{\mathbf{x}}) = \exp^{\mp 2i\psi}(Q \pm iU)(\hat{\mathbf{x}}). \tag{2.31}$$

Note that since the exponential is essentially a phase factor it will vanish when we construct the power spectrum of $(Q \pm iU)$ since then we will calculate $\langle (Q \pm iU)'(Q \pm iU)^{*'} \rangle$, which kills off the frame-dependent factor.

Polarization is usually described as either a vector field on the 2-sphere, or by the (frame dependent) Stokes parameters written as if the celestial sphere were actually a plane. Neither of which is correct, and both take away essential geometric information contained in the polarization field. The polarization is actually a spinor field on the 2-sphere – a most unfamiliar concept. To characterize it completely requires an expansion of the polarization field into a suitable basis for spinors on the 2-sphere. Zaldarriaga and Seljak [53] have made initial work in this direction based on the formalism originally developed by Roger Penrose and others [54] for gravitational wave applications.

An equivalent, though more geometric approach, was developed by Kamionkowski, Kosowsky, and Stebbins [55]; hereafter referred to as KKS. The KKS technique involves expanding the polarization field on the sky as a tensor field : $\mathcal{P}_{ab}(\hat{\mathbf{n}})$. The polarization tensor is a 2×2 symmetric ($\mathcal{P}_{ab} = \mathcal{P}_{ba}$) and trace-free ($g^{ab}\mathcal{P}_{ab} = 0$) tensor, parameterized by two real quantities. Given the Stokes parameters Q and U measured in any coordinate system, we can construct $\mathcal{P}_{ab}$. For example, in spherical polar coordinates, (θ,ϕ), the metric is $g_{ab} = \mathrm{diag}(1, \sin^2\theta)$ and

$$\mathcal{P}_{ab}(\hat{\mathbf{n}}) = \frac{1}{2} \begin{pmatrix} Q(\hat{\mathbf{n}}) & -U(\hat{\mathbf{n}}) \sin\theta \\ -U(\hat{\mathbf{n}}) \sin\theta & -Q(\hat{\mathbf{n}}) \sin^2\theta \end{pmatrix}. \tag{2.32}$$

As pointed out by KKS, the factors of $\sin\theta$ must be included since the coordinate basis for (θ, ϕ) is an orthogonal, but not an orthonormal basis.

We now seek the equations corresponding to 2.28 for the expansion of the polarization tensor in terms of a complete set of orthonormal basis functions for symmetric trace-free (STF) 2×2 tensors on the 2-sphere,

$$\frac{\mathcal{P}_{ab}(\hat{\mathbf{n}})}{T_0} = \sum_{l=2}^{\infty} \sum_{m=-l}^{l} \left[a^{\rm G}_{(lm)} Y^{\rm G}_{(lm)ab}(\hat{\mathbf{n}}) + a^{\rm C}_{(lm)} Y^{\rm C}_{(lm)ab}(\hat{\mathbf{n}}) \right], \tag{2.33}$$

where now we have *two* sets of expansion coefficients:

$$a^{\rm G}_{(lm)} = \frac{1}{T_0} \int d\hat{\mathbf{n}} \mathcal{P}_{ab}(\hat{\mathbf{n}}) Y^{{\rm G}\,ab\,*}_{(lm)}(\hat{\mathbf{n}}), \qquad a^{\rm C}_{(lm)} = \frac{1}{T_0} \int d\hat{\mathbf{n}}\, \mathcal{P}_{ab}(\hat{\mathbf{n}}) Y^{{\rm C}\,ab\,*}_{(lm)}(\hat{\mathbf{n}}). \tag{2.34}$$

Note that, since the scalar Spherical Harmonics obey orthonormality conditions, the basis functions $Y^{\rm G}_{(lm)ab}(\hat{\mathbf{n}})$ and $Y^{\rm C}_{(lm)ab}(\hat{\mathbf{n}})$ will as well. These functions are given in terms of covariant derivatives of the scalar spherical harmonics by [55]:

$$Y^{\rm G}_{(lm)ab} = N_l \left(Y_{(lm):ab} - \frac{1}{2} g_{ab} Y_{(lm):c}{}^{c} \right), \tag{2.35}$$

and

$$Y^{\rm C}_{(lm)ab} = \frac{N_l}{2} \left(Y_{(lm):ac} \epsilon^{c}{}_{b} + Y_{(lm):bc} \epsilon^{c}{}_{a} \right), \tag{2.36}$$

where ϵ_{ab} is the completely antisymmetric tensor, the ":" denotes covariant differentiation on the 2-sphere, and

$$N_l \equiv \sqrt{\frac{2(l-2)!}{(l+2)!}} \tag{2.37}$$

is a normalization factor. The new orthonormality properties are:

$$\int d\hat{\mathbf{n}}\, Y^{\mathrm{G}\,*}_{(lm)ab}(\hat{\mathbf{n}})\, Y^{\mathrm{G}\;ab}_{(lm')}(\hat{\mathbf{n}}) = \int d\hat{\mathbf{n}}\, Y^{\mathrm{C}\,*}_{(lm)ab}(\hat{\mathbf{n}})\, Y^{\mathrm{C}\;ab}_{(lm')}(\hat{\mathbf{n}}) = \delta_{LDL'}\delta_{mm'}, \tag{2.38}$$

$$\int d\hat{\mathbf{n}}\, Y^{\mathrm{G}\,*}_{(lm)ab}(\hat{\mathbf{n}})\, Y^{\mathrm{C}\;ab}_{(l'm')}(\hat{\mathbf{n}}) = 0. \tag{2.39}$$

These functions are the rank-2 generalizations of the "Vector Spherical Harmonics" used to Fourier expand the electromagnetic field [56]. As pointed out by KKS, the existence of two sets of basis functions,"G" and "C", is due to the fact that an STF 2×2 tensor is specified by two independent parameters, which shows, not surprisingly, that the linear polarization of a region on the celestial sphere is completely specified by two parameters, Q and U. In two dimensions, any STF tensor can be uniquely decomposed into a symmetric part: $A_{:ab} - (1/2)g_{ab}A_{:c}{}^{c}$ and an antisymmetric part: $B_{:ac}\epsilon^{c}{}_{b} + B_{:bc}\epsilon^{c}{}_{a}$ where A and B are two scalar functions. This is reminiscent of the Helmoltz Theorem which contends that a vector field (in 2 dimensions) can be expanded into a part which is the gradient of a scalar field and a part which is the curl of a vector field; hence KKS use the notation G for "gradient" and C for "curl". The correspondence is even stronger: if we have an map of polarization on the celestial sphere we can easily distinguish polarization patterns with a large "C" component by locating divergence-free "swirls" and "eddies", from large "E" regions which are distinguished curl-free patterns.

Following KKS, we see that by integration by parts equations (2.34) transform into integrals over scalar spherical harmonics and derivatives of the polarization tensor:

$$a^{\mathrm{G}}_{(lm)} = \frac{N_l}{T_0}\int d\hat{\mathbf{n}}\, Y^{*}_{(lm)}(\hat{\mathbf{n}})\, \mathcal{P}_{ab}{}^{:ab}(\hat{\mathbf{n}}), \tag{2.40}$$

$$a^{\rm C}_{(lm)} = \frac{N_l}{T_0} \int d\hat{\mathbf{n}}\, Y^*_{(lm)}(\hat{\mathbf{n}})\, \mathcal{P}_{ab}{}^{:ac}(\hat{\mathbf{n}}) \epsilon_c{}^b. \tag{2.41}$$

The second equation follows from $\epsilon^{ab}{}_{:c} = 0$. Since T and $\mathcal{P}_{ab}$ are real, all of the multipoles must obey the reality condition

$$a^{\rm X\,*}_{(lm)} = (-1)^m a^{\rm X}_{(l,-m)}. \tag{2.42}$$

Scalar perturbations can produce only G-type polarization and not C-type polarization. On the other hand, tensor or vector metric perturbations will produce both types [52]. Scalar perturbations are associated with curl-free motion of the photon-baryon fluid prior to decoupling an hence have no handedness so they cannot produce any "curl", whereas vector and tensor perturbations *do* have a handedness. As pointed out by KKS and Seljak, Zaldarriaga[53], and Zaldarriaga [57], observation of primordial (*i.e.*, *not* produced at reionization or by foregrounds) C-type polarization (a nonzero $a^{\rm C}_{(lm)}$) in the CMB would indicate the presence of either vector or tensor (or both) perturbations at the time of last scattering. This would be strong evidence for the existence of gravitational waves (which produce tensor perturbations), and provide the first detection of these objects. Given a foreground-free, low-noise map of the polarization pattern on the sky we could easily identify regions with non-zero "C"-type polarizations, and thus, we could literally confirm the existence of gravitational waves *by eye!*

Chapter 3

An Introduction to Radiometry

A microwave radiometer is a class of radio receiver which can measure the antenna temperature of distant sources. Radio Astronomy at meter-wavelengths was pioneered by K. Jansky in the mid-1930's, but it was not until after World War II that microwave radiometry was applied to the peaceful studies of sources of microwave emission. Robert Dicke is credited with the development of the first modern microwave radiometer which could measure sub-Kelvin differences in antenna temperature with integration times of a few seconds [58]. The technique known as "Dicke Switching" is a fundamental operating principle in all modern day microwave radiometers, though its implementation takes on numerous guises.

3.1 Total Power Radiometer

The simplest radiometer is known as the "Total Power Radiometer". This device precedes Dicke's measurements, and its shortcomings motivated the development of the technique which bears his name. The Total Power Radiometer consists of an antenna, a radio

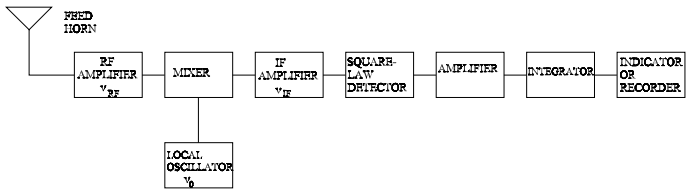

Figure 3.1: Schematic of a Superheterodyne Total Power Radiometer. The antenna couples radio frequency (RF) power into a high-frequency amplifier, whose output is subsequently down converted in frequency by a mixer and local oscillator. The intermediate frequency (IF) band is then amplified and detected. The final stage involves amplification, and filtration (integration) to reduce the noise on the recorded DC signal.

frequency (RF) amplifier, a power detector ("square-law" detector), and an integrating element. The square-law detector produces a voltage whose DC level is proportional to the power received by the radiometer. Riding on this DC voltage is a noise-waveform, which is smoothed by the integration element (usually a simple RC circuit). In figure 3.1 a slightly more complicated receiver is shown which uses a down-conversion scheme (mixer) to convert the RF band to a lower, more easily processed band known as the intermediate frequency (IF) band. This technique, known as heterodyning, is implemented in two of POLAR's channels: called "TP0" and "TP1", which detect the total power in the two orthogonal polarization states of the incident radiation (which can be partially polarized or unpolarized).

3.1.1 Minimum Detectable Signal

The minimum detectable signal of a radiometer is defined as the temperature of a source which produces a power level equal to the power level produced by the thermal noise of

the instrument itself in a given integration time [20].

Consider a radiometer with a system noise temperature T_{sys} looking at a load at absolute zero. We assume that antenna accepts only one spatial electromagnetic field mode and one polarization, the RF amplifier has a bandwidth of $\Delta\nu_{RF}$, and the integrator has a bandwidth of $\Delta\nu_{LF}$. The power produced by the system is $k_b T_{sys}\Delta\nu_{RF}$, where k_b is Boltzmann's constant. This produces a square-law voltage spectral density (VSD) of $S_\nu^{RF} \propto k_b T_{sys}$. From Chapter 1 we note that the RMS fluctuations in the *power* produced by the system are $\sigma^2 = \int_{\Delta\nu_{RF}} (S_\nu^{RF} d\nu)^2 = k_b^2(\Delta\nu_{RF})(T_{sys})^2$. This noise signal is integrated for a time τ corresponding to $\Delta\nu_{LF} \propto \frac{1}{\tau}$. From the convolution theorem applied to linear filters, as in Chapter 1, we find that the total system power RMS is:

$$\sigma^2 = 2(\Delta\nu_{RF}\Delta\nu_{IF})(k_b T_{sys})^2 \tag{3.1}$$

When looking at a source of antenna temperature ΔT, the square-law detector produces a DC signal voltage: $V \propto (k_b T \Delta\nu)$. To get the minimum detectable signal in an integration time τ, we find the ΔT that produces the same amount of DC power as the fluctuating AC power produced by the noise temperature of the radiometer. We find that:

$$\Delta T = \frac{T_{sys}}{\sqrt{\Delta\nu_{RF}\tau}}. \tag{3.2}$$

3.1.2 Limitations of the Total Power Radiometer Technique

The benefit of the Total Power Radiometer is its simplicity. Unfortunately, if the gain of the RF amplifier varies, say with temperature or voltage fluctuations in its power supply, the ultimate sensitivity to temperature variations of the source will be seriously degraded,

and equation 3.2 is no longer true. Temperature and voltage fluctuations will, in general, be worse on long timescales than on short timescales. This type of fluctuation is known as " $1/f$-noise". Equation 3.2 in the presence of $1/f$ noise becomes:

$$\Delta T = \frac{T_{sys}}{\sqrt{\Delta\nu_{RF}\tau}} \rightarrow \frac{T_{sys}}{\sqrt{\left(\frac{1}{\Delta\nu_{RF}\tau} + \frac{\kappa}{\nu^{-\alpha}}\right)}}, \tag{3.3}$$

where κ and α are both positive constants [59]. So we see that the effect of integrating for longer periods of time is offset by the presence of fluctuations of the output of the radiometer on long timescales. This was Dicke's motivation to switch the antenna between two different loads at a high frequency. In this approach the instrument does not have enough time to change appreciably in such short timescales. The faster the radiometer can be switched, the less important the $1/f$ fluctuations become. When one uses a single receiver, and switches the antenna between a celestial source and a reference target source of known temperature, ΔT is actually a factor of two *larger* than in the total power approach. However, the decrease in noise at low-frequencies (near the switching frequency) more than compensates for this decrease in sensitivity.

3.2 The Correlation Radiometer Technique

The correlation radiometer accomplishes the Dicke switching referred to above by viewing the *same* source with *two different receivers*, and subsequently correlating their outputs at RF frequencies using a multiplier. Physically, the multiplier is usually based on a non-linear device, such as a diode (see Chapter 4), which acts as a switch when provided with a bias waveform. The bias power for the diode comes from the uncorrelated RF power in each arm, which being in the RF band, effectively (Dicke) switches at these high radio

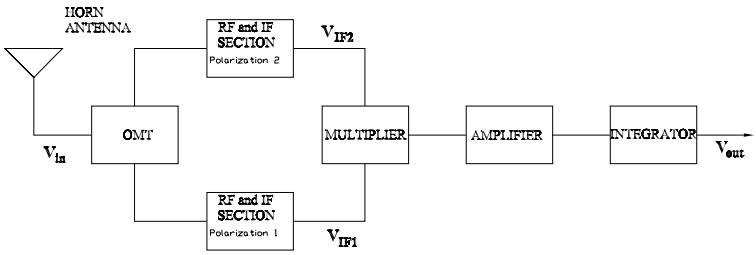

Figure 3.2: Schematic of a simple Correlation Polarimeter. Radio frequency (RF) fields are split into two linear polarization states by an orthomode transducer (OMT), and amplified. The field amplitudes are multiplied, producing a DC voltage proportional to their product. The DC product voltage is filtered and amplified before being integrated (low-pass filtered) prior to being recorded.

frequencies. The system has a $\sqrt{2}$ noise advantage over the single receiver Dicke switch [20]. The only penalty is the complication and cost of the second receiver. Consider the simplified correlation polarimeter shown in 3.2.

Radiation from the sky couples into a feed horn which propagates both of the field's linear polarizations. The orthomode transducer (OMT) separates the two polarizations, sending each one to its own receiver. The multiplier forms the product of the two fields, which are subsequently integrated. This multiplication and integration is the exact definition of the cross-correlation of the two polarization states, as defined in Chapter 1. As we will show in Chapter 4, for a single frequency, the fields which enter the multiplier are:

$$E_y(t) = E_{y_o} \cos[\nu t + \phi_y(t)] + n_y(t) \tag{3.4}$$

$$E_x(t) = E_{x_o} \cos[\nu t + \phi_x(t)] + n_x(t),$$

where n_i is the noise waveform generated by the amplifier viewing polarization state i.

Throughout we will assume $\langle n_i(t) n_j(t) \rangle = \sigma^2 \delta_{ij}$. Following Thompson [60], we will express an electric field as:

$$\hat{E}(\theta, \nu) = \int_{-\infty}^{\infty} E(\theta, t) e^{-i2\pi\nu t} dt \tag{3.5}$$

$$E(\theta, t) = \int_{-\infty}^{\infty} E(\theta, \nu) e^{i2\pi\nu t} d\nu, \tag{3.6}$$

where $E(\theta, t)$ is the electric field produced at time t when viewing at an angle θ with respect to the axis of the horn. The horn's amplitude response function, $G(\theta, \nu)$ (with dimension [length])[1], is assumed here to be axisymmetric. The antenna output *voltage* for polarization state $i \in \{x, y\}$ is:

$$\hat{V}_{iA}(\nu) = \int_{-\pi}^{\pi} \hat{E}_i(\theta, \nu_i) \hat{G}(\theta, \nu_i) d\theta. \tag{3.7}$$

The output voltage, after being amplified by the HEMT/mixer/IF amplifier chain (with total radiometer voltage transfer function $\hat{H}(\nu)$), is $\hat{V}(_i\nu) = \hat{H}(\nu)\hat{V}_{iA}(\nu)$.

The output of the correlator is given by:

$$R(\tau) = \lim_{T \to \infty} \frac{1}{2T} \int_{-\infty}^{\infty} V_x(t) V_y^*(t - \tau) dt. \tag{3.8}$$

---

[1] which is *not* equal to the power response function, $B(\theta, \nu)$, obtained, for example, when mapping the beam.

$$
\begin{aligned}
R(\tau) \quad &= \lim_{T\to\infty} \tfrac{1}{2T} \int_{-\infty}^{\infty} dt \int_{-\infty}^{\infty} d\nu_x \int_{-\infty}^{\infty} d\nu_y \int_{-\infty}^{\infty} d\theta \int_{-\infty}^{\infty} d\theta' \\
&\times \hat{E}_x(\theta,\nu_x)\hat{E}_y^*(\theta,\nu_y)\hat{H}_x(\theta,\nu_x)\hat{H}_y^*(\theta,\nu_y) \\
&\times \hat{G}_x(\theta',\nu_x)\hat{G}_y^*(\theta,\nu_y)e^{i2\pi\nu_x t}e^{-i2\pi\nu_y(t-\tau)}.
\end{aligned} \tag{3.9}
$$

Remembering that $\int_{-\infty}^{\infty} e^{i2\pi t(\nu_x-\nu_y)}dt = \delta(\nu_x - \nu_y)$, we have:

$$
R(\tau) = \int_{-\infty}^{\infty} \hat{\gamma}(\nu)\hat{B}(\nu)H_x(\nu)\hat{H}_y^*(\nu)e^{i2\pi\nu\tau}d\nu. \tag{3.10}
$$

where:

$$
\hat{\gamma}(\nu) = [\hat{E}_x(\nu_x)\hat{E}_y^*(\nu_y)] \tag{3.11}
$$

is the *source coherence function*, and

$$
\hat{B}(\nu) = \int_{-\pi}^{\pi} d\theta' \int_{-\pi}^{\pi} \hat{G}_x(\theta',\nu)\hat{G}_y^*(\theta,\nu)d\theta \tag{3.12}
$$

is the power response function of the horn, conventionally known as *the beam pattern.*

The properties of the source coherence function and the beam pattern completely determine the output voltage.

3.2.1 Minimum Detectable Signal

As in the case of the total power radiometer the sensitivity depends on both the system noise temperature and the RF bandwidth of the amplifiers. Since there are now two RF amplifiers we take the system temperature to be their geometric mean: $T_{sys} = \sqrt{T_{sys}^x T_{sys}^y}$.

For an unpolarized source which fills the antenna beam completely, each OMT polarization port sees only half of the total incident power.

Since the correlation polarimeter is essentially differencing the power (antenna temperature) of each polarization state, the correlator output can be symbolized by $V_{corr} \propto T_y - T_x$. If we assume the noise of the two receivers are uncorrelated (though approximately equal) then by simple error propagation we see that the RMS noise of the correlator output is $\sqrt{2}$ worse than the total power receiver. For the Dicke radiometer this result also holds.

The minimum detectable temperature difference in an integration time τ for the correlation radiometer is:

$$\Delta T = \sqrt{\frac{2T_{sys}^{x} T_{sys}^{y}}{\Delta\nu_{RF}\tau}}. \tag{3.13}$$

We also note here, for comparison, that the Dicke radiometer divides its integration time equally between viewing the signal and the noise which is why it is $\sqrt{2}$ times worse than the *correlation radiometer*, and a full factor of 2 worse than the *total power radiometer*[59].

Chapter 4

POLAR: Experimental Description

Before embarking on the technical details of the POLAR experiment, it is appropriate here to give a brief historical overview. The development of the correlation radiometer technique preceeded the discovery of the CMB in 1965; see for example [61]. In the early days of the COBE experiment the idea to apply the correlation radiometer to do CMB work was proposed. Although not implemented on COBE, development correlation radiometers and interferometers as viable CMB receiver techniques continued for many decades, boasting numerous experiments in the areas of anisotropy research ([62], [63], [64]) and the spectral measurements of [65]. The idea to develop a correlation radiometer for investigation of the polarization of the CMB can be traced to Prof. D. Wilkinson of Princeton University.

As a final interesting postscript, we note that a (pseudo) correlation radiometer will form the heart of the MAP [10] and PLANCK [11] Low Frequency Instrument's techniques

to recover the polarization and anisotropy of the CMB from space in the early part of the next century.

4.1 POLAR: Experimental Overview

POLAR is the first dedicated correlation polarimeter designed for measurements of the CMB. It has the widest bandwidth ($\sim$ 6 GHz) of any correlation receiver ever used for CMB work. This chapter summarizes the major components of the instrument as well as all known systematic effects. Measurement of polarization of the CMB poses a wide variety of experimental challenges, many of which are familiar from the experiments now measuring spatial anisotropy in the CMB. We describe below the design of POLAR to illustrate the experimental issues that must be addressed in any CMB polarization observation.

POLAR measures polarization on 7° scales in the $K_{\rm a}$ band, which is the spectral band covering the frequencies between 26 and 36 GHz. This band is multiplexed into three sub-bands to allow for discrimination against foreground sources and to solve technical problems in the development of a wide-bandwidth analog correlator. The radiometer executes a drift scan of the zenith with a FWHM = 7° beam produced by a corrugated feed horn antenna. In a preliminary engineering run, POLAR has observed $\sim$ 36 different pixels for 5 days, and in a single night of data achieves a sensitivity level of $\sim 100\mu$K per 7° FWHM pixel.

POLAR's design builds on techniques developed in previous searches for CMB polarization [13], [66], [15], [67], [17], [18] and is driven by several factors: the size and angular scale of the anticipated CMB signals, spectral removal of foreground sources, optimization of the observing scheme, and anticipated systematic effects.

Radiation from the sky couples into a corrugated circular horn antenna (See Fig. 4.1). This antenna has extremely low side lobes, near -80 dB at 90° off axis, in both polarizations, across a full waveguide band. The antenna output couples to an ortho-mode transducer (OMT), a waveguide device that decomposes the incoming wave into two orthogonal linear polarization components. The OMT defines the x-y coordinate system of the antenna. The entire experimental apparatus rotates about the symmetry axis of the feed-horn in order to measure both linear polarization Stokes parameters.

The Q and U Stokes parameters are defined in terms of a coordinate system fixed to the sky. There are several approaches to measuring Q and U for a particular pixel on the sky. Lubin & Smoot [15] employ a Dicke switch which alternately couples each of the polarization components from the OMT to a low-noise amplifier and square-law detector [66], [15]. Phase-sensitive detection at the modulation frequency of the switch yields the difference between these two components, the Q Stokes parameter, and helps overcome $1/f$ noise from the amplifier. After a 45° rotation about the antenna symmetry axis the instrument measures the U Stokes parameter.

A second technique which has been used for polarimetry couples the output of an OMT directly to two separate total-power radiometers [68], [69]. The beam is switched on the sky to measure the spatial anisotropy in two orthogonal polarizations. This approach measures the anisotropy in the Q Stokes parameter of the incident radiation field, and currently provides the most stringent upper limits on the polarization of the CMB.

An alternate approach, employed in POLAR, is the correlation radiometer [61], [59]. In this instrument the two polarization components are amplified in separate parallel amplifier chains and the output signals are correlated, resulting in a signal proportional to the U Stokes parameter. This type of instrument effectively "chops" between the two input

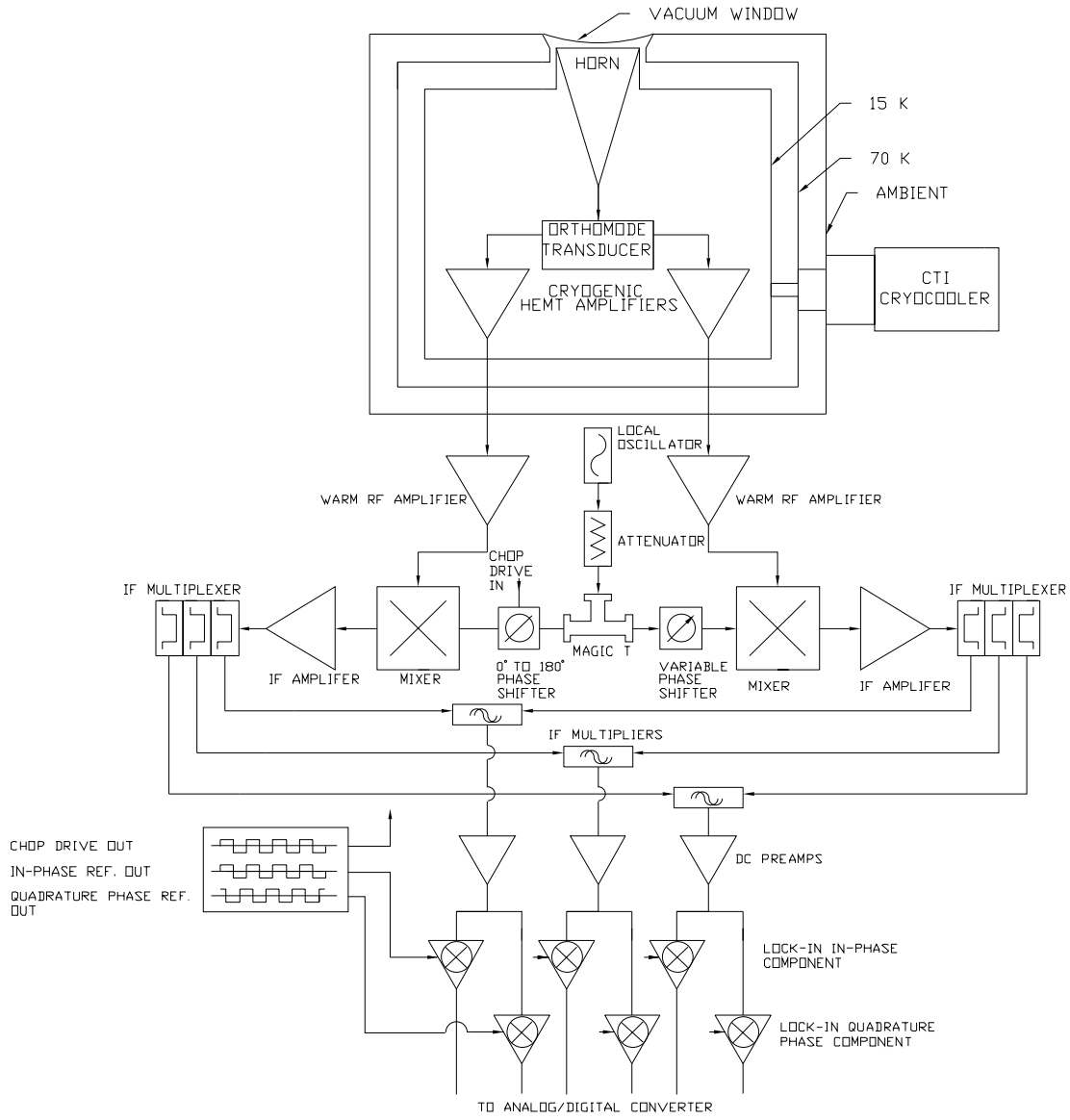

Figure 4.1: Schematic of the POLAR $K_{\rm a}$ band Radiometer. See text for description of components.

RF signals at a frequency which is comparable to that of the RF signals themselves. An advantage of this differencing mechanism is that it has no magnetic or moving parts which have traditionally complicated experiments of this type. After a 45° rotation the correlator gives an output proportional to the Stokes Q parameter. POLAR rotates continuously about the vertical at 3 RPM. The rotation modulates the output sinusoidally between U and Q at twice the rotation frequency and allows the removal of an instrumental offset and other instrumental effects that are not modulated at this frequency.

4.2 The POLAR Radiometer

The POLAR radiometer is comprised of 3 main sections:

- Cold receiver components: optics, OMT, isolators, HEMT amplifiers.
- Room-temperature receiver components: warm RF amplifiers, heterodyne stage, warm IF amplifiers, band-defining filters, detectors.
- Post-detection components: pre-amplifiers, low frequency processing, and data acquisition.

4.3 Cold Receiver Components

4.3.1 Dewar

The components comprising the "cold receiver section" are naturally defined by those contained in the dewar, which we will currently describe. The POLAR dewar is a custom fabricated dewar constructed by Precision Cryogenic Systems[1] (see figure 4.2). The de-

[1]PCS: Indianapolis, In

war is designed to house a CTI 350 cryocooler coldhead, and possesses no liquid cryogen containers. The dewar was designed to be quite flexible, accommodating numerous possible upgrades. One possible upgrade configuration would include the addition of 2 more corrugated feed horns in the nominal 20K (second stage) working volume. With this in mind, the current working cold-volume is divided into three sections, where the $K_{\rm a}$ section occupies one-third of the shielded second stage. The first stage is used to cool a radiation shield, which is nominally maintained at a temperature of $\sim$ 80K.

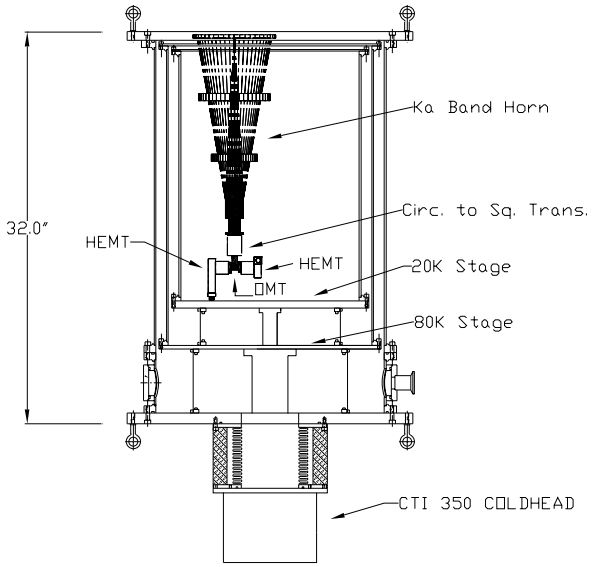

Figure 4.2: POLAR Dewar and $K_{\rm a}$ band cold receiver components. The horn is located off of the symmetry axis of the dewar in order to allow for future, higher-frequency receivers to perform simultaneous observations.

4.3.2 Vacuum System

For a large dewar such as POLAR's, a high vacuum is essential to achieve reasonable cool-down times. The vacuum system is an Edwards Turbo pump system composed of a mechanical roughing pump and a turbo-molecular pump. The turbo-molecular pump

has an exit aperture, D, of 100 mm which is maintained for the majority of the vacuum length, $L \sim 1750$mm. We convert from ISO-100 to KF-50 (50 mm) vacuum bellows hose just prior to attaching to the dewar block-valve. As the conductance of a vacuum line in the molecular-flow regime scales as D^3/L, the large diameter pump lines more than compensate for the relatively long length. After leak-proofing the dewar, and cooling down, it remains at $\sim 1 \times 10^{-5}$ Torr for months at a time.

4.3.3 CTI Cryocooler

Following pump-down to $\sim 1 \times 10^{-4}$ Torr, the pump is detached and the cryocooler's compressor (CTI 8500 Air Cooled) is activated. The cryocooler is capable of ~ 50 Watts of cooling power at 80K (first stage) and ~ 5 Watts at 20K (second stage). In the field it is found that the ultimate cold stage temperatures are correlated with the ambient temperature of the shelter in which POLAR resides. Because our compressor is air-cooled[2], as opposed to CTI's water-cooled version, the compressor's compression ratio is a strong function of ambient temperature, which modifies its cooling efficiency. Maintaining the temperature stability of the compressor is accomplished, to first order, by a commercial air-conditioner during the summer months which counters the $\sim 2kW$ heat output from the compressor. During the winter, the heat output by the compressor itself serves to keep the enclosed POLAR shelter at a nearly constant temperature. The compressor is mechanically isolated from the radiometer by use of a separate rotation bearing coupled loosely to the motor-driven main bearing by copper braid. The compressor is further isolated on its bearing by use of rubber padding on all support structures.

[2]which is necessary due to the fact that POLAR rotates continuously

The cold radiometer components are inside the 80K stage radiation shield. Of course it is essential to have vacuum-tight feedthroughs into and out of the dewar. Both waveguide outputs from the HEMTs leave the dewar through vacuum-port WR-28 waveguide feedthroughs from Aerowave[3]. The feedthroughs are mounted on a single brass-disk flange, which also serves as a feedthrough for the HEMT bias wiring and the Lakeshore[4] #10 Temperature Diode readout wiring. The final major port in the dewar is the main vacuum window through which passes our $K_{\rm a}$ band signal. This port is mounted ~ 3" radially off the rotation axis of the cryostat to allow for additional feed horns at higher frequency as mentioned above.

4.4 Optics

POLAR's optical system is simplicity itself. There are no unwieldy mirrors, chopping, flats, secondaries, tertiaries, etc. The main element is a single corrugated feed horn. Due to the absence of supplemental beam-forming reflectors, spurious effects introduced by cross-polarization by optical elements is near the minimum possible level for a millimeter wave instrument. Only optical polarimeters are capable of achieving lower levels of cross-polarization [70].

4.4.1 Corrugated Scalar Feed horn

The only true optical element in POLAR is its corrugated feed horn. The canonical theoretical treatment of these devices is discussed in [71]; this section merely describes

[3]Aerowave Corp., Medford, MA

[4]Lakeshore Cryotronics, Westerville, OH

the relevant device parameters which are necessary and sufficient to construct and model the performance of the horn.

POLAR's horn was designed by Dr. Josh Gundersen, and is based on the procedure outlined in [72], and is nearly identical to the $K_{\rm a}$-Band feed horn employed by the *COBE* DMR experiment [73]. The goal of the corrugated feed horn is to provide a low-sidelobe, low-cross-polarization Gaussian beam on the sky. The device should exhibit a high degree of symmetry in its E and H planes and, if possible, produce a diffraction-limited power response with a narrow full-width-at-half-maximum (FWHM). The final condition is sought since, as shown in Chapter 2, the angular power spectrum of polarized anisotropy on the sky is expected to peak at small angular scales.

Although the input to the orthomode transducer (OMT) is square-waveguide, in which we desire to simultaneously propagate only the $\mathrm{TE}^{\square}_{10}$ and $\mathrm{TE}^{\square}_{01}$ modes[5], the horn has a circular output and is most naturally treated using the theory of cylindrical waveguides. In cylindrical coordinates a cylindrical waveguide will propagate a transverse field mode with no azimuthal angle dependence[6] if certain conditions on the waveguide's impedance and admittance are satisfied. This mode will have a pure co-polar radiation field , *i.e.* on-axis, its cross-polarization will vanish. The conditions required are that the impedance, Z, and admittance, Y, at the waveguide wall are both identically zero. The impedance condition is ensured by virtue of the fact that the azimuthal component of the field is always locally transverse to the metallic boundary, *i.e.* $E_{trans} = E_{\phi}|_{r=r_1}$. Maxwell's equations near the surface of a metal stipulate that the tangential component of the field vanishes at the

[5]This is the so-called "hybrid-mode" condition

[6]This is a "balanced hybrid mode"

boundary of a conductor at $r = r_1$, so $Z \propto E_\phi = 0$. Thus, the use of a metal has paid off. But what about the effect of the corrugations? Surely if the walls of the guide are not smooth, it is impossible to simultaneously have the impedance vanish at all locations along the guide. However, as long as the corrugations are smaller than $\frac{\lambda}{4}$, the field does not sense the presence of the corrugations, and the surface is then just as conductive as a smooth metal surface.

However, the corrugations have their role: they null out any residual admittance at the wall of the guide, and effectively present a high resistance to currents which attempt to flow along the walls of the guide. The corrugations are $\frac{\lambda}{4}$ in height, so that a field is 180° out of phase with itself after climbing up and then down the corrugation. This phase cancelation is only strictly true for one frequency of course, but in practice the frequency dependence can be offset by tolerating a slight mode imbalance.

Thus we have an electric field of the following form:

$$E_x(r) = AJ_0(K_c r)\exp\left(\tfrac{-jkr}{2R_0}\right) \quad E_y(r) = 0$$

where r is the radial distance in our cylindrical coordinate system, A is the amplitude coefficient, and $K_c r_1 = 2.405$ is the root of the zero-order Bessel function $J_0(K_c r)$.

The complete modal-distribution of the E_x field is given by expanding the Bessel function in equation 4.1 in Gauss-Laguerre modes, *viz*:

$$J_0(K_c r) = \sum_{p=0}^{\infty} A_p L_p^0\left[\frac{2r^2}{w^2}\right]\exp\left(-r^2/w^2\right) \tag{4.1}$$

where $L_p^0(x)$ is a zero-order Laguerre polynomial and $w = w(z)$ is the locus of points where the electric field in the horn is $\frac{1}{e}$-times smaller than the on-axis field. Wylde [74] demonstrates that in order to maximize the power ($\propto E^2$) in the fundamental mode, the function $w(z)$ should have a minimum at a point located $w_o = 0.6435a$ inward from the horn's aperture; here a is the radius of the horn aperture. The minimum of $w(z)$ is known as "the beam waist", and is the Gaussian Optics generalization of the geometric optics "focus".

Table 4.1, reprinted from [75], in turn reprinted from [71] gives the calculated power in each mode for the first 11 modes of the expansion in equation 4.1. We have used this model to predict the far-field beam pattern of the POLAR K_a band horn out to $\sim 20^\circ$. The agreement is quite impressive for such a simple model, obviating the need for a pricey, commercial finite-element field-analysis code.

Table 4.1: Normalized Power Coefficients for Gauss-Laguerre Modes

Mode	Power coefficient
0	0.9792
1	4.90×10^{-9}
2	1.45×10^{-2}
3	1.86×10^{-3}
4	3.81×10^{-4}
5	1.16×10^{-3}
6	3.97×10^{-4}
7	1.50×10^{-8}
8	1.59×10^{-4}
9	2.33×10^{-4}
10	1.12×10^{-4}

If the horn had an infinitely wide aperture, its angular response[7] would be a delta-function. We would have a true "pencil-beam" – one with no off-axis response. Unfor-

[7] $(\mathcal{F}[E(r)])^2$, where $\mathcal{F}$ is the Fourier transform of the field in the aperture, $E(r)|_{z=L}$.

tunately, we could not accommodate such an idealization and our horn's aperture field pattern is necessarily truncated sharply at the physical radius of the horn, a. This sharp transition introduces diffractive "ringing" in the angular power response of the horn, a condition known as a "side-lobe". The simple Gauss-Laguerre model breaks down at low-power levels, which for us translates to the far off-axis sidelobes of the horn located at $\sim 40^\circ$ and beyond. In the absence of a reliable model for the far off-axis behavior of our feed, we have measured the beam response for a variety of frequencies, for both polarizations, as well as the cross-polarization response. The results of the simple Gauss-Laguerre model are summarized in figure 4.3.

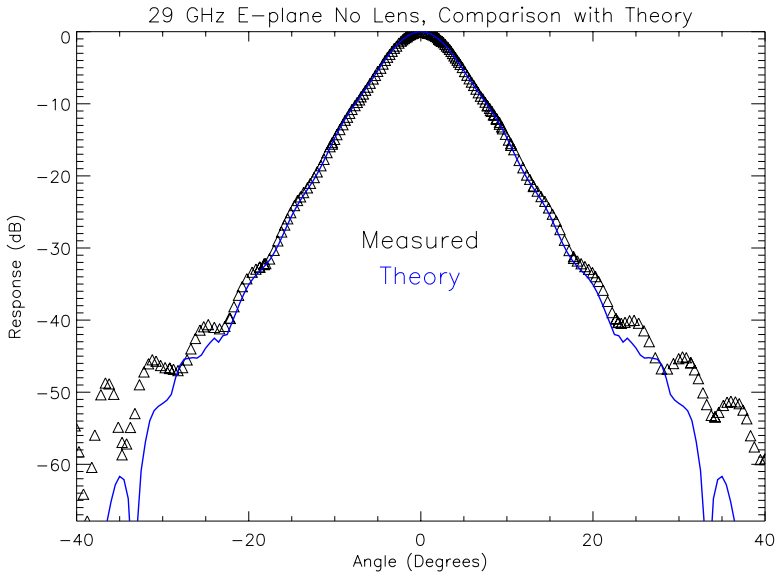

Figure 4.3: Shown here are the results of the Gauss-Laguerre model described in the text (solid line), compared with the E-plane beam map at 29 GHz (triangles).

The final, but by no-means least important part, of the feed horn is the *mode converter* which is a separate electroformed element placed at the throat of the horn. The mode converter combines the TE°_{11} and TM°_{11} circular waveguide modes to create the HE°_{11} corrugated waveguide mode. The mode converter's corrugations are of varying height, unlike those in the flare section of the horn. The primary purpose of the variable height

corrugations is to define the bandpass of the horn, without sacrificing the sidelobe or cross-polarization levels achieved in the flare section of horn [71], [72], [76], [77].

Up until this point we have been rather amplicentric, *i.e.* we have largely ignored phase considerations. The electrical path length from points in the aperture plane to the horn throat is a function of r, implying that the phase of a wavefront which is in-phase upon impinging on the aperture will be progressively out of phase as a function of radial distance off the horn axis. This phase error leads to a decoherance of the electromagnetic field. The phase error, Δ, is usually normalized to a particular wavelength, generally the nominal band's center wavelength, λ_o. From elementary geometric considerations we have:

$$\Delta \equiv \frac{l_{slant}}{\lambda_o}(1 - \cos\theta_o) = \frac{a}{\lambda_o}\tan(\frac{\theta_o}{2}) \tag{4.2}$$

where l_{slant} is the length from the horn's apex to its aperture radius, a, and θ_o is the horn flare's semi-angle. Small-Δ horns produce diffraction-limited pixels on the sky, which are necessarily frequency-dependent. Large-Δ horns produce nearly frequency-independent beams because the frequency information is smeared out across the band. For $0.2 > \Delta$ and $\Delta > 1.2$, the phase-center is frequency independent, though, in practice, difficult to realize mechanically. For wide-band horns, the minimum width of the beam's $\frac{1}{e}$ contour (the beam waist) is located in the throat of the horn and is given by: $w_0 = \frac{\lambda_o}{\pi\theta_0}$. For the POLAR horn, $\Delta \simeq 0.6$, placing the phase center closer to the aperture than to the apex, resulting in a frequency dependent beam size as summarized [8]in table 4.4.1.

---

[8]The author wishes to recognize the Herculean efforts of Chris O'Dell and his assistant Kip Hyatt for producing outstanding measurements of the K_a band beam parameters (and figure 4.3), as well as Nathan Stebor who assisted the author in earlier pioneering, though less-sophisticated, beam pattern

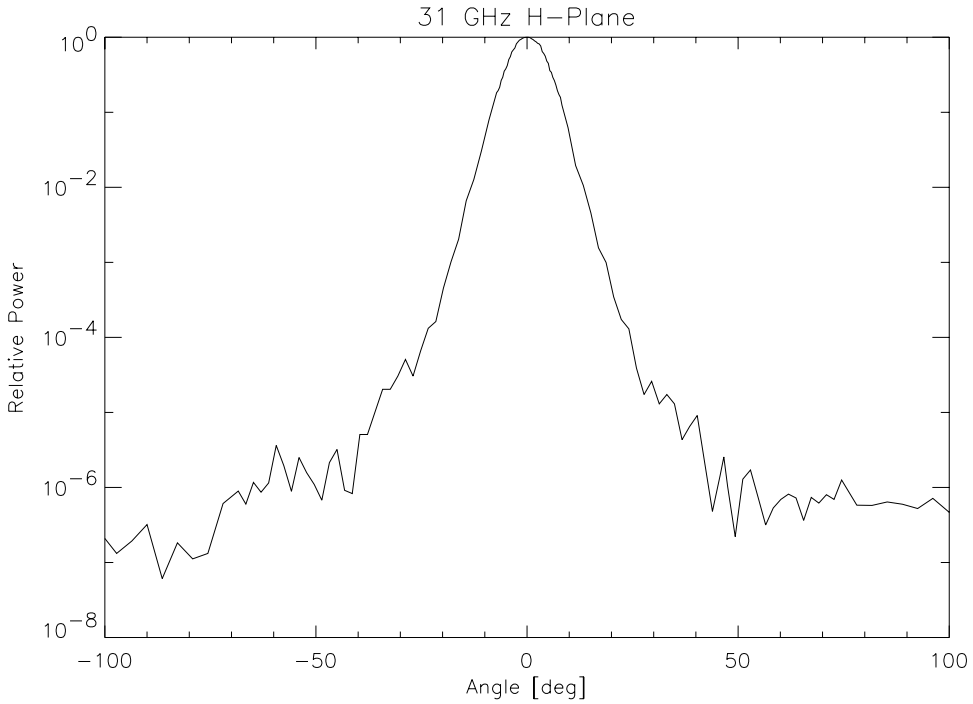

Figure 4.4: The POLAR $K_{\rm a}$-band 31 GHz (middle frequency band) H-Plane Beam Pattern is shown. The E-Plane beam map is similar to within $\sim 1\%$ out to ~ -20dB $\Rightarrow 30^{\circ}$.

Table 4.2: POLAR $K_{\rm a}$-Band Measured and Modeled FWHM Beam Widths.

Plane	ν [GHz]	$\theta_{fwhm} \pm 0.1^{\circ}$
E	26	7.9°
E	29	7.6°
E	36	7.1°
H	29	7.5°
H	36	6.9°

4.4.2 Optical Cross Polarization

As mentioned above, the corrugated scalar feed horn boasts a low-level of cross-polarization. The cylindrical symmetry of the feed might lead one to expect that the cross-polarization of the horn should be identically zero. However, even for a perfectly designed, completely symmetric feed, this is not true. The reason for this is grounded in the geometry of the horn and source when treated as a scattering problem.

Define the (x,y) plane to be the aperture plane, and ϕ to be the angle measured clockwise from the y-axis in the aperture plane to the polarization axis of the field. We first consider a field polarized along $+\hat{y}$,and the $x-z$ plane to be the scattering plane. Let $+\hat{k}$ be the wave-vector, and $\Theta(\theta,\phi)$ be the angle between $-\hat{x}$ and $+\hat{k}$. $\Theta(\theta,\phi)$ can have both polar angle, θ, and azimuthal angle, ϕ dependence. Treating the wall of the horn as a perfectly smooth conductor,[9] we find that for this scenario, the reflected field has the same polarization after scattering, independent of $\Theta(\theta,\phi)$. Thus, for an ideal horn, the cross- polarization induced by scattering in a plane containing the polarization axis is identically zero since there has been no polarization conversion. This is also manifestly true for scattering in a plane perpendicular to the polarization axis.

Now consider an incident field, again with a polarization in the $+\hat{y}$ direction, but now impinging on an element of surface area at an angle $\phi = 45°$. Using the fact that the electric field inside the conductor vanishes we obtain conditions on the reflected field's parallel and perpendicular components to the surface, $E_{\perp}$, vanishes and we find that there

---

measurements.

[9]Of course this is only strictly true for an un corrugated feed, but as we have shown, in the flare section of the horn the corrugations are $\lambda/4$ in depth, causing the field to be 180° out of phase after traversing one corrugation. This condition is identical to that of scattering from a perfect conductor, so our approximation here is reasonable.

is polarization conversion. For such a field we find that the incident field's y-component will be converted to an x-component upon reflection, thus producing a polarized signal in the cross-polarization direction, $\hat{x}$. The magnitude of the induced cross-polarization will vary as $\sin^2\phi$, and will be peaked at $\phi = 45°, 135°, 225°, 315°$.

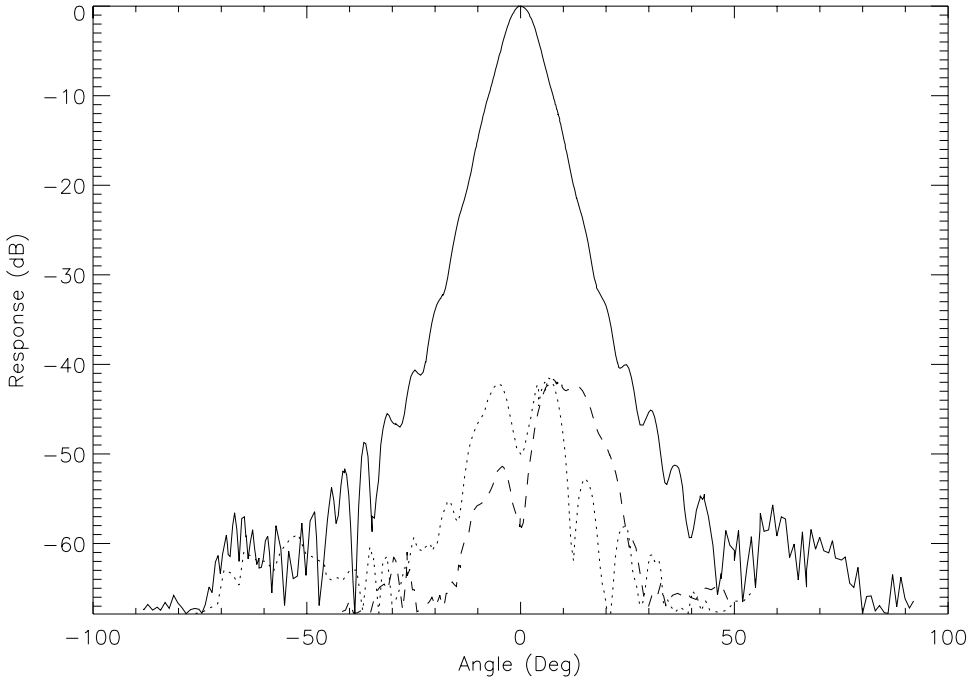

Figure 4.5: 29 GHz Cross-Polarization Beam Map. Here the solid line is the co-polar E-plane (field parallel to the $+\hat{\theta}$ direction) power response pattern, the dotted line is the cross-polarization response as measured along the azimuthal direction, $\hat{\phi}$, and the dashed line is the cross-polarization measured along $\hat{\theta} + \hat{\phi}$. As mentioned in the text, both cross-polarization responses should vanish at $\theta = 0$.

4.4.3 Orthomode Transducer: OMT

Following the throat in the optical path, there is an electroformed adiabatic[10] transition from the throat's circular output waveguide to the square-input waveguide of the OMT. This device was designed by application of the Pyle Condition, which seeks to match the

[10]See [78] for useful definition of adiabaticity as applied to waveguide transitions

cutoff wavelengths of the $TE^{\square}_{10}$ and the $TE^{\circ}{}_{11}$ modes [79]. The transition was manufactured by Custom Microwave Inc., of Longmont, CO.

The OMT[11] is a waveguide device used to separate the two linear polarization states in the incident field. POLAR's OMT was fabricated by Atlantic Microwave[12], and is a three-port device with a square input port, and two rectangular output ports containing the orthogonal polarization signals.

Although not strictly representative of POLAR's OMT, the paper by Chattopadhyay [80] presents an equivalent circuit model of a functionally equivalent device. The OMT's entrance port is K_{a} band square guide which supports both $TE^{\square}_{01}$ & $TE^{\square}_{10}$ modes simultaneously. Inside the square guide is a thin septum which behaves as a 3-dB power divider for the $TE^{\square}_{10}$ mode, and reflects the $TE^{\square}_{01}$ mode towards a short-slot coupling port transverse to the incident field. The slot is often reduced in size by the addition of an inductive iris to improve coupling to the $TE^{\square}_{01}$ mode, and reduce the coupling to the $TE^{\square}_{10}$ mode. To compensate for the added reactance of the iris, a canceling (capacitive) reactance is added in parallel [80]. See table 4.3 for a summary of POLAR's OMT properties.

Table 4.3: Properties of POLAR's OMT: Atlantic Microwave Model 2800.

Property	Value	Notes
Isolation	-35 dB	Specified and Measured
VSWR	< 1.2	Specified and Measured
Cross-polarization	-30 dB	Estimated

[11]Variously referred to in the communications literature as: polarization diplexers, dual-mode transducers, ortho-mode tees, and orthomode junctions. Communications applications use these devices to broadcast and separate channels which share identical bandpasses. SATCOM TV applications, broadcast odd TV channels in one polarization, and even TV channels in the orthogonal polarization.

[12]Boston, MA

Non-Beam-Forming Optics: Vacuum Window and Ground Screens

The vacuum window is given the task of allowing radiation to land on our detectors, while keeping the innards of the radiometer cool and pressure-free. To this end, a sophisticated multi-element approach was adopted. The window was designed by Chris O'Dell, and based on the extensive investigations of Peter Timbie's MSAMII/Top Hat work. The main features of the window are a 3 mil vacuum-tight polypropylene vacuum barrier and non-vacuum-tight Gore-Tex window support which bears the several hundred pounds of force on the window. A layer of Volara[13] (expanded polyethylene) serves to seal in a dry-nitrogen layer between the polypropylene layer and any precipitable water vapor in the atmosphere which would otherwise condense and freeze on the vacuum window. The window is exceedingly leak-free, allowing pressures of $< 10^{-5}$ Torr to be maintained for *months* at a time.

The final pseudo-optical elements of the POLAR instrument are its two concentric ground screens, see figure 4.6. The use of two ground screens is not unusual in the field, although POLAR's screens are optimized to reject polarized spillover, rather than total-power spillover.

The theory of ground screen operation is quite simple: one attempts to steer the power received in the sidelobes of the optical system to a well-known, constant, and preferably low-temperature source, rather than allowing them to land on the earth's 300K surface. It is essential that the sidelobe response not be modulated by the instrument's modulation scheme or else synchronous signals will be produced which, in principle, are indistinguishable from the feeble cosmic signals we are attempting to measure.

---

[13]Voltek Corp.

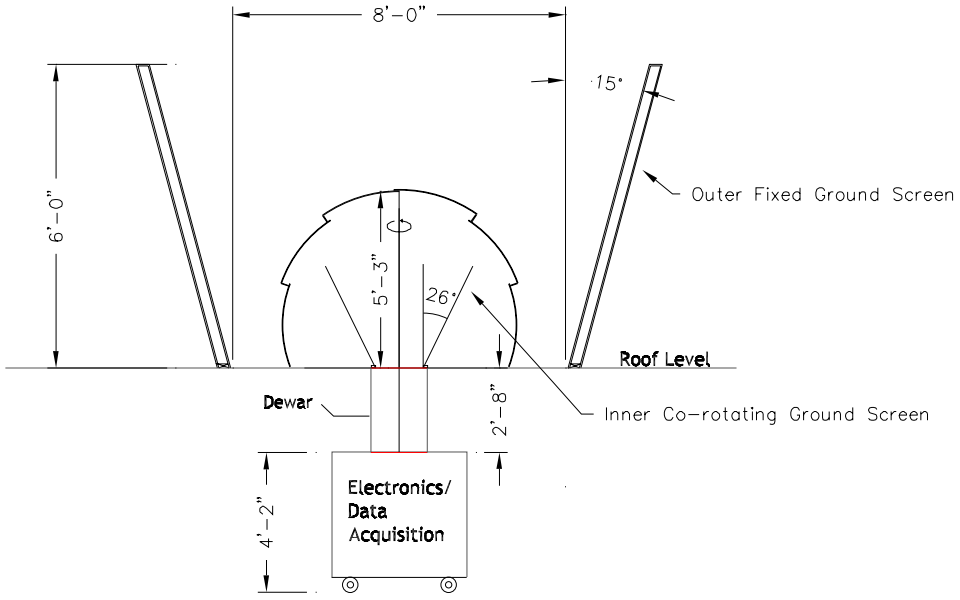

Figure 4.6: POLAR's Groundscreens. Two sets of ground screens are used to reduce the polarized spillover from the earth, as well as polarized emission from the shields themselves. The outer shield is fixed to the structure in which POLAR resides, and is composed of a lightweight steel skeleton covered by 0.05" aluminum sheets. The inner ground screen is covered with flat Eccosorb panels (to reduce their polarized emission), and co-rotate with the POLAR radiometer. Also shown is the motor-driven, fiberglass clamshell-dome which can be remotely operated via the World Wide Web in the event of inclement weather.

POLAR's ground screen approach is dual-purposed. First an inner conical ground screen rotates with the instrument and is coated with Eccosorb. The Eccosorb panels absorb, rather than reflect the sidelobes to the sky. This absorptive approach is uncommon in CMB anisotropy experiments as it increases the total power loading on the detectors, which is particularly troublesome in the case of ultra-sensitive bolometric detectors. However, we estimate that the antenna temperature of the inner shield to be < 1K. Polarization generated by emission from the bare metal surface of the uncovered shield is believed to be much more troublesome than the slight increase in system temperature. Additionally POLAR's inner ground screen co-rotates with the receiver, which ensures that if there is any residual polarized power produced by the inner screen, it will produce a constant polarized offset, rather than a less-tractable, rotation-modulated offset.

The second level of shielding is of the more conventional reflective-scoop design, *e.g.* Wollack [17]. The scoop[14] is mounted to the side of the POLAR observatory, and is made of aluminum panels 8' wide and 6' high. To estimate the level of sidelobe suppression induced by this shield we have employed Sommerfeld's diffraction calculation for points deep in the shadow region of a knife-edge scatterer [56]. We estimate the suppression to be ~ -40 dB, which in combination with a similar (measured) figure from the inner ground screen, and the low-sidelobe response of our feed horn, gives a total estimated sidelobe suppression of over -100 dB. We note that the diffraction calculations employed throughout the design process were based on scalar diffraction theory rather that the more complete vector theory, which is most appropriate for a polarization experiment.

[14]designed and built by Nathan Stebor and Kip Hyatt

4.5 HEMT Amplifiers

The development and implementation of wide-band low-noise amplifiers has revolutionized the field of coherent CMB radiometry. There exist no commercial devices which can match the performance of the amplifiers produced by the National Radio Astronomy Observatory (NRAO), under the direction of M.W. Pospieszalski and W.J. Lakatosh. Current devices, capable of up to 20 GHz bandwidths with noise temperatures lower than 50 K, are available for all waveguide bands up to W-Band (75 - 110 GHz).

The POLAR $K_{\rm a}$-band HEMT amplifiers were constructed in the Fall of 1994 and are no longer considered "state-of-the-art". Our amplifiers are based around HFET transistors produced by Hughes Electronics.

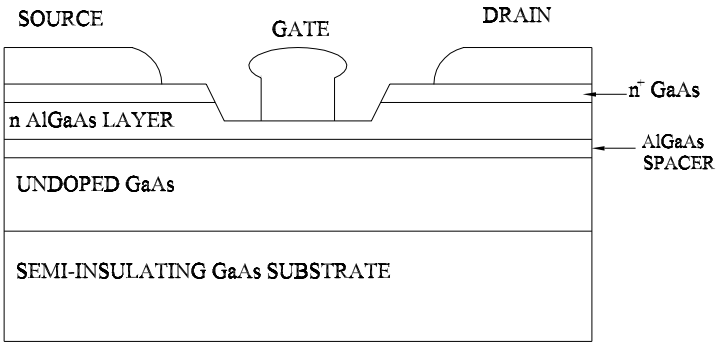

Figure 4.7: HEMT Structure

A generic structure is shown in figure 4.7. The HFET itself has electron 2DEG sheet densities of $\sim 10^{12}\mathrm{cm}^{-2}$, and a mobility of $10^4 cm^2/Vs$, thus justifying the name *High* Electron *Mobility* Transistor when compared with the mobility of a "garden-variety" low-frequency, coolable, low noise FET, which has a mobility of $5 \times 10^3 cm^2/Vs$ and noise

temperatures of $\sim 100 - 200$K. POLAR's NRAO amplifiers[15] are composed of four individual transistor stages, with the lowest noise device preceeding the following three. Each stage provides roughly 7-8 dB of gain, resulting in an overall gain of ~ 30 dB. Current amplifiers utilize InP based devices for the first stage (which have lower noise-temperatures than GaAs devices) at the expense of slightly increased $1/f$ noise. However, the low-frequency spectral properties of these amplifiers are largely irrelevant (at least in theory) for radiometers such as POLAR which employ the correlation technique.

NRAO supplied the amplifiers as well as support electronics which provide regulated voltages and currents to each of the four individual transistors. Supplied with the devices are data sheets which specify the NRAO-optimized values for the gate bias-current and the drain-source voltage. After tuning these parameters, the device's transconductance, $g_m = \frac{dI_d}{dV_{ds}}$ is completely determined. At a fixed V_{ds}, the noise temperature depends on the drain current weakly, but with a well-determined minimum. Unfortunately, this minimum noise-temperature current results in a rather low transconductance, and thus low-gain. So, an optimization is carried out in a two-dimensional parameter-space for each of the four transistors in each of the two POLAR HEMTS. With appropriate parameter tuning the devices can be used at room-temperature which is quite convenient for prototyping a radiometer while still in the user-friendly confines of the lab.

POLAR's two amplifiers had noise temperatures of ~ 65 K when measured at NRAO 5 years ago. Currently we measure the noise temperature of the entire system, which includes contributions from numerous lossy and emissive components which preceed and

[15]Serial Numbers: A29 and A30

follow the HEMTs[16], to be: $\sim$ 75K (See Chapter 5). We can assume that the HEMTs dominate this value, though the aforementioned non-idealities of the system contribute $\sim$ 15 K. A future goal of the POLAR $K_{\rm a}$ band receiver is to obtain upgraded InP devices, which should decrease our system temperature by a factor of at least two.

4.6 Room Temperature Radiometer Box: RTRB

After amplification, the signals leave the dewar through custom-made coin-silver waveguides which route the signals along a complicated, bending 3D path from the HEMTs in parallel to 6" stainless steel waveguides which provide a thermal break from the 300K dewar walls to the 20K HEMTs. The stainless guides are bolted to a vacuum-tight $K_{\rm a}$ band waveguide feedthrough manufactured by Aerowave. Outside the dewar, straight sections of Rhodium plated, brazed-copper waveguides are used to compensate for the path-length differences between the two polarizations incurred by the 3D bends. As mentioned in Chapter 4, it is essential that the two signals traverse identical electrical path lengths so that the electric fields will be in-phase at the correlators. Finally, the waveguides enter the RTRB, where the signals are converted from waveguide to coax to match the inputs of the MITEQ [JS426004000-30-8P] $K_{\rm a}$-band warm HEMT amplifiers. These devices are based on HEMT technology just as the NRAO devices are, however their noise temperatures are significantly higher: $T_N^{MITEQ} \simeq$ 250K. To compensate, these devices outperform their more refined cousins in the following all-important qualities: gain, delivery time, and not surprisingly, price!

Following this second-stage of amplification, the signals are down-converted in fre-

[16] see Chapter 5 for a discussion on spurious loading introduced by these components.

quency by the superheterodyne components, as delineated in the following subsection.

4.6.1 Superheterodyne Components

We down-convert in frequency because the ultimate multiplication of the signals is most easily performed at the lowest tolerable frequency which still preserves the nominal 10 GHz bandwidth. Down-conversion maintains the bandwidth, and allows us to further amplify the signals before they are detected.

Superheterodyne techniques are common in almost all modern commercial communications applications, though in recent years they have been de-throned from their position as the CMB community's "receiver-of-choice" where they reigned in the 60's and 70's. We now present a brief review of the technique.

Following [70], we Fourier expand the input signal as:

$$A = \sum_{\nu_1}^{\nu_2} a_i \cos(2\pi\nu_i t + \phi_i), \tag{4.3}$$

and the local oscillator's pure-harmonic signal as:

$$B = b\cos(2\pi\nu_m t + \phi_m). \tag{4.4}$$

The low signal level output of the mixer is approximately: $(A+B)^2 = A^2 + B^2 + 2AB$, which is:

$$= \sum_{\nu_i=\nu_1}^{\nu_2} \sum_{\nu_j=\nu_1}^{\nu_2} a_i a_j \cos(2\pi\nu_i t + \phi_i)\cos(2\pi\nu_j t + \phi_j) + b^2\cos^2(2\pi\nu_m t + \phi_m) +$$

$$2b \sum_{\nu_i=\nu_1}^{\nu_2} a_i \cos(2\pi\nu_i t + \phi_i) \cos(2\pi\nu_m t + \phi_m). \qquad (4.5)$$

Using some simple trigonometric relations, we can conclude that the first term on the HRS of equation 4.5 contains terms:

- between $2\nu_1$ and $2\nu_2$
- between $|\nu_1 - \nu_2|$ and $|\nu_2 - \nu_1|$.

Term 2 contains the frequencies $2\nu_m$ and 0 (*i.e.*, DC), and the third term contains frequencies:

- between $\nu_1 + \nu_m$ and $\nu_2 + \nu_m$.
- between $|\nu_1 - \nu_m|$ and $|\nu_2 - \nu_m|$.

The IF port of the MITEQ [TB0440] triple-balanced mixer is transformer coupled and passes only frequencies between 2 - 12 GHz. The final spectrum of the "intermediate frequency" (IF) – *i.e.* down converted, port's output is:

$$b \sum_{\nu_i=\nu_m+\nu_a}^{\nu_m+\nu_b} a_i \cos[2\pi(\nu_i - \nu_m)t + \phi_i - \phi_m], \qquad (4.6)$$

which is a (scaled) replica of the input, RF, with an identical bandwidth, though now at lower frequencies: IF. The IF signal is subsequently amplified in the IF band to provide the appropriate bias power level into the multiplier. Each multiplier requires $\sim$ 6dBm, or 4 mW, of bias power to function as a bilinear multiplier. We must amplify the signal substantially to meet this requirement as the three multipliers are preceeded by a triplexer which attenuates each signal by a factor of three in power. We use two stages of IF amplification, again provided by MITEQ devices with 2-12 GHz band passes. The gain

of each device falls steeply above a frequency of $f_{3dB} \simeq 12$ GHz, attenuating any residual out-of-band frequencies which might otherwise be propagating in the coax transmission lines.

4.6.2 The Correlator

After mixing and IF amplification, the signals are frequency multiplexed by Reactel triplexers. The function of the triplexers is two-fold. First they serve to provide us with three (ideally) independent bands from which we may investigate the spectral behavior of our signals. Secondly, these devices allow us to "flatten" the gain of the system across the wide RF-bandwidth that we achieve with the HEMTs. This ensures that the *effective* bandwidth will not be reduced from its nominal specifications. Following the triplexers, the signals from the two polarization states are fed into three separate wide-band multipliers (one for each sub-band). The multipliers themselves are MITEQ [DBP112HA] double balanced mixers with RF band passes from 1-12 GHz and an IF bandpass from 0-500 MHz. The IF output port is not transformer coupled, and can thus propagate the DC signal proportional to the correlation between signals in the x and y polarization states.

Performance of an Ideal Multiplier

There are several ways to implement a correlator for use in a correlation radiometer [10], [62], [65], [63], [81]. POLAR utilizes a correlator based on Schottky-diode mixer technology. In this manifestation, the ideal correlator is realized by a double balanced mixer, a phase modulating element, and lock-in amplification. At the heart of the correlator is the wide-band double-balanced analog multiplier. This type of multiplier isolates both RF input ports from one-another, while the IF port is coupled to both. The primary

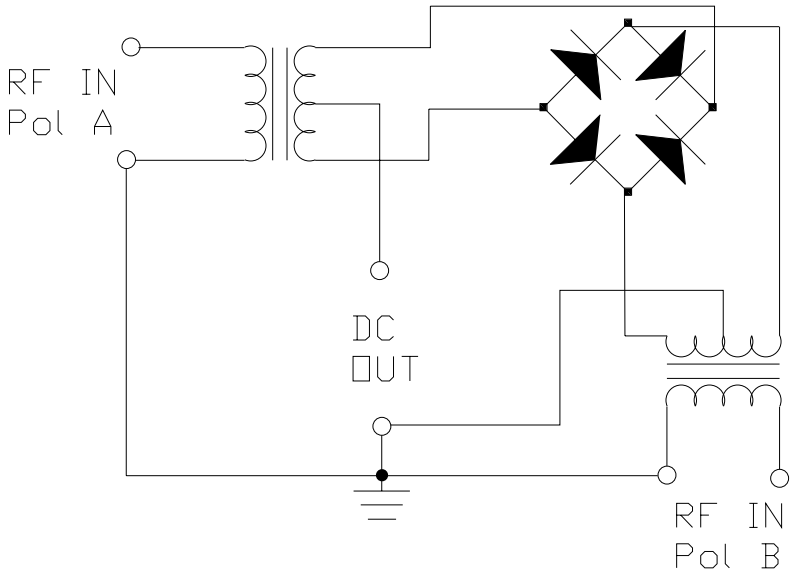

Figure 4.8: Electrical Schematic of Multiplier

difference between a multiplier and a conventional mixer is that the IF bandwidth is made intentionally narrow to suppress frequency components greater than ~ 100 MHz. As the RF ports have bandwidths from 1-12 GHz the narrow IF band prevents higher order terms than essentially DC from propagating in the output. In many circles, a narrow RF band multiplier is known as a 'phase detector', for reasons which will become apparent shortly.

The transformer coupled inputs coherently add the signals at both RF ports, traditionally labeled by 'L', for LO (*i.e.* Local Oscillator), and 'R', for RF. Due to the symmetrical arrangement of transformers and diodes, in practice, there is no electrical distinction between the two RF ports. A schematic of the multiplier is shown in figure 4.8.

The multiplying element itself is a bridge arrangement of Schottky diodes. The Schottky diode is a metal-semiconductor junction device with an I-V characteristic of:

$$I(V) = I_o(e^{\frac{\pm eV}{\eta k_b T}} - 1)$$

where I_o is the reverse saturation current, k_b is Boltzmann's constant, e is the charge of the electron, and $\eta \sim 1$ is the "ideality factor" parameterizing non-idealities of the junction. Following Maas [82], we model the diode as a current source, $I(V)$ in parallel with a junction capacitance, together in series with a resistor, R_s. The junction capacitance is:

$$C(V) = \frac{C_o}{(1 - \frac{V}{\phi_{bi}})^{\frac{1}{2}}}$$

where C_o is the junction capacitance with zero voltage difference, and ϕ_{bi} is the junction's built-in voltage. $C(V)$ is implicitly defined by:

$$C(V) = \frac{dQ_d}{dV}$$

where Q_d is the depletion-region charge. The capacitor's output current is:

$$I(t) = C(V(t)) \times \frac{dV(t)}{dt}.$$

We will also need the junction's conductance:

$$g(V) \equiv \frac{dI(V)}{dV} = \frac{-e}{\eta k_b T} I(V).$$

Now we can express the diode's output voltage as $V_{out} = IR_s = Z^{-1}V = YVR_s$, where Z is the equivalent circuit impedance, and Y is the corresponding admittance. We have that:

$$Z = (g + i\omega C)^{-1} + R_s,$$

so:

$$I(t) = \frac{R_s V(t)}{(g(t) + i\omega C(t))^{-1} + R_s}.$$

4.6.3 Multiplication

Expanding the ideal I-V curve for small junction voltages, we find that :

$$\mathbf{V_{out}(t)} \propto \texttt{constant} \ + \alpha \mathbf{V(t)} + \beta \mathbf{V^2(t)} + \ldots,$$

showing the non-linear dependence of $\mathbf{V_{out}}$ on V. Here, the amplitude terms in boldface are complex quantities, so we must pay attention to phases. For the mixer, $\mathbf{V} = \mathbf{V_{LO}} + \mathbf{V_{RF}}$ so that $V_{out} \propto |\mathbf{V_{LO}}|^2 + \mathbf{V_{LO}^* V_{RF}} + \mathbf{V_{LO} V_{RF}^*} + |\mathbf{V_{RF}}|^2$. The quadratic terms result in a DC component of magnitude $|\mathbf{V_{LO}}|^2 + |\mathbf{V_{RF}}|^2$, while the bilinear terms produce the desired "mixed" terms. In the case of the correlator, the DC component will also contain a contribution from the cross-correlated components of the signals at the RF and LO ports. We assume that $V_{out}(t)$ will be integrated, for a time period $2T$, which kills off the term linear in $\mathbf{V(t)}$.

For the bilinear terms we have:

$$\langle \mathbf{V_{RF}(t) V_{LO}^*(t-\tau)} \rangle = \lim_{\mathbf{T}\to\infty} \frac{\mathbf{1}}{\mathbf{2T}} \int_{\mathbf{-T}}^{\mathbf{T}} \mathbf{V_{RF}(t) V_{LO}^*(t-\tau) dt}. \tag{4.7}$$

We now choose an explicit representation for the signals:

$$\mathbf{V_{RF}}(\omega, \mathbf{t}) = \mathbf{V_{RF}} \mathbf{e}^{\mathbf{i}(\omega \mathbf{t} + \phi_{\mathbf{RF}})} \tag{4.8}$$

$$\mathbf{V_{LO}}(\nu, \mathbf{t}) = \mathbf{V_{LO}} \mathbf{e}^{\mathbf{i}(\nu \mathbf{t} + \phi_{\mathbf{LO}})}, \tag{4.9}$$

(4.10)

so equation 4.7 becomes:

$$V_{out}(\tau) = \tfrac{1}{2T}\langle \mathbf{V_{RF}(t)V^*_{LO}(t-\tau)}\rangle \tag{4.11}$$

$$= \lim_{T\to\infty} \int_{-T}^{T} V_{RF} e^{i(\omega t' + \phi_{RF})} V_{LO} e^{-i(\nu(t'-\tau)+\phi_{LO})} dt'$$

$$= \lim_{T\to\infty} \int_{-T}^{T} V_{RF} V_{LO} e^{i(\omega-\nu)t' + \nu\tau} e^{\phi_{LO}-\phi_{RF}} dt'$$

$$= \langle V_{RF} V_{LO}\rangle \delta(\omega-\nu) e^{i(\phi_{LO}-\phi_{RF}+\nu\tau)}$$

At zero lag ($\tau = 0$), the output is $\langle V_{RF}V_{LO}\rangle\delta(\omega-\nu)e^{i(\phi_{LO}-\phi_{RF})}$, showing that no output results when the RF and LO ports are at different frequencies. When the frequencies are matched, the output varies sinusoidally as $\cos(\phi_{LO} - \phi_{RF})$, justifying the name "phase detector" as mentioned above.

The above analysis has only treated a single frequency component. In practice both the LO and RF signals are composed of a finite band of frequencies:

$$\mathbf{V_{LO/RF}(t)} = \int_{\nu_o}^{\nu_o + \Delta\nu_{RF}} \mathbf{V_{LO/RF}}(\nu, \mathbf{t}) \mathbf{e^{2\pi i \nu t}} \mathbf{d}\nu. \tag{4.12}$$

Substituting the above into eq. 4.11, we find:

$$R_{LR}(0) = \int_{\nu_o}^{\nu_o+\Delta\nu_{RF}} \langle \mathbf{V_{LO}}(\nu)\mathbf{V^*_{RF}}(\nu)\rangle \cos(\phi_{\mathbf{LO}}(\nu) - \phi_{\mathbf{RF}}(\nu))\mathbf{d}\nu. \tag{4.13}$$

Performance of the Non-Ideal Correlation Radiometer

The simplest non-ideal behavior of the correlation radiometer is the effect of electrical path length mismatch between the input arms. From eq. 4.11 the correlator's DC output is proportional to $\cos(\phi_{LO} - \phi_{RF})$. If the phases themselves are frequency dependent, as in the case of a path length mismatch, then the DC output of the correlator will be reduced by the cosine term. The path length difference ΔL introduces a dispersive phase shift via: $\phi(\omega, \Delta L) = 2\pi\Delta L/\lambda_{guide} = 2\pi\frac{\Delta L \nu_g}{c}$. From eq. 4.13, we have:

$$R_{LR}(0) = \int_{\nu_o}^{\nu_o+\Delta\nu_{RF}} V_{LO}(\nu,t)V_{RF}(\nu,t)e^{2\pi i(\omega)t}\cos(2\pi\frac{\Delta L\nu_g}{c})d\nu. \tag{4.14}$$

The contribution of each spectral component is thus weighted by the cosine of its phase. Equivalently, the bandpass of the correlator is modulated by the cosine term. It is therefore imperative to accurately match the path lengths in the system. In practice this is accomplished by injecting a completely polarized signal into the OMT input which is swept in frequency across the RF band. By measuring the modulation of the spectrum of the correlator by the cosine envelope, we can determine the equivalent electrical path length imbalance. From these measurements one can also determine the bandpass of the correlation radiometer once it has been phase-optimized. The electrical path difference measurements agree quite well with measurements of the physical waveguide path difference. To balance the path lengths one simply adds the appropriate length of wave guide to the shorter arm of the receiver.

The remaining contributions to the non-ideality of the correlation radiometer result primarily from gain and phase asymmetry between arms, across the band passes. The effects can be caused by mismatched bands, temperature dependence, and phase instability

Table 4.4: Tolerances on Frequency Response Variations for a 2.5% Reduction in SNR

Type of Variation	Permissable Level
Amplitude Slope	3.5 dB across band
Sinusoidal Ripple	2.9 dB peak-peak
Inter band Centroid Offset	5% of $\Delta\nu_{rf}$
Phase Variation across band	12.8°

of the amplifiers and/or the correlator. In practice it is impossible to eliminate all such effects, and so in table 4.6.3 we provide an estimate of the tolerable level of a few of these effects such that they would contribute to a 2.5% degradation of the signal-to-noise ratio of the correlation receiver following Thompson et al. [60].

The final non-ideality of the correlation radiometer which must be confronted is its temperature dependence. There are two relevant effects caused by temperature fluctuations: gain instability and phase instability. Even for an ideal multiplier there is a DC component of the output which is proportional to the sum of the total RF power in each arm. Let us examine the effect of a change in the total power output (modulated, for example, by changing atmospheric antenna temperature, T) on the output from the correlator. We will assume that the radiometer is viewing an unpolarized source which produces fields $E_y(T)$ and $E_x(T)$, which are themselves functions of the ambient temperature. We will further assume that the feed horn is symmetric w.r.t. the E and H plane response and all band passes are identical between the two arms. The output from the correlator is given by:

$$V_{out}(T) \propto \langle |\mathbf{E_x(T)}|^{\mathbf{2}} + \mathbf{E_x^*(T)E_y(T)} + \mathbf{E_y^*(T)E_x(T)} + |\mathbf{E_y(T)}|^{\mathbf{2}} \rangle.$$

The two bi-linear terms in E_y, E_x vanish due to the uncorrelated assumption. The two quadratic terms survive and we assume that the audio frequency power spectra of the two

fields are given by:

$$S_\nu = \sqrt{\frac{E_o^2 \nu_{knee}}{\nu} + E_o^2}$$

where the frequency dependent term is caused by fluctuations in the power response due to temperature variations. Since this $1/f$ spectrum now appears in our multiplier output, it too will have a $1/f$ spectrum; apparently defeating the purpose of utilizing the correlation technique in the first place! There are two methods to remove the contribution from the total power channels. One is a hardware based approach, and the other is based on software removal of the total power contribution. In the final analysis, POLAR incorporates techniques from both approaches to achieve a high-level of suppression of residual contamination from the effects of the earth's atmosphere.

Software Based Solution to Correlator Drifts

The software-based solution does not utilize the phase modulator. Instead, the DC output from the correlator is measured, including correlated and uncorrelated contributions. After binning the correlator signal and both total power signals, fits are performed to the correlator output and the best-fit reconstructions of the total power signals are regressed out of the correlator signals. This technique removes most, but not all, of the total power, $1/f$ contaminated, contributions to the correlator output. The primary reason limitation is that in practice the sampling of the detector outputs is not sufficiently fast to accurately sample the total power channels which have $\nu_{knee} \sim 4$ Hz. We would need to sample the detectors much faster than $2\nu_{knee} \sim 10$ Hz to avoid aliasing. However, our audio bandwidth is $0 - 5$ Hz, so we would certainly lose high-frequency information from the total power channels simply by our choice of integration and data acquisition methods. To

address this problem we bin the raw total power output at 1 sample/.05 seconds to 1 sample/.5 seconds , which effectively introduces a low-pass filter into our data stream at ~ 2 Hz. Thus we lose information at timescales shorter than approximately twice the bin size, which certainly excludes a large portion of the HEMT low-frequency power spectrum.

However, the software solution offers a great deal of flexibility in the analysis, and has been applied with success in the anisotropy detections by Femenia et. al [83]. Additionally, we avoid the offsets which are associated with adding active components, such as the modulator, with its attendant differential loss. We have simulated the performance of the DC offset removal technique in various scenarios. First, we generate random, noise like, data representing signals for TP0 and TP1. Then we can simulate a correlator signal with and without a component which possesses a variable amount of correlation with the total power channels. We can then observe the power spectra of the correlator before and after regressing out the correlated component. In all cases the technique reduces the RMS fluctuations from the simulated correlator output. Note that since this simulated data is white noise it is not an accurate representation of the actual signals in the real radiometer. Therefore we also need to test our technique on real data taken while viewing the sky or a temperature stabilized black-body calibrator. The latter measurement only contains fluctuations from the radiometer, while the former contains contributions both from the radiometer and the atmosphere.

Hardware Based Solution to Correlator Drifts: Phase Modulation

The hardware-based solution places a phase modulator in one arm of the local oscillator stage. The phase is square-wave chopped from 0 to π at 1024 Hz. This has the effect of modulating *only* the correlated component of the RF fields before the mixers at an AC

frequency which is much higher than the $1/f$ knee of the total power channels, dominated by the HEMTs themselves. The signal out of the correlator is then demodulated at the chop frequency of the phase modulator using standard lock-in techniques.

POLAR's implementation of the phase modulation technique employs:

- an analog multiplier (MITEQ Model DBP0112HA2)
- an electronic $0^\circ - 180^\circ$ phase shifter (Pacific Millimeter Products)
- a switch-referenced synchronous demodulator detector and integrator (Analog Devices AD 630)

The implementation of the technique requires not only multiplication but also phase switching and phase-sensitive detection (lock-in). In doing so, we eliminate the $A^2 + B^2$ terms in equation 4.5 which correspond to the sum of the total power in both polarizations. These signals appear at DC, and do not survive the lock-in process. The output of the lock-in detectors is proportional to only the correlated component common in each arm of the polarimeter. In practice, the phase of the square-wave chop signal switch is slightly out of phase with the signal appearing at the lock-in signal input. This undesired phase shift is caused by propagation delays in the system, and any parasitic reactance (inductance or capacitance) in the multipliers themselves, or in the subsequent stages of audio-band signal conditioning. We AC couple our correlator signals before amplification in the second gain stage of the pre-amps. We do not low-pass filter the correlator signals in the audio pre-amp; if we did the correlator signal would appear as if its high-frequency components were rolled-off (the high-frequency "corners" of the ideal square-wave modulated signal would be slightly rounded-off, equivalently introducing a phase shift prior to lock-in detection).

The parasitic reactances mentioned above effectively convert a portion of the sig-

nal's in-phase component to an 90° out-of-phase component (which we call "quadrature-phase"). If we used only one lock-in, referenced to the nominal "in-phase" of the phase switch, we would lose information on the correlated component of the signal. To recover this information, we utilize two lock-in detectors per correlator, one in-phase with the chop, and the other quadrature-phase component. See figure 4.9.

Once the phase shifter is supplied with its square-wave current chop signal the actual choice of lock-in technique is either hardware based or software based. The common problem is to find the optimum reference phase for the phase sensitive detector, which is implemented in hardware or in software. A poor reference waveform will reduce the signal-to-noise (SNR) of the system considerably (see the following subsection for a discussion of the lock-in amplifier's SNR). The lock-in signal, being a complex quantity, has an associated modulus and phase. The real and imaginary components must be completely determined to recover the underlying signal.

Both approaches have advantages and disadvantages. The software based solution acquires the signal directly from the pre-amps, and then performs a best-fit to the phase of the (known) phase-shifter drive signal. This technique has the advantage that the reference frequency is easily modified as systematics warrant. Its main disadvantages are:

- there must either be a significant amount of correlated signal such that the correlated component's modulation is easily resolved from the noise; or, in the case that the real-time correlated signal's phase is buried in the noise, the phase solution obtained from a source with a large correlation between arms must be trusted to be constant between calibrations (which may be days apart).

- for a high frequency phase switch, the detector output must be sampled faster than at

least twice the phase-shift frequency. The phase switch frequency is usually a factor of ~ 10 higher than the $1/f$ knee of the first-stage amplifiers, which in POLAR's case would require a sampling frequency of $2 \times 10 \times \sim 5Hz\sim 100$Hz. For the roughly 10 channels of data and housekeeping this results in an effective data rate of ~ 100 Kb/S or roughly 1 GB per day which is rather impractical to reduce, unless the software is performed in real time. However, with 8 data channels sampled at 1 KHz, this too is impractical.

Lock-In Detectors

To implement the "hardware-based solution", a custom lock-in detector was constructed. The detector is centered on the AD630 Synchronous Modulator/Demodulator chip. Signals leave the pre-amp card and enter a separate RF tight box containing six separate lock-in circuits. The number "six" corresponds to phase sensitive detection of three correlators, each with two reference phases, "in-phase" and "quadrature-phase" . After multiplication of the pre-amp output signal by the two reference waveforms, the resulting product is low-pass filtered at 5 Hz, which also serves as our anti-aliasing filter for our 20 Hz DAQ sampling system.

For diagnostic purposes, we have an additional variable-phase reference signal which can be used in place of the fixed phase reference signal into the AD630. This gives us the flexibility to "tune" the phase of the reference signal such that the quadrature phase component of the correlator output can be nulled. For observations, we reference the lock-ins to either the fixed in-phase or quadrature-phase waveforms. Our phase-switch driver circuit produces both the in-phase and quadrature phase reference waveforms. We are able to change the phase of the reference waveforms with respect to the physical chop

waveform by discrete steps of 0.18°. This technique allows us to maximize the signal-to-noise ratio of the correlator channels as well as to remove any signal component from the quadrature phase detectors providing us with extremely powerful monitors of the noise of the correlator channels.

We have measured the complex transfer function of the pre-amps to determine both their voltage gain and relative phase shift. The latter is especially important in the case of our phase-sensitive detection scheme outlined above. Any use of signal-conditioning elements, such as filtration, of the signal out of the pre-amps would contribute to a nontrivial phase shift between the correlator output and the signal waveform input to the AD630's. Such a phase shift would be disastrous if we were only measuring the real component of the lock-in signal. Our dual-reference phase approach solves this problem of course.

The output of the lock-ins with terminated inputs are measured to determine their offsets. This is done in addition to the corresponding measurement for the pre-amps. Furthermore, the transfer function of the pre-amps must be fully characterized in order to determined the effective integration time for each channel.

4.6.4 Electronics Box and Housekeeping

Thermal regulation of the RTRB is essential to the stability of the instrument over long periods of time. We have identified a number of components which are extremely temperature-sensitive. The most sensitive components are the non-linear devices such as the mixers/multipliers, and especially the Gunn Oscillator. To regulate the temperature we have constructed a thermal control circuit which employs feedback from a sensor inside the RTRB. This control circuit is centered on a commercial microprocessor-based PID control (OMEGA), and can regulate up to 300W of power applied directly to MINCO

Heaterfoil pads. The power and control of our approach allows us to regulate the temperature of all elements in the RTRB to better than 100 mK_{RMS} per-day.

We also monitor several other housekeeping signals, including: 4 Lakeshore # 10 temperature sensor diodes inside the cryostat (on the HEMTS, cold plate, and feed horn) and the dewar pressure. We employ a multi-stage power regulation approach, using precision voltage regulators and reference throughout the RTRB; all signal circuitry (HEMT bias cards, post-detection electronics, etc.) are double regulated and EMI shielded.

4.6.5 Post-Detection Electronics: PDE

The pre-amplifier is the final component of the signal chain for the total power detectors, and the penultimate component for the correlators as they are detected via the lock-in circuits described above. To minimize the susceptibility to electromagnetic interference (EMI), the signals are amplified and filtered before leaving the radiometer box. A single Vector card contains 5 identically constructed circuits, a single one of which is displayed in figure 4.9. The card is mounted in close proximity to the detectors and shares the same thermally regulated environment.

The first stage of the pre-amplifier consists of the gain stage set by a low-noise Analog Devices OP-27 Precision Op-Amp. The gain is adjustable by selection of the feedback resistor. Following the gain set stage is a 4-pole, 5Hz Frequency Devices Anti aliasing filter. The bandpass of the anti-aliasing filter also serves to set our fundamental integration time, τ. In order to measure the effective integration time we calculate the power spectral density (PSD) of the output of the pre-amplifier circuit with a 50Ω terminated input. The effective integration time is the time lag between which samples from the detector can be considered independent. Denote the voltage transfer function of the pre-amps/anti-

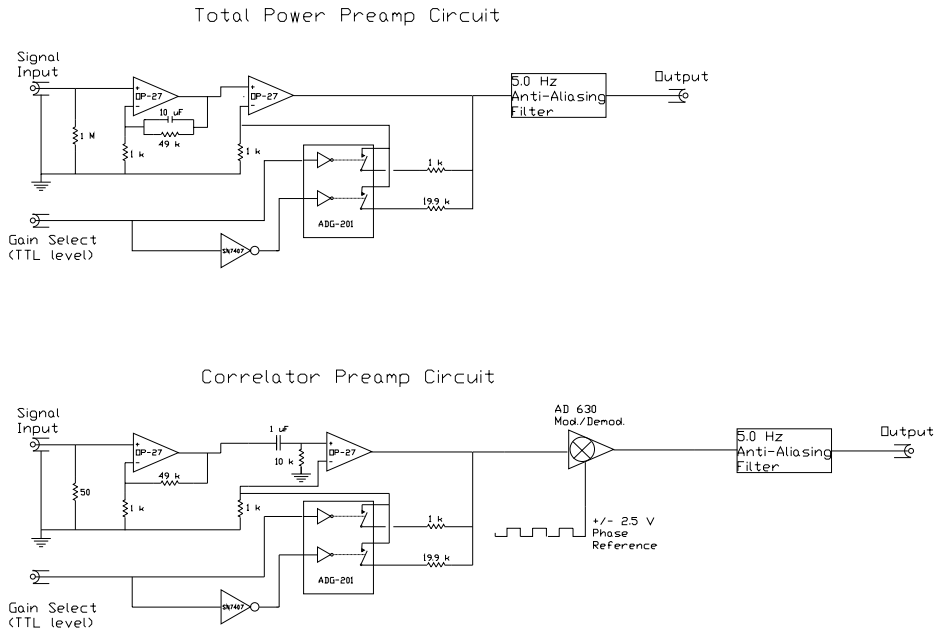

Figure 4.9: Post-Detection Pre-amplifier circuits for the total power channels (top) and the correlator channels (bottom). The overall gain of the pre-amps can be switched between low-gain (during calibration) or high-gain (during observations). The gain is controlled by a TTL signal supplied by the data acquisition system.

aliasing filters as $\equiv H(\omega)$. The power spectrum of $H(\omega)$ is $S_H(\omega)$. Then we have that:

$$\frac{1}{\tau_{PSD}} \equiv \frac{1}{S_H(0)} \int_{-\infty}^{\infty} S_H(\omega) d\omega = \frac{2}{S_H(0)} \int_{0}^{\infty} S_H(\omega) d\omega = 2\Delta\nu = \frac{2}{\tau}$$

.

We have that $\tau = 2\tau_{PSD}$. To convert Noise Equivalent Voltage (NEV) in $[V/\sqrt{Hz}]$ to $[V\sqrt{s}]$ we have: $NEV = \frac{S}{\sqrt{\tau}}$ where S is the PSD with units $[V^2 s]$. So if we are measuring the PSD and converting to NEV we have $NEV = \frac{S}{\sqrt{2\tau_{PSD}}}$, justifying the hitherto *ad hoc* practice of dividing PSD's by spurious factors of $\sqrt{2}$.

4.6.6 DAQ Hardware and Software

The data acquisition system is composed of three main sections:

- National Instruments DIO-MIO-16, 16 Bit Daqpad Analog-to-Digital Converter Module
- Compaq Pentium II notebook computer
- National Instruments Labview software

The main hardware constraint is that all components must rotate with the polarimeter, eliminating the use of a standard desktop computer for acquisition and storage purposes. The Daqpad is a compact 16-Bit, 16 channel (single-ended) analog-to-digital converter (ADC). It samples all 8 data channels as well as 8 housekeeping channels at a sampling rate of 20 Hz, which over samples the outputs from the detectors by a factor of 2 since the Nyquist frequency for our anti-aliasing filters is 10 Hz. The Daqpad interfaces to the notebook computer via a 1m parallel port interface cable. The Labview software is custom written to sample all channels at 20Hz. By sampling and storing all of the data in close physical proximity to the detectors, we minimize corruption due to RFI which might otherwise occur if the ADC took place off of the rotation platform.

The data files are indexed by calendar date, with several hundred files stored per day. After one day of acquisition, the data files are transfered from the rotating notebook computer to a desktop computer via a local area network Ethernet connection. The coax Ethernet connection leaves the rotating electronics box through 2 channels of a 10 channel shielded slip-ring (5th Dimension). No RFI is noticed during data transfer.

4.7 Rotation Mount and Drive System

Since POLAR's recovery of the Stokes parameters is based upon their modulation under rotations, we have constructed a 30" diameter bearing platform and AC motor system to

rotate the cryostat at 2 RPM ($\sim$ 30mHz see figure 4.10).

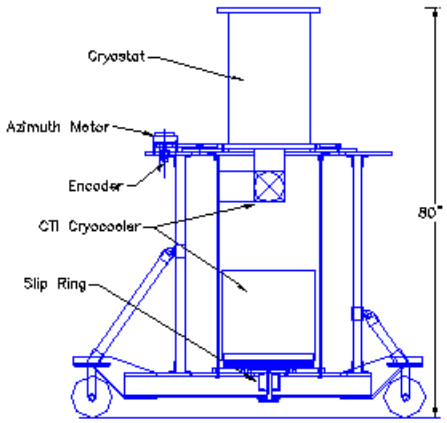

Figure 4.10: Rotation mount, showing motor, bearing, and encoder position. The wheels allow for fine positioning of the instrument on its platform, and are removed once the instrument has been aligned.

The AC motor is smoother than a stepper motor approach(which we tried originally), and is ideal for continuous rotation such as ours. The dewar bearing rides on a 0.100" stainless-steel ball-bearings in a lubricated channel, which contains about 400 balls. The motor pulley has a 1000 bit/rotation TTL compatible relative angle encoder which reads out the rotation angle. A custom made one-bit absolute encoder is triggered once per revolution at a specific angular position which serves to set the zero angle for the polarization

recovery.

4.8 Instrument Bandpasses

We present here a measurement of the bandpass of the instrument. For this measurement, an HP 83751A Synthesized Sweeper is used to produce a swept signal from 13 to 18 GHz, which is subsequently doubled in frequency by an active doubler (producing 26 - 36 GHz) and fed into a power spitter. The outputs from the power splitter are, of course, 100% correlated, and these signals are fed into the waveguide input ports of the RTRB. This allows us to measure the bandpass of all warm RF components. The correlated signals are attenuated by 60 dB to provide a power level similar to that obtained when viewing the sky.

To illustrate the bandpass measurement and phase chop method we refer the reader to figure 4.11 which shows a 600 MHz section of the bandpass of correlator J3 *before* lock-in detection. The phase switch is chopped at 1 KHz, causing sign reversal of the correlator DC output. This signal is subsequently fed into the lock-in detectors, and the DC level out is recorded to measure the response as the input signal is swept in frequency. All three correlator channels are measured this way, and the resulting bandpasses are shown in figure 4.12.

Table 4.5: Radiometer Centroids, Bandwidths, and Observing Sensitivities ($T_{Ant} \simeq 15$K)

Channel	$\nu_c[GHz]$	$\Delta\nu[GHz]$	$S_{sky}mk-\frac{1}{2}$
TP0	31.9	7.8	40.0
TP1	30.8	8.0	10.1
J3	28.0	1.2	8.5
J2	31.5	2.7	7.8
J1	35.0	2.9	4.5

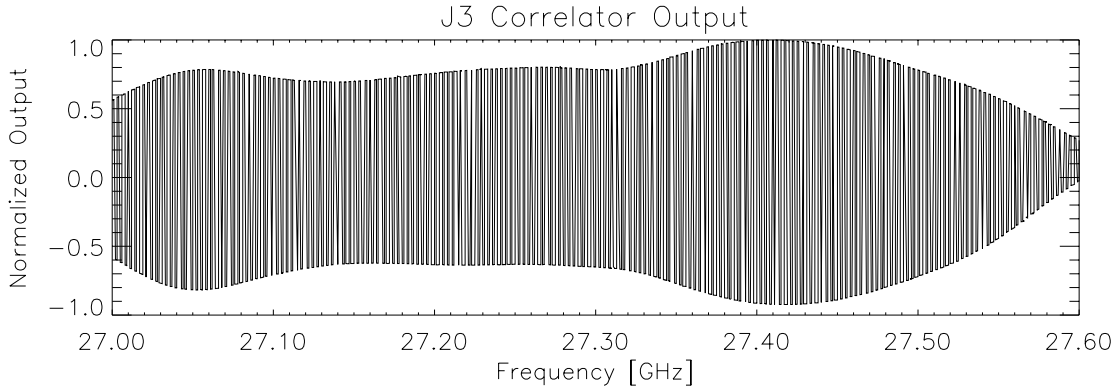

Figure 4.11: A 600 MHz section (out of 1.2 GHz) of correlator J3's band is shown. The modulation is caused by a square-wave phase chop of the local-oscillator signal. The low-frequency oscillation is the result of gain and phase variations across the band.

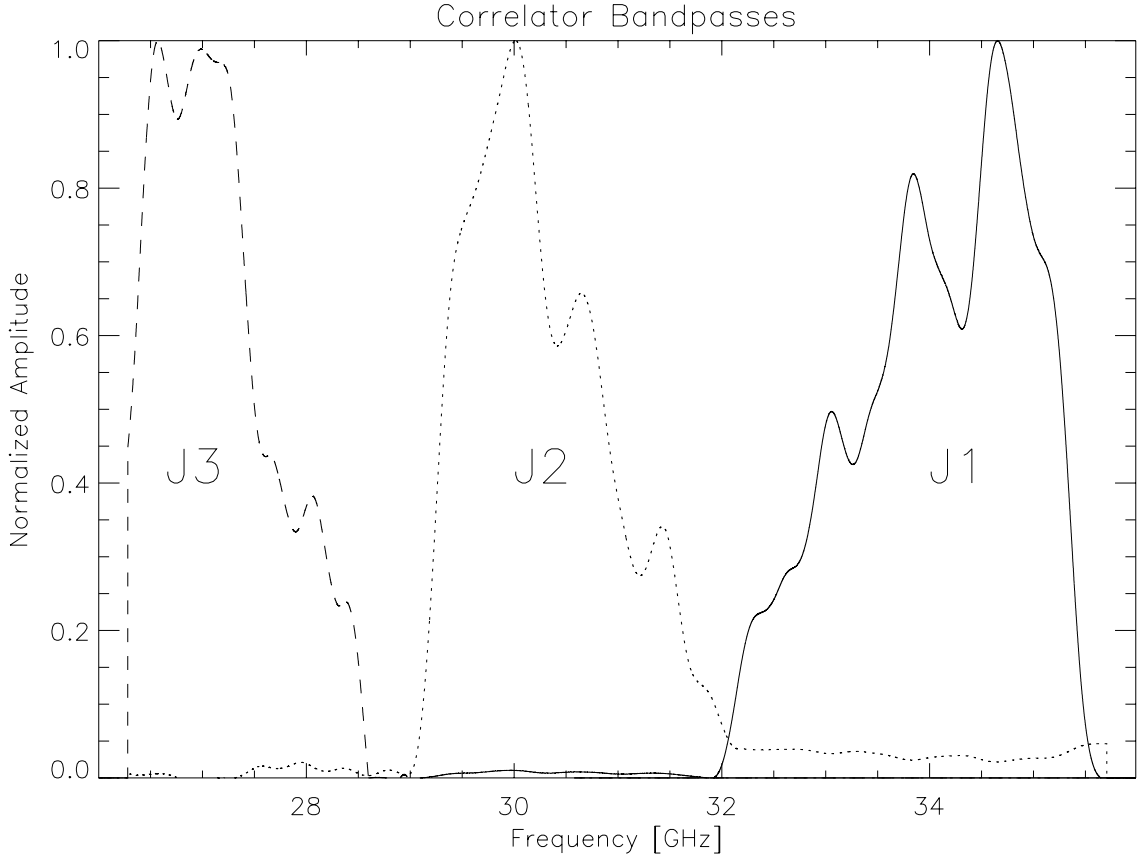

Figure 4.12: All three correlator bandpasses are shown. There is significant response to correlated signals over the full K_a band.

Table 4.6: POLAR K_a Band Radiometer Components

Device	Manufacturer	Model
Circular-Square Transition	Custom Microwave	—
OMT	Atlantic Microwave	OM2800
HEMTs	NRAO	A29 & A30
Warm RF Amps	MITEQ	JS426004000-30-8P
Mixers	MITEQ	TB0440LW1
Gunn Oscillator	Millimeter Wave Oscillator Co.	—
Warm IF Amps	MITEQ	AFS6-00101200-40-10P-6
Triplexers	Reactel	—
Correlators	MITEQ	DBP112HA
Total Power Detectors	Hewlett Packard	HP 8474C
Lock-In Amplifiers	Analog Devices	AD630
K_a band Phase Switch	Pacific Millimeter Products	—
Dewar	Precision Cryogenic Systems	—
Cryocooler	CTI Cryogenics	8500 Compressor, 350 Cold Head

Table 4.7: POLAR Observing Parameters

Parameter	POLAR 1999
Declination of Drift Scan	43.03°
Beam width	7°
Fractional Sky coverage	$255° \times 7° FWHM \simeq 5\%$
Rotation Rate	0.03Hz
Point Source Sensitivity	$0.7\mu K$ Jy^{-1}
Post detection Bandwidth	5Hz
Sampling Frequency	20 Hz

Chapter 5

Calibration

5.1 Calibration *desiderata*

An accurate calibration is essential to the success of the POLAR experiment. The ideal calibration source will allow us to determine the following quantities of interest:

- voltage-to-antenna temperature conversion coefficient for each channel
- system noise temperature for each channel
- minimum detectable polarized signal in one second of integration, the Noise Equivalent Temperature (NET), for all detectors
- offsets and long-term stability of our instrument

An ideal source would be a polarized astrophysical point source with enough power to be seen in "real-time". This would allow real-time beam-maps as well as calibration. We can estimate the necessary power such that a 5-σ detection is made in the fundamental 0.2 s integration period of the receiver back-end – which would be bright enough to see clearly in real-time.

The antenna temperature seen by POLAR's total power detectors when viewing a source of flux density $S(\nu)$ [Jy] is given by:

$$T(\nu) = S(\nu)\frac{c^2}{2k_b\nu^2\Omega_M} \times 10^{-26}K, \tag{5.1}$$

where k_b is Boltzmann's constant and Ω_M is the solid angle of the main beam. For POLAR, $\Omega_B = 0.047$sr, which implies an antenna temperature of 0.7μK for a 1 Jy source. Note that equation 5.1 holds for a single mode detector for a single polarization, as indicated by the presence of the factor "2" in the denominator. For a $10-\sigma$ detection, with a receiver whose $NET \simeq 3$ mK $\sqrt{sec}$, a source of antenna temperature $T_{Ant} \simeq 33$mK is required. This is equivalent to a 335 Jy source at 31 GHz. For comparison, Cas-A, the brightest known radio source, has a flux density of 206 Jy at 31 GHz. We note that this assumes we are measuring a change in antenna temperature by the source, not a polarized signal. Since the polarization of Cas-A is less than 10% at 31 GHz, for the polarization signal to be detected in real time would require a signal ten times larger! Clearly, we cannot expect to use an astrophysical point source for calibration of POLAR. We note here, for possible future relevancy, that Madison, WI is almost ideally situated for a zenith scan with a smaller beam size, for Cyg-A, the second most powerful radio source, lies at a declination of $\delta = 41^\circ$, placing it only 2° from the zenith. The polarization properties of Cyg-A have been measured at arcsecond scales at 15 GHz to be $\sim 10\%$, decreasing due to Faraday rotation to 2% at 5 GHz [84]. A sub-degree polarization experiment at 31 GHz could detect this object at the several$-\sigma$ level.

5.2 Twisted-Cold Load (TCL) Calibrations

For our initial laboratory calibrations we have developed an internal calibration method which produces a correlated electric field at the input to the orthomode transducer (OMT). The intensity of this field can be varied above 30 K, and produces a polarized signal at the input to the OMT which calibrates the entire radiometer from the feedhorn on. We call this calibrator the "Twisted Cold Load", or TCL, and it allows us to determine the radiometer's noise temperature, noise equivalent temperature (NET), and calibration coefficients.

The TCL is constructed from a section of circular copper waveguide, with castable Eccosorb epoxy CR-114 coated walls. The Eccosorb coats the walls in such a way as to maximize the number of reflections/absorptions for a wave incident on the calibrator. To accomplish this an "inverse-spike" geometry was adopted. The measured return loss across the K_{a} band better than -30 dB. A section of circular stainless-steel waveguide is attached between the load and the OMT to act as a thermal break, and a copper strap connects the load to the 20K cold stage (see figure 5.1).

The load is polarized by coupling its circular output flange to a WR-28 circular-to-rectangular transition, which acts as a polarizing filter. Following is a co-aligned rectangular-to-circular transition which then couples to the circular-to-square transition which feeds the OMT. By rotating the E-plane of the back-to-back transitions 45° with respect to the square aperture of the OMT we are injecting in a 100% correlated field into each port of the OMT. This allows us to have a temperature controlled thermal source, which mimics the effect a 100% polarized source would produce in our correlator channels. The rotation by 45° motivates the name of the device: the Twisted Cold Load (TCL).

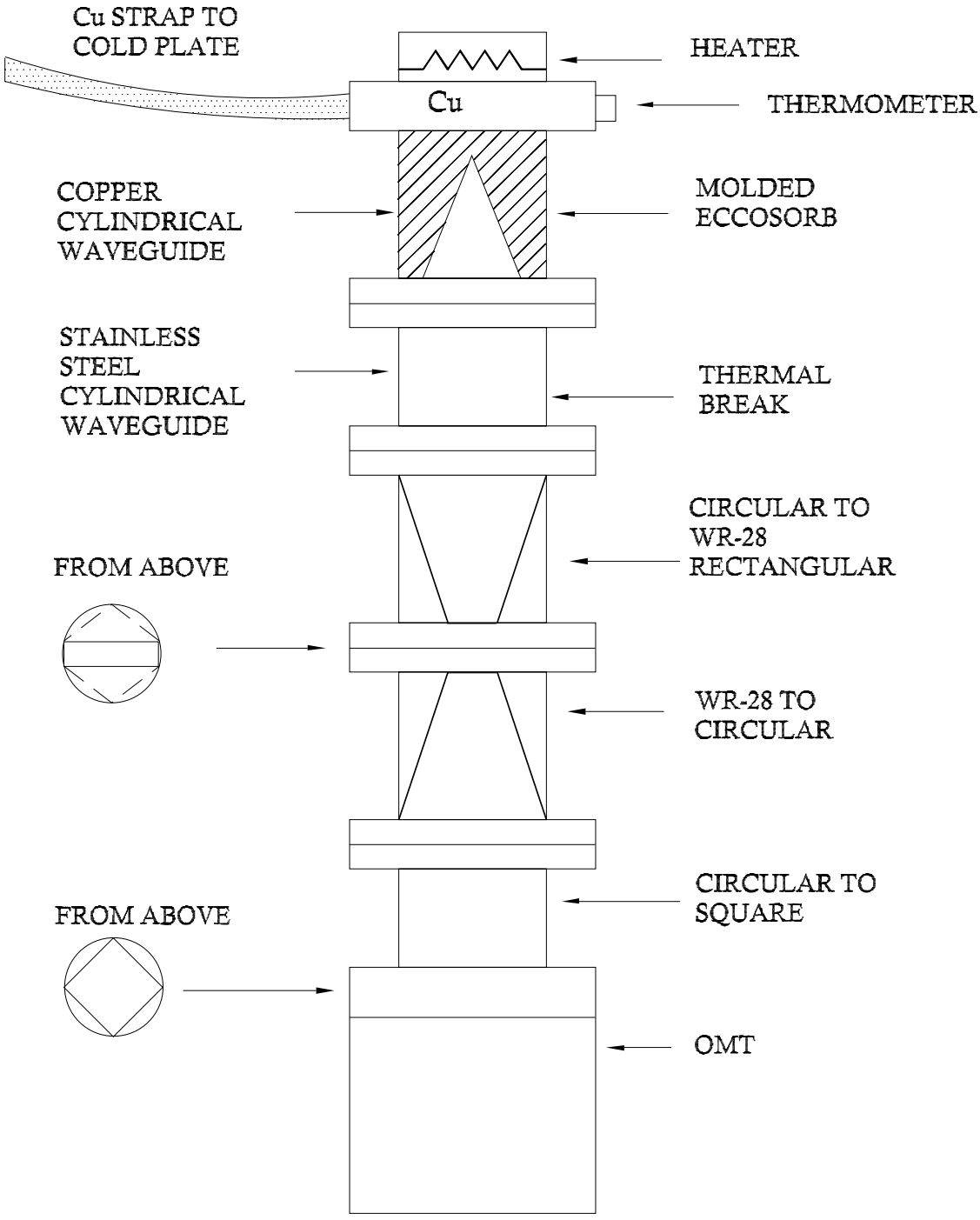

Figure 5.1: The Twisted Cold Load Calibrator (TCL). The antenna temperature of the load is varied by heating an Eccosorb loaded section of cylindrical waveguide. The back-to-back circular-to-rectangular waveguide transitions polarize the load along the E-plane of the rectangular waveguide. This plane is rotated along the main-diagonal of the OMT to produce correlated fields in the E and H plane output ports of the OMT.

This rotation affects the power ($\equiv$ antenna temperature) seen by both the total power detectors and the correlators. For the total power detectors, the use of the rectangular section of waveguide converts the dual-polarization circular waveguide into one which only propagates a single-mode. Because the load itself is unpolarized, and we accept only one polarization, we have cut the power into the OMT from $2k_bT_{load}\Delta\nu_{RF}$ to $k_bT_{load}\Delta\nu_{RF}$. The effect of the 45° twist is that the amplitude of the *field amplitude* delivered to each total power detector is reduced by $\cos 45^\circ = \frac{1}{\sqrt{2}}$. Thus a change in load temperature ΔT_{load} produces a change in the total power detected temperature of $\frac{\Delta T_{load}}{2}$.

For the correlators, the reduction in power is the same factor of two. The correlators multiply the field amplitude in each of the polarizations. Each polarization receives $\frac{1}{\sqrt{2}}$ of the field produced after the mode conversion. Multiplying these two factors in the correlators produces the same factor of two reduction as for the total power detectors.

5.2.1 System Noise Temperature

There are several methods to compute the noise temperature of the radiometer using the TCL or with several different temperature external loads. While the former method produces lower and more stable temperatures, the latter is much faster to implement, and also incorporates the effect of the feed horn. We have tested the TCL method vs. the ambient temperature external load method to ensure consistency. Further tests using the TCL are planned in order to obtain higher precision results at temperatures lower than the lowest temperature external load available: 77K. However, the noise temperature calibration results quoted in this thesis are obtained from the ambient temperature external load method.

Method 1: Y-Factor Measurements

For the total power channels we use a common technique to obtain a first-order estimate of the noise temperature of each arm of the radiometer. Given two load temperatures, T_H and T_C , and the corresponding DC voltages produced in the total power detectors, V_H and V_C, the y-factor is defined to be: $y = \frac{V_H}{V_C} = \frac{T_H+T_N}{T_C+T_N}$. Solving for the receiver noise temperature, T_N, we find:

$$T_N = \beta \frac{V_C T_H - V_H T_C}{V_H - V_C},$$

where $\beta = \frac{1}{2}$ for the TCL and $\beta = 1$ for the ambient temperature calibrations.

Method 2: Bandwidth Technique

Knowing the bandwidth $\Delta\nu$ of the system, the voltage fluctuations ΔV_{rms} in an integration time τ, and the calibration coefficient, g in [V/K] allows us to estimate the noise temperature of the receiver via the radiometer equation:

$$T_{sys} = \kappa g^{-1} \Delta V_{RMS} \sqrt{\Delta\nu\tau} - \beta T_{load}, \tag{5.2}$$

where $\kappa = 1$ for the total power channels, and $\kappa = \sqrt{2}$ for the correlator channels, and $\beta = \frac{1}{2}$ for the TCL and $\beta = 1$ for the ambient temperature calibrations.

Method 3: Linear Intercept Technique

For the two total power channels and the three correlators we can use the RMS noise on the DC detector voltages to determine the noise temperature. This method has the advantage that it does not require the knowledge of the radiometer's bandwidth. The

noise model for the total power detectors is:

$$\Delta T_{RMS} = \frac{T_{SYS}+\beta T_{load}}{\sqrt{\Delta\nu\tau}} \tag{5.3}$$

$$= \alpha T_{load} + \gamma, \tag{5.4}$$

while for the correlators we have:

$$\Delta T_{RMS} = \sqrt{2}\frac{\sqrt{(T_{SYS0}T_{SYS1}}+\beta T_{load})}{\sqrt{\Delta\nu\tau}} \tag{5.5}$$

$$= \gamma T_{load} + \delta. \tag{5.6}$$

Again, $\beta = \frac{1}{2}$ for the TCL and $\beta = 1$ for the ambient temperature calibrations.

We see that for both the total power channels and the correlators ΔT_{rms} is a linear function of the load temperature. The x-intercept of these lines will be equal to the negative of the system noise temperature. We note again that these results apply to the ambient load method, not the TCL method. For the TCL method it is necessary to incorporate the effect of the single-mode waveguide which reduces the load temperature seen by the detectors by a factor of two.

Noise Temperature Contribution from Lossy Components

The system noise temperature is dominated by the noise temperature of the HEMT amplifiers. However, the contribution of the following room-temperature amplifiers, as well as loss in components preceeding the HEMTS cannot be neglected. The dominant lossy

elements preceeding the HEMTs are the two PAMTECH cryogenic isolators and the dewar's vacuum window. The isolators' exact physical temperature is unknown, but we may estimate them to be at $\sim$ 40K, which is the physical temperature of the horn, so this is a worst-case estimate. Their insertion loss is: $L = 1/\epsilon_{iso} = 0.1dB = 0.03$, where ϵ_{iso} is the transmission of the isolator. The loss of the vacuum window is conservatively estimated at 1%. The noise contribution from amplifiers in series with the HEMTs are reduced by the gain of the HEMTS [20], which is why we put our best amplifiers first in the signal chain. The room temperature MITEQ amplifiers have noise figures of $F = 2.5dB = 1.8$ which translates to a noise temperature of $(F-1)290K = 232$K.

The total estimated system noise temperature including all of these additional factors is:

$$\begin{aligned} T_n &= T_{HEMT} + \frac{1}{G_{HEMT}} T_{MITEQ} + \Big(\frac{1}{\epsilon_{iso}} - 1\Big) T_{iso} + \Big(\frac{1}{\epsilon_{window}} - 1\Big) T_{window} \\ &= 65K + \frac{232}{316} K + 0.03 \times 40K + 0.01 \times 300K \\ &\simeq 70K, \end{aligned}$$

where the gain and noise temperature of the HEMTS have been taken from their specifications after construction at NRAO in 1994. This number agrees quite well with the measured values of T_n discussed below.

Results of Noise Temperature Measurements

Table 5.2.1 displays the noise temperature of the system obtained from the correlator channels quadrature-phase component using the linear intercept method outlined above.

Table 5.1: System Noise Temperature Obtained From Correlator Channels Using Linear Intercept Method

Channel	T_N from Linear Intercept
J1	64.7 K
J2	79.0 K
J3	77.4 K

A plot of the y-factor measurements for the three correlator channels is shown in figure 5.2. This figure allows us to obtain the system noise temperature derived from each correlator (x-intercept) as well as an independent measurement of each correlator's NET (y-intercept). Some compression can be discerned for the highest ambient temperature load used (300 K). Higher precision measurements using the TCL will be performed to obtain the lowest possible uncorrelated load temperatures ($\simeq$ 30K). The values of ΔT_{RMS} for correlators J1 and J2 agree quite well with the measured values from the PSD data discussed at the end of this Chapter. Correlator J3 shows the highest level of compression and not-coincidently, obtains the highest NET – a value inconsistent with the NET derived from its PSD.

5.3 Wire Grid Calibrator: WGC

While the TCL calibrations described above are the most accurate method to calibrate the detectors, the TCL does not accurately represent the true configuration of the radiometer as used during observations. The absence of the feed horn and vacuum window is a striking shortcoming of the TCL technique. Additionally, the TCL calibration method is time-consuming as it requires complete disassembly of the cryostat to install. Therefore, we require a calibration method which is easily implemented, and representative of the observations we are attempting to perform. The conventional approach to these issues for

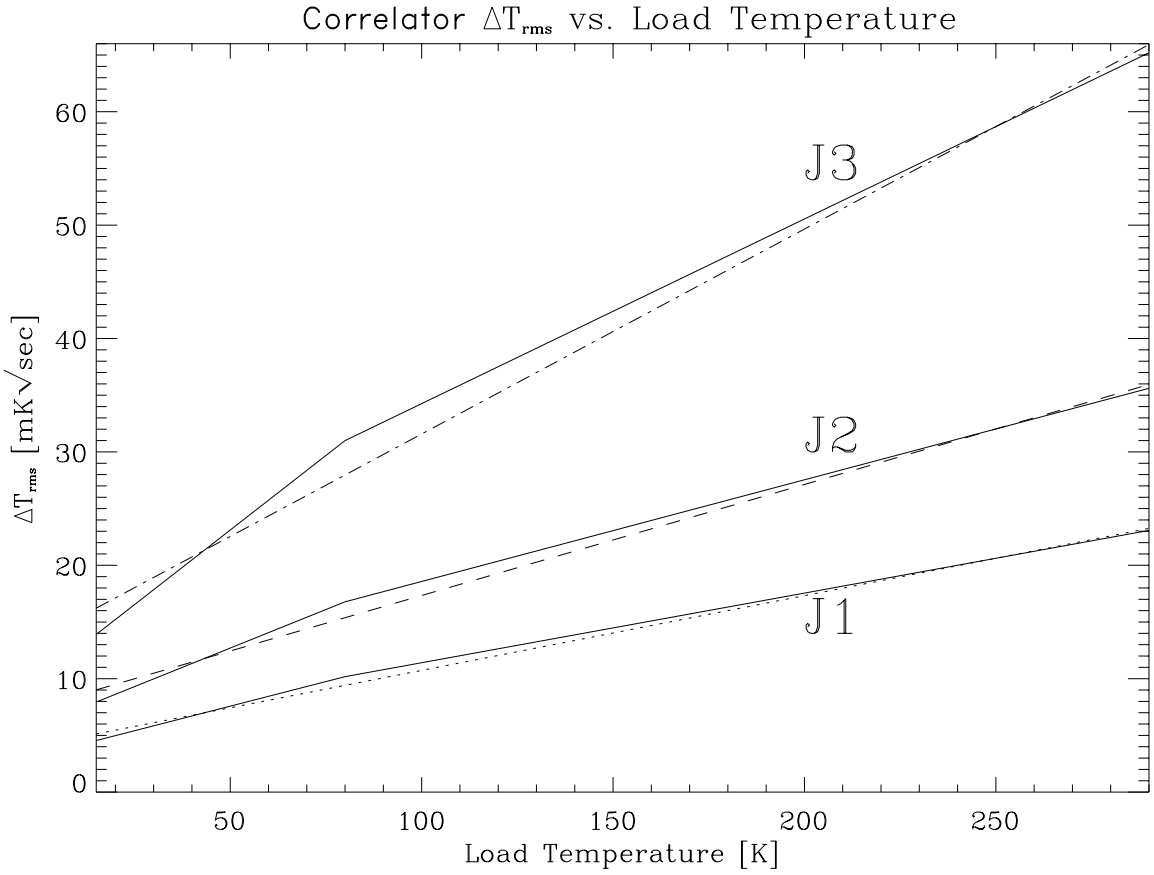

Figure 5.2: Y-factor measurements of all three correlators are shown. The dash-dot, dash, and dotted lines are the best linear fits to the corresponding correlator data. The results obtained from these measurement for J1 and J2 are consistent with the corresponding values obtained using the other two methods discussed in this Chapter (PSD and bandwidth methods). All correlator channels appear to suffer some compression. Correlator J3 displays the greatest compression, and the NET derived from this measurement is not consistent with that obtained from the PSD measurement discussed at the end of this Chapter.

a polarimeter is to employ a wire grid calibrator (WGC) [66], [85], [86]. The WGC is a passive source which can provide electromagnetic fields which are correlated in each arm of the receiver, and is placed outside the cryostat for rapid implementation.

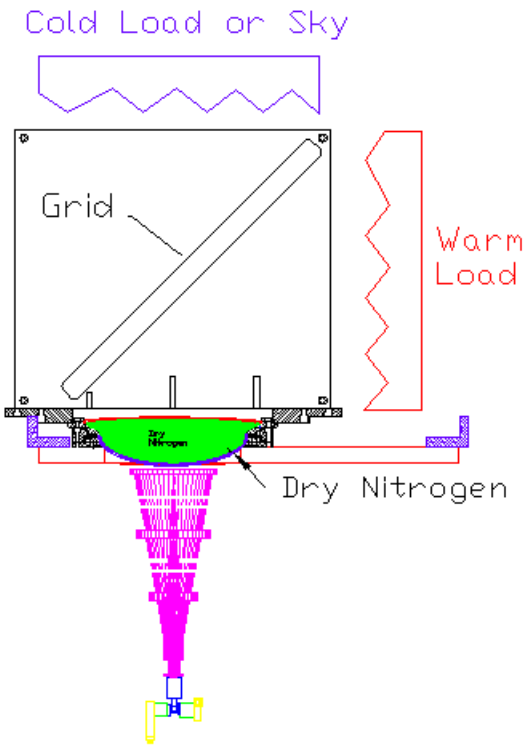

Figure 5.3: Side view of wire grid calibrator (WGC) in place during calibration.

The grid functions by transmitting thermal radiation from a blackbody source in one polarization, and reflecting thermal radiation from a second blackbody source (at a dif-

ferent temperature) into the orthogonal polarization, see figure 5.4. For the POLAR calibrator, the cold load is located above the grid and produces fields E_1 and H_1, and the warm load produces fields E_2 and H_2. The grid's wires reflect fields polarized along their axes and transmit fields orthogonal to their axes. The result is that, ideally, H_1 is transmitted and E_2 is reflected into the feed-horn producing, as we will show, a 100% polarized diffuse source with an antenna temperature equal to the temperature difference between the two loads.

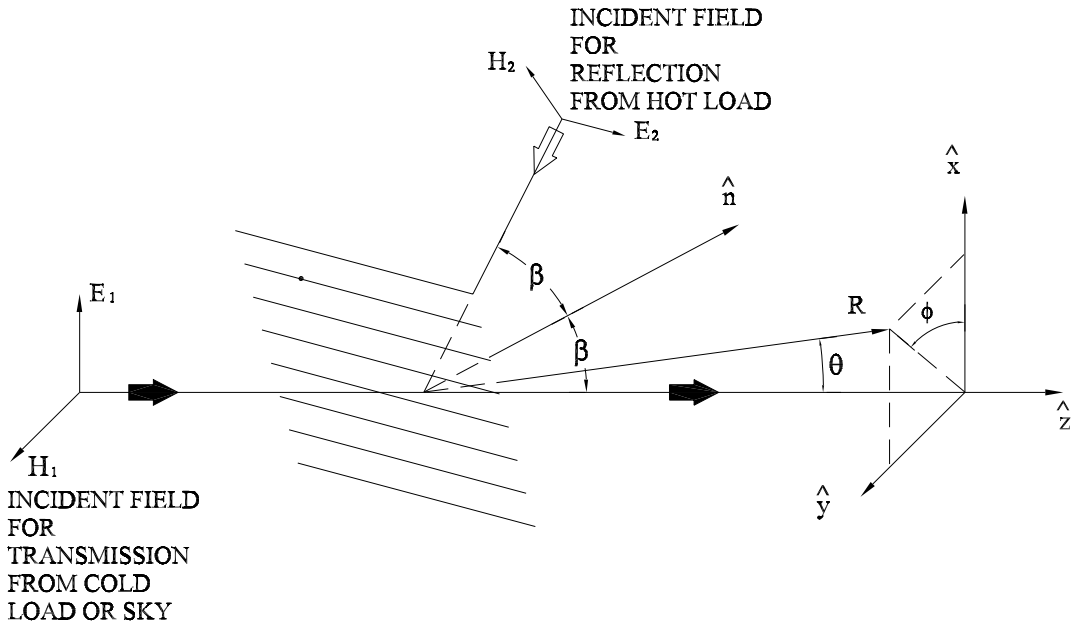

Figure 5.4: Geometry of the Wire Grid Calibrator

Our wire-grid calibrator[1] was fabricated by deposition of copper onto a 50 mil mylar substrate. The wires themselves are 0.008" wide with 0.008" spaces. For support the grid is sandwiched between Dow Corning "pink" Styrofoam sheets (emissivity of $\sim 1\%$), and the sandwich is mounted at 45° to the aperture plane. See figure 5.3 for the orientation of the grid during calibration. The grid has an integrated bearing system which allows it

[1]Designed by Chris O'Dell.

to rotate directly over the vacuum window. This allows us to keep the dewar stationary and simply rotate the grid to calibrate POLAR.

As shown in Chapter 3, the properties of the source function, $\hat{\gamma}(\nu)$, defined in Chapter 4 determine the output voltage recorded by the correlation channels. The function $\hat{\gamma}(\nu)$ depends on the coherence of the electric fields produced by the thermal radiators. However, we only know the *antenna temperature* of the hot and cold loads, *not* the electric fields produced in the x and y directions. Fortunately, as we will see, only the antenna temperatures are needed in the end.

The resulting field seen by the feed-horn is the superposition of the transmitted field H_1, and the reflected field E_2, In terms of the (x', y') basis of the feed-horn and OMT and the (x, y) basis of the rest frame of the WGC, the electric field produced by the WGC as the polarimeter is rotated by an angle α is given by:

$$\begin{aligned} E_{x'} &= E_x(t)\cos\alpha + E_y(t)\sin\alpha \\ E_{y'} &= -E_x(t)\sin\alpha + E_y(t)\cos\alpha. \end{aligned} \tag{5.7}$$

The output of the correlator from the coherence function given by 3.11 is:

$$\begin{aligned} V_{out} &\propto \langle \hat{E}_{x'}(\nu)\hat{E}^*_{y'}(\nu)\rangle \\ &= \langle (E_x(t)\cos\alpha + E_y(t)\sin\alpha)(-E_x(t)\sin\alpha + E_y(t)\sin\alpha)\rangle, \end{aligned} \tag{5.8}$$

with the load fields E_x, E_y given by:

$$E_y(t) = E_{y_o} \cos[\nu t + \phi_y(t)]$$

$$E_x(t) = E_{x_o} \cos[\nu t + \phi_x(t)]. \tag{5.9}$$

We obtain:

$$V_{out} \propto \langle -E_x(t) \cos\alpha E_x(t) \sin\alpha + E_y(t) \sin\alpha E_y(t) \sin\alpha \rangle$$

$$\propto \langle E_y E_y^* - E_x E_x^* \rangle \sin\alpha \cos\alpha$$

$$\propto \sin 2\alpha [\langle E_y E_y^* \rangle - \langle E_x E_x^* \rangle]$$

$$\propto Q \sin 2\alpha$$

$$= \gamma (T_y - T_x) \sin 2\alpha$$

where γ converts antenna temperature (measured by the radiometer) to intensity (the units of the Stokes parameter, Q). Note that at $\alpha = 0^\circ, 90^\circ, 180^\circ, 270^\circ$ the correlators have zero output as the fields are completely aligned along only one port of the OMT and thus do not produce correlated fields between the two arms.

Ideally, the grid would reflect T_{hot} from the side in 100% horizonal polarization and transmit T_{cold} from the top in 100% vertical polarization, resulting in $V_{out} \propto \gamma(\nu)(T_{cold} - T_{hot}) \sin 2\alpha$. In practice, due to loss and reflection, the grid is not perfect and instead we observe the following antenna temperatures at the feed-horn in the two orthogonal polarizations [85]:

Table 5.2: Estimated Properties of Grid and Loads Used For Calibration

Property	Value
$r_{\|\|}$	0.995
r_l	0.02
$t_\perp$	0.95
T_{bg}	290 K
$\Delta T_1 = T_{300K} - T_{sky}$	256 K
$\Delta T_2 = T_{300K} - T_{77K}$	196 K

$$T_{hot'} = r_{||}[(1 - r_l)T_{hot} + r_l T_{bg}] + (1 - r_{||})[(1 - r_l)T_{cold} + r_l T_{bg}] \tag{5.10}$$

$$T_{cold'} = t_\perp[(1 - r_l)T_{cold} + r_l T_{bg}] + (1 - t_\perp)[(1 - r_l)T_{hot} + r_l T_{bg}], \tag{5.11}$$

where: $r_{||}$ is the grid's reflectivity to radiation polarized parallel to the wires, $t_\perp$ is the grid's transmission for radiation polarized perpendicular to the wires, r_l is the reflectivity of the load, and T_{bg} is the effective background temperature of the radiation field surrounding the calibrator. In the above equations, we have neglected the effects of the emissivities and dielectric constants of the mylar and Styrofoam.

We have two pairs of temperature differences with which to calibrate POLAR. Using a 300 K load (in reflection) and the sky (in transmission) we obtain a polarized antenna temperature of 256 K. Using a 300 K load (in reflection) and a 77 K Liquid Nitrogen load (in transmission) we obtain an antenna temperature of 196 K. Here we have assumed the properties of the grid as listed in table 5.2.

A plot of a calibration run is shown in figure 5.5. The sinusoidal oscillations are the result of rotation of the grid over the feedhorn. The first set of oscillations corresponds to the 300 K Load and the sky and the second set corresponds to 300 K Load and the 77 K Liquid Nitrogen Load.

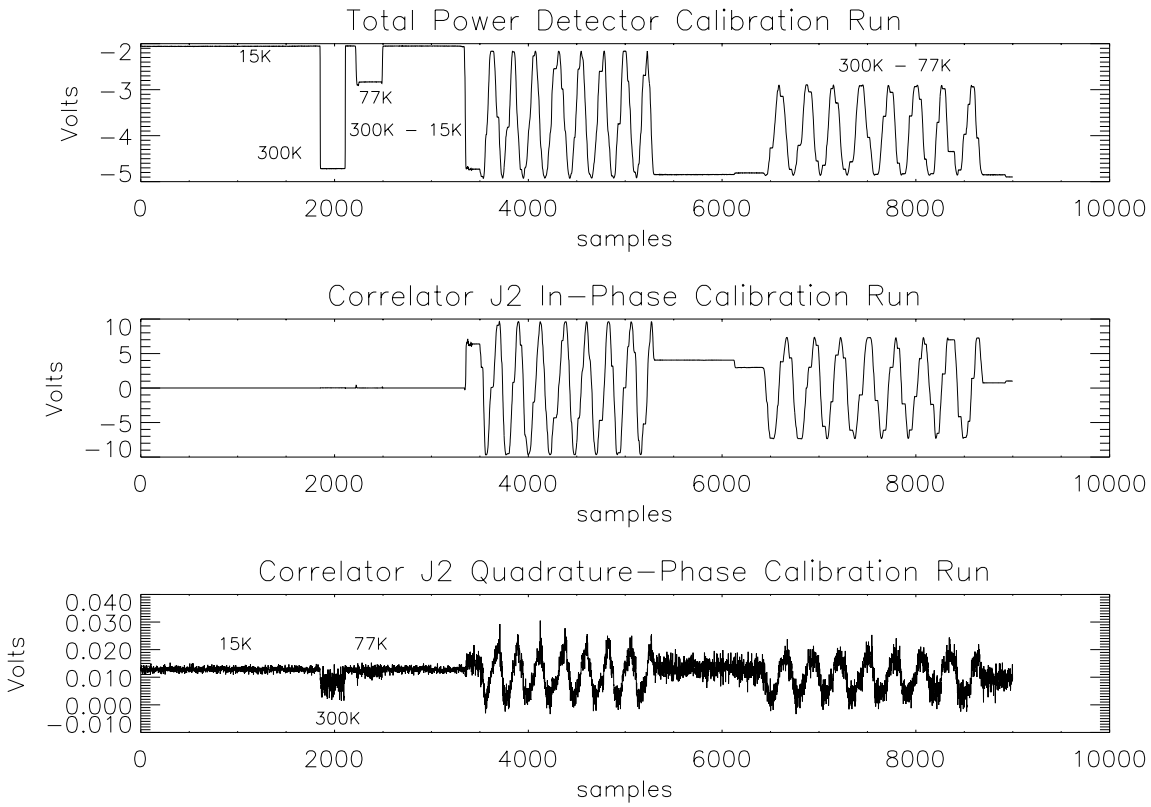

Figure 5.5: Voltages out of correlator J2 and a total power detector during calibration with the Wire Grid Calibrator (WGC). The middle figure shows the voltage out of J2's in-phase lock-in detector, the bottom figure shows the corresponding voltage out of J2's quadrature phase lock-in detector. The various temperature loads are indicated at the time they are applied. The first set of oscillations corresponds to a polarized temperature obtained by using a 300 K load and the sky, which produces 256 K signal. The second set of oscillations corresponds to a polarized temperature obtained by using a 300 K load and a Liquid Nitrogen Load producing a 196 K signal. Note the suppression of the correlated component in the quadrature phase detector, and also note that the noise envelope of that detector is a function of the load temperature making it an effective noise monitor.

5.3.1 Gain Matrices

The grid furnishes us with a well-defined thermal load which is 100% polarized, which is exactly what is needed to calibrate POLAR's voltage output in terms of antenna temperature. Following [85] we model the output of the polarimeter versus rotation angle as a linear combination of the Stokes parameters at the feed horn. The output voltage is modeled as a vector $\bar{v}$:

$$\bar{v} = \begin{pmatrix} v_y \\ v_x \\ v_Q \end{pmatrix} = \begin{pmatrix} g_{yy} & g_{yx} & g_{yQ} \\ g_{xy} & g_{xx} & g_{xQ} \\ g_{Qy} & g_{Qx} & g_{QQ} \end{pmatrix} \begin{pmatrix} T_{Fy} \\ T_{Fx} \\ T_{FQ} \end{pmatrix} + \begin{pmatrix} o_y \\ o_x \\ o_Q \end{pmatrix} + \bar{n} \tag{5.12}$$

or

$$\bar{v} = \hat{\mathbf{g}}\bar{T}_f + \bar{o} + \bar{n} \tag{5.13}$$

where $\hat{\mathbf{g}}$ denotes the gain matrix, $(\bar{T_F})$ is the vector of actual antenna temperatures produced at the feed by the grid, and $\bar{o}$ and $\bar{n}$, respectively, represent offset and noise contributions to $\bar{v}$. Ideally, $\hat{g}$ would have only on-diagonal elements. The off-diagonal elements of $\hat{g}$ correspond to various non-idealities of the instrument which will result in offsets in our measurements. We will elaborate on these terms in the following.

In practice, the grid is placed directly over the feedhorn aperture formed by the vacuum window and rotated while the polarimeter is held fixed. The resulting vector of voltages is recorded and a least-squares fit is made to the data using the model of equation 5.12. The gain matrix parameters, including the off-diagonal cross-talk elements, and the offsets are recovered for each calibration run.

5.3.2 Calibration Using the WGC

With the antenna temperatures of the loads given by equations 5.11, The voltages out of the two total-power channels and the correlator channel are then:

$$\bar{v} = \begin{pmatrix} v_y(\alpha) \\ v_x(\alpha) \\ v_Q(\alpha) \end{pmatrix} = \begin{pmatrix} g_{yy}T_c + g_{yx}T_s + g_{yQ}(T_{hot'} - T_{cold'})\sin 2\alpha + o_y \\ g_{xy}T_c + g_{xx}T_s + g_{xQ}(T_{hot'} - T_{cold'})\sin 2\alpha + o_x \\ g_{yQ}T_c + g_{xQ}T_s + g_{QQ}(T_{hot'} - T_{cold'})\sin 2\alpha + o_Q \end{pmatrix} + \bar{n} \qquad (5.14)$$

where

$$T_c = T_{hot'}\cos^2\alpha + T_{cold'}\sin^2\alpha$$

and

$$T_s = T_{hot'}\sin^2\alpha + T_{cold'}\cos^2\alpha$$

.

To recover $\hat{\mathbf{g}}$, we first integrate long enough that the noise term, $\bar{n}$ is negligible, and then measure the offsets, $\bar{o}$. Then we can invert 5.14 to obtain $\hat{\mathbf{g}}$. Since we have two pairs of temperature differences we can measure the calibration constants as a function of this difference and check for linearity. Our two loads produce effective polarization antenna temperatures of 256 K and 196 K and it is verified that the calibration constants are equal to better than 10% over this range. The linearity of the correlators over this wide range in temperatures, and at such high temperatures, suggests that the radiometer is linear over 6 dB, which is quite impressive for an instrument with $\sim$ 100 dB of RF gain and which uses diode-based multipliers to implement the correlation radiometer technique.

5.3.3 Results of WGC: Gain Matrices and Systematic Effects

We recover three separate gain matrices; one per correlator:

In the following we show the gain matrix G in [K/V]; $G_{ij} = 1/g_{ij}$. The off-diagonal elements are indicated by their relative size compared with the corresponding on-diagonal terms, *i.e.*, for a given correlator $G_{xQ} = fG_{QQ}$, where f is given as a percent. For all three correlators, J1, J2, J3 we obtain:

$$\hat{\mathbf{G}}_{\mathbf{J1}} = \begin{pmatrix} -96.4 & 3.8\% & 6.1\% \\ 8.3\% & 59.3 & -6.7\% \\ 6.1\% & -6.7\% & 55.8 \end{pmatrix} \tag{5.15}$$

$$\hat{\mathbf{G}}_{\mathbf{J2}} = \begin{pmatrix} -96.4 & 3.8\% & 8.6\% \\ 8.3\% & 59.3 & -9.2\% \\ 8.6\% & -9.2\% & 29.3 \end{pmatrix} \tag{5.16}$$

$$\hat{\mathbf{G}}_{\mathbf{J3}} = \begin{pmatrix} -96.4 & 3.8\% & 8.6\% \\ 8.3\% & 59.3 & -9.3\% \\ 8.2\% & -9.3\% & 55.5 \end{pmatrix} \tag{5.17}$$

The entries of the gain matrix $\hat{\mathbf{g}}$ tell us a great deal about the performance of our instrument. The on-diagonal elements of $\hat{\mathbf{G}}$, (G_{xx}, G_{yy}, G_{QQ}) dominate the matrix; they are the terms which measure the system calibration in [K/V].

However, to the experimentalist, the off-diagonal elements are nearly equal in importance for they encode information regarding the system's imbalance, cross-talk, and imperfect isolation between polarization states. All of these effects result in systematic differences between the actual polarization, and that which is measured by POLAR. These effects are known as "offsets", and may be incorrectly interpreted as celestial signals if

they are not removed or are unstable in time.

There are two independent effects responsible for the off-diagonal elements, corresponding to the two different off-diagonal elements $g_{xy} = g_{yx}$ and $g_{xQ} = g_{yQ}$. Let us examine each of these effects in detail. First we will analyze the effects of $g_{xy} \neq 0$, so we set $g_{yQ} = n_y = o_y = 0$. Then the first non-ideality, g_{xy} (or equivalently, g_{yx}), implies that at $\alpha = 0$, when we should only see $T_{hot'}$, we actually observe $v_y = g_{yy}T_{hot'} + g_{yx}T_{cold'}$. So the non-ideality g_{xy} has introduced an offset in the total power outputs. We can now identify the terms which contribute to the total offset in the total power channels. First, we make some preliminary definitions. We define the isolation of the OMT to be the fraction of transmitted *power* into one rectangular (polarization) port which appears at the other (orthogonal) port. The main contribution to the total power offset is from cross-polarization effects in the horn or the OMT [2] These terms contribute to the g_{xy} terms in the gain-matrix equations used for calibration. A similar calculation shows that the contributions to the correlator off-diagonal elements, *e.g.*, g_{xQ}, are primarily attributed to gain differences in the horn's E and H plane power response, as well as gain imbalances in the two HEMT amplifiers.

To address these problems we have constructed a feed horn with a high-level of symmetry between E and H planes, along with a low level of cross-polarization of $\sim -30dB$, see Chapter 4. The OMT also has a high degree of E/H polarization port isolation; measured ($|S^{omt}_{x'y'}|^2 \sim -30dB$). Though its cross-polarization has not been measured, it

[2]Although rarely refereed to as such, cross polarization of the OMT is a well-defined concept; distinct from the more familiar figure-of-merit: isolation. Conceptually, we can consider the actual OMT to be an in-series combination of a feed-horn (with non-vanishing cross-polarization) and an ideal OMT (*i.e.* one with no cross-polarization). Then, the cross-polarization of the actual OMT is that of the series-feed. This definition asserts that no practical measurement of a horn-OMT combination can decompose the cross-polarization into components definitively associated with either sub-component.

is believed that it is less than -30dB. Gain imbalances are minimized by installing fixed coaxial attenuation in the IF band, just prior to correlation, to better than $1dB$.

From 5.15, 5.16 , 5.17 , we see that the off-diagonal elements are uniformly less than 10% of their on-diagonal counterparts. This indicates that there are correlations between the correlators and the total power detectors. This correlation causes the correlators to exhibit all of the undesirable traits of the total power detectors: decreased sensitivity and $1/f$ behavior as demonstrated in section s:psd. These effects are coming in at a low level, however. Further investigation is needed: multiple calibrations over longer periods of time will provide us with estimates of the errors in the gain matrices as well as indicating the long term stability of the calibrations themselves.

5.4 Noise Analyses and Noise Equivalent Temperatures: NETs

Once we know the calibration between voltage and temperature, by measuring the voltage RMS we in turn obtain the temperature RMS. The noise equivalent temperature (NET) of the detector is the instrument noise as measured in a bandwidth of $\sqrt{1Hz}$, which can be converted to the noise in a one-second integration, ΔT_{RMS}, by dividing by $\sqrt{2}$. We have that the noise in an arbitrary integration time, τ, is:

$$\Delta T_{RMS} = NET/\sqrt{\tau}. \tag{5.18}$$

Again, the model of the noise of the total power detectors differs from that of the correlators. From equation 5.3 for the Total Power detectors:

$$NET = \frac{T_{SYS} + T_{load}}{\sqrt{\Delta\nu}}, \tag{5.19}$$

while for the correlators, from equation 5.3, we have that:

$$NET = \sqrt{2}\frac{\sqrt{(T_{TP0} + T_{load})((T_{TP1} + T_{load})}}{\sqrt{\Delta\nu}} \tag{5.20}$$

The most naive technique to obtain the NETs is simply to calculate the RMS of the time stream in a one-second segment and convert from voltage to temperature. This approach, however, only applies when the signal is a wide-sense stationary Gaussian process, as defined in Chapter 1. Of course, the time stream is not pure Gaussian white noise; the spectrum will exhibit an excess of low frequency power (" $1/f$ noise "). In practice, low-frequency components in the time-stream will dominate the RMS if they are not removed. This, of course, is the motivation for the modulation of the signal by rotation of the instrument. A better approach is to compute the power spectrum of the data, and use it to estimate the RMS. To do this we must first measure the transfer function of the pre-amplifiers, $G(\nu)$. This is accomplished by terminating the input to the pre-amplifier and recording its PSD. The equivalent integration time of the pre-amplifier circuit is related to its audio bandwidth by:

$$\tau = \frac{1}{2\Delta\nu_{audio}} = \frac{G_{audio}(0)}{2\int_0^\infty G_{audio}(\nu)d\nu}. \tag{5.21}$$

This τ is the equivalent integration time of the pre-amplifier for each channel to be used in the radiometer equation.

Given a measurement of a channel's PSD, $S(\nu)$ [V^2/Hz], and pre-amplifier transfer function, $G(\nu)$, we can estimate the variance of the time stream as:

$$\sigma^2 = \frac{\int_{-\infty}^\infty S(\nu)G(\nu)d\nu}{\int_0^\infty G(\nu)d\nu}. \tag{5.22}$$

In practice, a given channel's PSD is only "white" (*i.e.* flat) above a certain frequency, ν_{knee}, and so the lower limit in the numerator's integral is replaced by this value. The amplitude of the PSD in the "flat" region provides us with an estimate of the time stream's variance without $1/f$ noise. Making use of the Wiener-Khintchin Theorem from Chapter 4, we can estimate the autocorrelation function (ACF) of the time-stream from the inverse Fourier transform of its PSD, and evaluate it at zero-lag. Of course this estimate is not independent of the PSD estimate since the autocorrelation function, $R(\tau)$, of the time stream, $y(t)$, is given by:

$$R(\tau) = \lim_{T\to\infty} \frac{1}{T} \int_{-T/2}^{T/2} y(t')y(t'+\tau)dt' \tag{5.23}$$

which, when $\tau = 0$, becomes:

$$\frac{1}{T} \int_{-T/2}^{T/2} y^2(t')dt' \equiv \langle y^2(t)\rangle = \frac{\int_{-\infty}^{\infty} S(\nu)G(\nu)d\nu}{\int_0^{\infty} G(\nu)d\nu}. \tag{5.24}$$

Although these two methods are not mathematically independent, it is informative to evaluate both in practice. Each has its own region of applicability, and each can be computed independently and then compared to the Fourier transform estimate given by the other. The ACF at zero-lag of the raw data suffers from contamination due to the low-frequency drifts apparent in the PSD, and it is therefore more convienient to calculate the PSD and then invert it to get the ACF. On the other hand, correlations induced in the time stream by instrumental effects (e.g., the low-pass filter integration stage) are most clearly visible in the ACF.

For both the ACF and PSD estimations of the noise it is impractical to transform large sections of data at a single time. Additionally, this method would result in low-precision

estimates of the desired functions in exchange for high-resolution (in either frequency or temporal bins). Instead, we choose to break the data sets into several smaller sections and subsequently average the transforms. This approach also yields an estimate of the dispersion of the ACF or PSD about its mean value.

Noise After Lock-In Detection

As discussed earlier, after multiplication the signals are detected via a lock-in circuit centered on the Analog Devices 630 Modulator/Demodulator. The AD630 multiplies the signal out of the multipliers by a reference waveform, which in our case is a square-wave generated by a dedicated crystal oscillator. The oscillator generates the phase-switch waveform as well as the in-phase and quadrature reference phases for the AD 630s.

We note that our lock-in detection after multiplication is essentially an implementation of the Dicke radiometer, switched at audio frequencies $\nu_{switch} = 1$ KHz. Following multiplication, the product of the multiplier output and the reference waveform is integrated for an amount of time $\frac{1}{2\Delta\nu_{anti-aliasing}}$. Our signal after the lock-in is effectively the difference between the multiplier signal at times separated by, roughly, the period of the phase switch, $T_{switch} \simeq 1$ msec. The multiplier output at times t_i and t_j, is uncorrelated if $|t_i - t_j| > 1/\Delta\nu_{IF} \sim 0.1$ nsec. So, since $T_{switch} \gg 0.1$ nsec the PSD of the lock-in detectors will be PSD of the noise waveform produced by our detectors when viewing an unpolarized source will be 2 times larger than the corresponding value without the lock-in detectors. The signal-to-noise ratio will thus be reduced by a factor of $\sqrt{2}$, which is in addition to the factor of $\sqrt{2}$ already included in the radiometer equation for the correlation radiometer. Relative to an ideal total power radiometer with an NET of σ [mK Hz$^{-\frac{1}{2}}$], our correlator channels have post-detection NET's of 2σ. For comparison with predictions, as in table

5.3, we always quote noise estimates *after* lock-in detection.

We note that the behavior of the noise should be independent of the phase of the reference waveform supplied to the lock-in. To illustrate this we consider figure 5.7 where the in-phase and quadrature phase low-frequency power spectra of correlator J1 are shown. We have developed a phase-switch driver circuit which also produces the in-phase and quadrature phase reference waveforms. For added flexibility we are able to change the phase of the reference waveforms with respect to the physical chop waveform by discrete steps of 0.18°. The quadrature phase detectors provide us with extremely powerful monitors of the noise of the correlator channels.

5.5 Results of Noise Analyses

We begin by referring the reader to figure 5.6 which shows the power spectra of all three in-phase correlator channels and both total power detectors. It is clear from the spectra that the correlators are far more sensitive than the total power detectors. The dramatic $1/f$ rise in the total power detectors is absent in the correlator channels, and allows us to slowly modulate the instrument output by rotation of the radiometer at 30 mHz, rather than at several Hz.

Next, we examine the behavior of the correlator power spectra at low frequencies. In figure 5.7 we display the power spectra at frequencies comparable to the rotation frequency of the instrument. Both the in-phase and quadrature-phase components of the lock-in detectors are shown, and the agreement at frequencies greater than the rotation frequency allows us to use these channels as noise monitors. The presence of signals at the rotation frequency and its harmonics is evident in the in-phase detectors, suggesting that there are

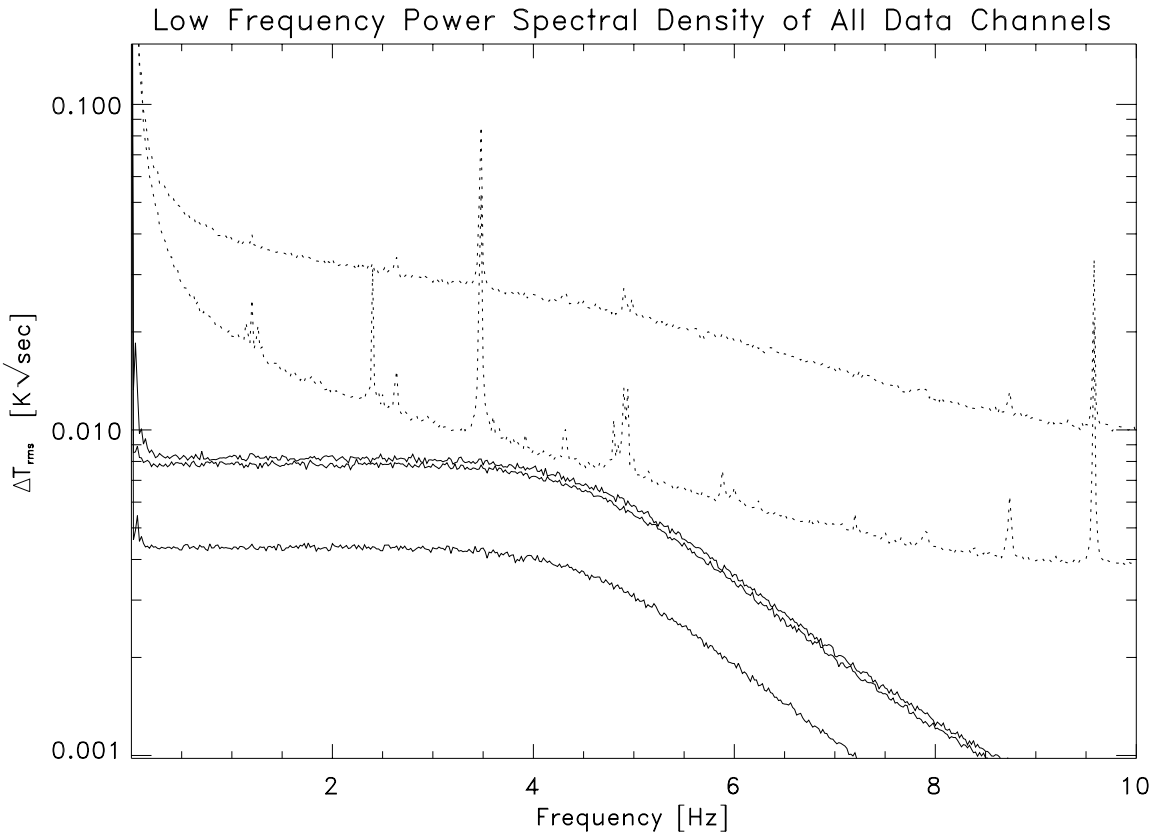

Figure 5.6: The power spectra of all five POLAR data channels while viewing the sky (T_{Ant} = 15K) are shown. The correlator spectra are plotted as solid lines and the total power are dotted. Several features are evident from these plots. The $1/f$ behavior of the total power detectors, and the low-pass filtering of the anti-aliasing filters on all channels above 5 Hz are evident. The CTI coldhead expansion/compression cycle is at 1.2 Hz, and this feature and its harmonics are clearly visible in the total power channels. From high-noise (top) to low-noise (bottom) the channels are TP0, TP1, J3, J2, J1.

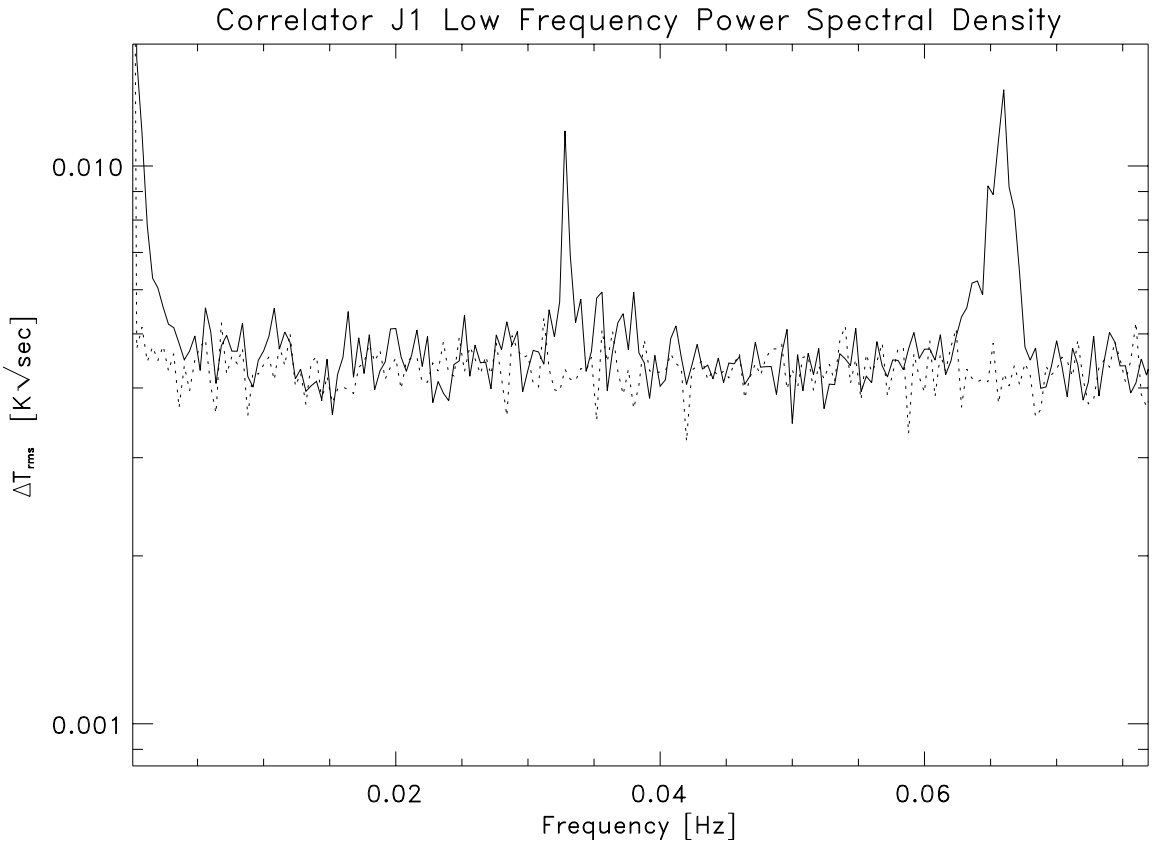

Figure 5.7: The low-frequency power spectra of the lowest noise correlator (J1), in-phase (solid) and quadrature-phase lock-in detectors (dashed), while viewing the sky ($T_{Ant} = 15$K). The quadrature phase detectors behave as effective noise monitors. The rotation frequency is 0.03 Hz, and some synchronous signal modulation is evident in the in-phase detector at this frequency and its harmonics. Absent in the quadrature-phase channels is the $1/f$ noise rise at frequencies below 0.005 Hz.

correlated signals in the raw time-streams which are being modulated by the rotation of the instrument. The stability of these offsets over a single rotation of the instrument is crucial to the recovery of the Stokes parameters.

Overall, the performance of POLAR is quite satisfactory. Table 5.3 compares the measured NET values and with predictions based upon that correlator's system noise and bandwidth. The longer-term performance of POLAR is further elaborated upon in Chapter 10.

From table 5.3 several phenomena are observed. First we see that the noise estimates

Table 5.3: NET Estimates from PSD and RMS Compared With Predicted NET

Channel	NET from PSD [mK$\sqrt{sec}$]	NET from RMS [mK$\sqrt{sec}$]	Predicted from T_N & $\Delta\nu$ [mK$\sqrt{sec}$]
J1	3.6	4.4	2.3
J2	6.5	7.5	2.9
J3	7.1	13.5	4.3

based on the RMS are systematically higher than those obtained from the PSD estimates. This is to be expected: the RMS suffers more-severely from $1/f$ contamination, which is difficult to remove from the time-stream directly. The PSD estimates are taken as the most accurate estimates of the NET because the $1/f$ behavior can be easily distinguished and subtracted.

Next we see that the correlators differ substantially from one-another. This is primarily attributed to the phase optimization discussed earlier. The variable phase-shifter, shown in figure 4.1, has been optimized for channel J1, which has the effect of increasing it's calibration in [V/K] relative to the other two correlators. At present it is not possible to individually tune the phase of each frequency band prior to correlation. This feature will be implemented prior to POLAR's observing run this winter. We expect to then obtain the same sensitivity for all three correlators allowing us to obtain a co-added sensitivity for all correlators of $\simeq 3\text{mK}\sqrt{sec}/\sqrt{3} \simeq 1.7\text{mK}\sqrt{sec}$.

Chapter 6

Systematic Effects

Because the anticipated polarization signal is a factor of $\sim$ 10 times smaller than the temperature anisotropy currently being detected, a thorough understanding of systematic errors is crucial. Polarization experiments have several advantages, however, that promise to make this effort possible. First, as shown in Chapter 7, the atmosphere is known to be polarized only at a very low level, far below the expected level of CMB polarization. Additionally, POLAR measures the polarization of each pixel in a manner which is (nearly) independent of neighboring pixels. It does not require comparison of pixels through different airmasses, and at different times. In anisotropy observations, beam switching often adds noise and additional chop-dependent signals. Potentially, atmospheric effects will have a smaller contribution to this type of experiment than to ground-based CMB anisotropy experiments and will allow longer observation times than have been possible in the past. Long-term observations are key to understanding and removing systematic effects [87]; [88]. Many spurious instrumental effects have been isolated from astrophysical effects by long-term integration tests with the horn antenna replaced by a cold termination.

The most troubling aspect of these effects is that they may not be stable in time. For

the correlator channels, the most pernicious contribution arises from gain fluctuations in the HEMT amplifiers and in the conversion efficiency and phase stability of the heterodyne stage. The conversion efficiency of the mixers is dependent on the Gunn Oscilator power which fluctuates just like an amplifier, thus introducing gain fluctuation, which can be misinterpreted as signals if some component of the variation is commensurate with the modulation frequency of the instrument. The phase stability of the oscilator is equally troublesome [60], since phase fluctuations between the two arms of the radiometer reduce its effective bandwidth. There are several standard methods to improve the stability of the heterodyne stage of the receiver, including phase modulation at frequencies of ~ 1 KHz, and phase-locked loops to stabilize the LO. The latter is quite common in conventional radiotelescopes, though it is not incorporated in the POLAR $K_{\rm a}$ band system. The former technique is performed, however, as described in Chapter 4.

In Table 6 we list some important systematic effects encountered in previous polarization measurements and summarize the solution adopted by POLAR.

Table 6.1: Expected Systematic Effects

Effect	Origin	Control Method
Mechanical Strain	Instrument Rotation	Zenith Scan
Magnetic Coupling	Rotation in $\vec{\mathbf{B}}_{earth}$	Minimal Ferrite Components (Isolators Only)
Microphonics	Mechanical Vibration	Isolation
EMI and RFI	Local Sources	Shield/Filter
Thermal Variations	Diurnal/Environment	Temp Control
Sidelobe Pickup	Sun/Moon/Earth	Low Sidelobe Antenna and Ground Screens

Gravitational effects

A problem with any radiometer that must move in the earth's gravitational field is position-dependent stress and strain on waveguide joints, etc. In the experiments of Lubin and Smoot, for example, observations off-zenith produced polarized offsets which were 1 to 10

times larger than the resulting upper-limit. POLAR attempts to minimize these problems by staring at the zenith, so that to first order no gravitational torques on waveguide components are present. The rotation speed is slow, ~ 2 rpm, and constant so accelerations on stopping and starting rotation are non-existent.

Magnetic Field effects

A particular concern is the coupling of the Earth's magnetic field to the radiometer. The *COBE* DMR had ferrite Dicke switches which produced a spurious signal at the $\simeq$0.1 mK level (Kogut et al. 1996b). POLAR's only ferrite components are its isolaters. However, other components such as amplifiers, etc., may have a low-level magnetic field dependence. Modulation of these effects can be minimized by maintaining a constant orientation of rotation axis with respect to the Earth's field. The magnitude of this effect has been estimated by generating a $\sim$ 10 Gauss DC field, and was undetectable for a one hour integration. Future AC field tests are planned.

Microphonics

The effects of vibrations that occur during rotation are reduced by use of HEMTS rather than high impedance devices such as bolometers, and by the fact that we take data only while the instrument is rotating at a constant rate, using a smooth-driving AC motor. We utilize numerous vibration isolation techniques, as described in Chapter 4, to decouple the primary source of mechanical vibrations: the cryocooler. Waveguide junctions can be a particular concern as vibration at the interface between waveguide flanges can cause modulation of the junction impedance, which will be present in the RF signals. To minimize this effect we have minimized the number of joints by constructing custom manufactured

waveguide sections, and stiffened all waveguides and support structures.

EMI and RFI

These effects can be controlled by Faraday shielding the instrument and by filtering electrical lines into and out of the dewar. Additionally, we employ two-stages of power regulation to all components, both inside the dewar as well as in the warm-IF section. RF sources that occur in the radiometer RF band or IF band are becoming increasingly troublesome. Of particular concern in the future will be communications satellites operating in the bands of interest. No RFI from terestrial sources (such as airport RADAR) has been detected in the data, attributable primarily to the relative isolation of the Pine Bluff Observatory. Given the small sky coverage and low point-source sensitivity of the POLAR 7° experiment, it is unlikely that there is contamination by any known satellite communication system.

Temperature Dependent Effects

Temperature variations in the radiometer can be mitigated by active temperature control and by shielding the instrument from the Sun. The latter function is naturally performed by the ground shields so that the antenna and receiver are completely shielded. The former fuction is provided by a two-stage temperature control system. The first, coarse level of control is provided by a 300 Watt PID controled heating element on the main electronics box. A finer level of control is provided by a second PID controled, thermo-electric cooler (Peltier Cycle) which provides 10 Watts of heating/cooling power.

Sidelobe Pickup and Spillover

The polarimeter must be able to reject or discriminate against emission from the Sun, Moon, and Earth, which appear only in the sidelobes of the beam. None of these sources are expected to be significantly polarized, but asymmetry in the antenna response to the two linear polarizations will create spurious signals. This effect is responsible for the false-detection claimed by Nanos[13], who later attributed his detection to pick-up from a elevator tower in close proximity to his observing site. POLAR requires that the total power from these sources lie below 1 μK, necessitating 75 and 63 dB sidelobe rejection for the Sun and Moon, respectively. Assuming 30 dB rejection from the ground screen, this level of rejection can be achieved with the corrugated horn antenna if data are rejected when these sources lie closer to the zenith than 50° and 30° respectively. Binning of the data in Sun-centered or Moon-centered coordinates will allow us to uncover correlations between the position of these objects and the response of the polarimeter. Spillover from the ground and surrounding structures is minimized by incoporating two-levels of ground screening. The first ground screen rotates with the polarimeter and provides $\sim$ 30 dB of suppression. This ground screen is covered with eccosorb foam sheets which absorb atmospheric radiation, rather than polarizing it via reflection off of a metal surface. The outer ground screen is fixed with respect to the polarimeter and provides an additional 30 dB suppression. This screen reflects the sidelobe response which diffracts over the first screen, to the 10K sky rather than the 300K ground. The combination of two levels of ground screening, along with the corrugated feedhorn's intrinsically low sidelobe level, reduces the contribution from off-axis radiation by $\sim$ 100 dB.

Chapter 7

Large Angular Scale Foregrounds in the $K_{\rm a}$ band

A fundamental question for any attempt to measure the polarization of the CMB is whether the cosmological signal can be distinguished from polarized foreground sources. While astrophysical (non-cosmological) sources of polarized radiation are of interest for other fields, the measurement of CMB polarization is our main objective, so these sources are spurious effects. These foreground sources all have spectra that are distinct from that of the CMB, and in principle can be distinguished from it by multi-frequency measurements. This technique has been employed for observations of CMB anisotropy [89]. However, polarized foreground spectra have not been studied as extensively. To estimate the intensity and spectra of these foreground sources, we rely on theoretical predictions and extrapolations from measurements at different frequencies of the antenna temperatures of these foregrounds. Here we summarize the properties of atmospheric and astrophysical (though non-cosmological) foreground sources.

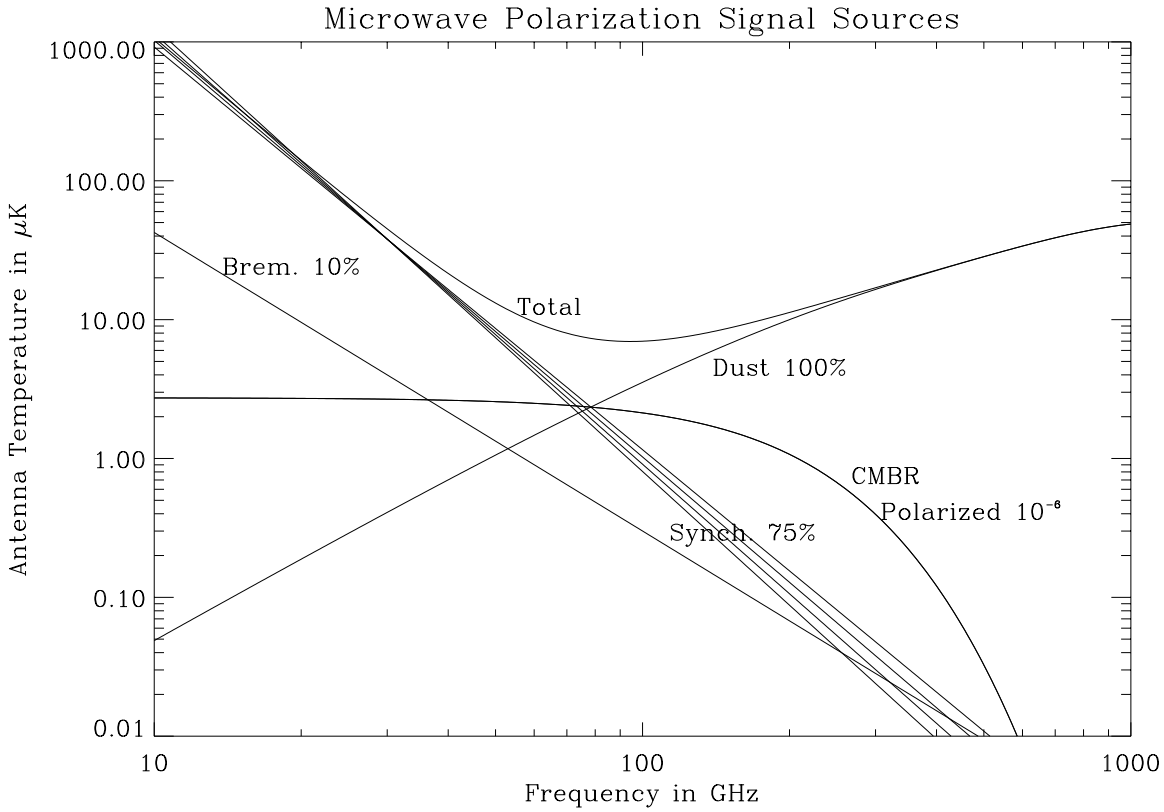

Figure 7.1: Polarized Foreground Spectra at Millimeter Wavelengths. Spectra of expected polarized radiation sources at high galactic latitudes, are shown for a 7° beam. A 3 μK polarized CMB signal is shown, corresponding to 10% of the 10^{-5} CMB anisotropy. At frequencies lower than 90 GHz the polarization signal is dominated by galactic synchrotron emission (up to 75% polarized, as shown). Galactic bremsstrahlung radiation is not polarized in direct emission, but can be up to 10% polarized (as shown) after Thomson scattering. Galactic dust is shown conservatively with 100% polarization.

7.1 Synchrotron Emission

Diffuse galactic synchrotron radiation arises from ionized regions of our galaxy that posses magnetic fields. Consider the relativistic motion of a charged particle of charge q and mass m. We have that:

$$\frac{d}{dt}(\gamma m v) = \frac{q}{c}\mathbf{v} \times \mathbf{B} \tag{7.1}$$

$$\frac{d}{dt}(\gamma m c^2) = q\mathbf{v} \cdot \mathbf{E} = \mathbf{0}. \tag{7.2}$$

The second equation implies that $\gamma =$ constant, so we have: $m\gamma \frac{dv}{dt} = \frac{q}{c}\mathbf{v} \times \mathbf{B}$. Expanding this equation into terms parallel and perpendicular to the magnetic field, we find that $v_{||} =$constant, and $m\gamma \frac{dv_\perp}{dt} = \frac{q}{c}\mathbf{v}_\perp \times \mathbf{B}$ which the equation of uniform circular motion with frequency $\omega B = \frac{qB}{\gamma mc}$. Since the angular acceleration is $a_\perp = \omega_B v_\perp$, we find that the total radiated power is:

$$P = \frac{2q^4 B^2}{3c^5 m^2}\gamma^2 v_\perp^2.$$

For an isotropic distribution of pitch angles α, we find $P = \frac{4}{3}\sigma_T \frac{v^2}{c}\gamma^2 U_B$, where σ_T is the Thomson cross-section and U_B is the energy density of the magnetic field: $U_B = B^2/8\pi$.

Following [90], we can obtain a qualitative description of the spectrum of synchrotron radiation. The individual electrons will produce a brief pulse of radiation once per revolution. These pulses have a broad spectrum, whose square is proportional to the power spectrum of the radiation. If we assume that the charges have an *energy* spectrum of: $N(E)dE = C(\alpha)E^{-p}dE$, where the particle distribution index, p, is related to the spectral

index, s, by: $s = \frac{p-1}{2}$, we obtain the following spectrum:

$$P(\omega) = \frac{\sqrt{3}q^3 CB\sin\alpha}{2\pi mc^2(p+1)}\Gamma\Big(\frac{p}{4}+\frac{19}{12}\Big)\Gamma\Big(\frac{p}{4}-\frac{1}{12}\Big)\Big(\frac{mc\omega}{3qB\sin\alpha}\Big)^{-(p-1)/2}$$

and polarization:

$$\Pi = \frac{p+1}{p+\frac{7}{3}}.$$

The antenna temperature of synchrotron emission obeys a power law:

$$T_{\text{synchrotron}}(\nu) \propto \nu^{\beta},$$

where β is referred to as the *synchrotron spectral index*. The polarization level Π of synchrotron radiation is related to the spectral index [91]:

$$\Pi = \frac{3\beta+3}{3\beta+1}.$$

Faraday rotation and non-uniform magnetic fields will reduce the level of polarization given by this equation. The radiation is linearly polarized between approximately 10% and 75%, depending on galactic coordinates. Below 80 GHz the polarized synchrotron emission dominates all sources, including the CMB if it is polarized at the 1×10^{-6} level, as shown in Figure 7.1. In figure 7.2 we estimate synchrotron emission by extrapolating the Brouw & Spoelstra [92] measurement at 1411 MHz to millimeter wavelengths with the modified power-law spectrum used to fit the *COBE* DMR data [93]. For our modeling purposes we choose $\beta = -2.9$ ([94], [93]), and Π= 75% [92].

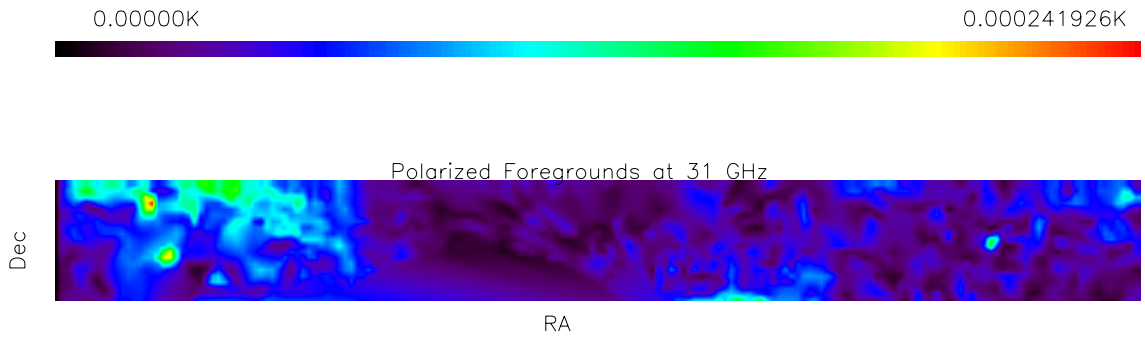

Figure 7.2: Polarized Synchrotron Emission at 1411 MHz ([92]) extrapolated to 31 GHz using a power law spectrum. From right to left the range of RA is $0h \leq RA < 24h$, and from top to bottom the range of Declination is $20° \leq \delta < 60°$. POLAR's observing strip appears in the middle of the figure.

7.2 Polarization Produced by Interstellar Dust

There are two mechanisms by which interstellar dust may produce a polarized signal. The more familiar thermal, vibrational, emission is treated first. Afterwards, we summarize recent developments in the modeling of polarization produced by rotating dust grains.

Extinction of unpolarized radiation from dielectric cylinders will produce polarization because the cylinder's scattering efficiency (or extinction cross-section) is different along the E and H planes of the radiation. The reason for this rests in the anisotropic nature of the grain's electric and magnetic moments. For cylinders with radii much smaller than the wavelength of the scattering (as in the case of simple dipole antenna), currents will flow along the cylinder axis. Depending on the real and imaginary components of the grain's complex index of refraction, m.

Following Spitzer [95], we define $x = \frac{2\pi a}{\lambda}$, where a is the cylinder radius. We find that the polarizing effectiveness of an infinite cylinder with a refractive index of $m = 1.33$[1], $r = 2\frac{Q_E - Q_H}{Q_E + Q_H}$, varies from $r \simeq 1$ (*i.e.*, 100% polarization) at $x = 1$, to $r \simeq 0.4$ at $x = 5$.

[1]For example, for ice $m = 1.33$

7.2.1 Thermal Dust Emission

The polarization level of interstellar dust is not well known. Depending on the shape and the alignment of dust particles, emission from dust particles may be highly polarized with the polarization $I \sim 0.07$, usually aligned parallel to the galactic plane [95].

At low galactic latitudes thermal emission from dust particles dominates the near infrared spectrum. Using the dust spectrum measured by the *COBE* FIRAS [96] normalized to the IRAS 100 micron map, we find that high galactic latitude dust emission is negligible below 80 GHz, even when assumed to be 100% polarized. We use the two temperature dust model [96] :

$$T_{dust} \propto \frac{c^2}{2\nu^2 k} \left(\frac{\nu}{900\text{GHz}}\right)^2 \left[B_\nu(20.4\text{K}) + 6.7 B_\nu(4.77\text{K})\right]. \tag{7.3}$$

At high galactic latitudes $T_{dust} \sim 10\mu$K at 200 GHz ([94], [93]).

7.2.2 Diffuse Emission from Rotating Interstellar Dust Grains

Recently there has been an effort to explain the "anomalous" correlation between infrared dust emission at 100μm and measurements made at 30 - 50 GHz. The emission does not appear to be consistent with Hα emission [97](to be discussed in the following section). Instead, an explanation in terms of spinning interstellar dust has been proposed by Draine and Lazarian [98]. The emission arises from dust grains composed of 100-1000 particles which are "spun-up" by incident starlight due to their non-vanishing electric dipole moments. The precise spectrum of emitted radiation depends sensitively on the models used for the components of the Interstellar Medium (ISM) and for the grains themselves. Generically, however, the rotational emission is expected to dominate that from thermal

dust emission below 70 GHz [98].

The main question for the POLAR experiment is that the emission may be polarized. The dust grains are also expected to have a non-vanishing magnetic dipole moment, which will tend to align with the magnetic field in the ISM. Lazarian and Draine [99] find that the polarization produced by such grains is expected to be in the range 0.1-10%. This deleterious effect is expected to be reduced slightly, however, as the alignment of the magnetic field is uncorrelated over large regions of the ISM. We have not considered this foreground in any of our analyses, though in the future we may investigate its effect on our data set. As usual, each foreground contaminant necessitates a wider spectral coverage in order to subtract.

7.3 Bremsstrahlung Emission

Continuum emission from electrons encountering protons which does not result in recombination is known as free-free emission. The radiation produced is the familiar bremsstrahlung emission found wherever there are copious quantities of free electrons and protons. One type of ionized region are the HII regions, usually identified in optical wavelengths by H_α light. HII regions are often associated "Stromgren Spheres" – spheres of ionized plasma surrounding energetic stars.

Bremmstrahlung scattering of unpolarized radiation does not produce polarized radiation [90]. However, bremsstrahlung emission will be polarized via Thomson scattering by the electrons in the H II region itself. The rescattered radiation will be polarized tangentially to the edges of the cloud, at a maximum level of approximately 10% for an optically thick cloud.

As a toy model, we will consider an incident plane wave emitted from the cloud center to a small scattering region at the radius of the cloud. From Chapter 2 we expect that the polarization will be generated by the plane wave, so all we need to know to estimate the polarization produced by this scattering is the emission of the thermal bremsstrahlung. Following Spitzer [95], we estimate the free-free emission factor for electron-proton scattering as :

$$j_\nu = 5.44 \times 10^{-39} \frac{g_{ff} n_e n_i}{T^{\frac{1}{2}}} e^{-h\nu/k_b T} \text{erg cm}^{-3}\text{s}^{-1}\text{sr}^{-1}\text{Hz}^{-1}, \tag{7.4}$$

where n_i is the proton density, n_e is the electron density, and g_{ff} is the Gaunt factor, which is a slowly varying function of frequency, which in the radio region is well-modeled by:

$$g_{ff} = 9.77(1 + 0.130 \log \frac{T^{3/2}}{\nu}). \tag{7.5}$$

To obtain the total radiated energy, ϵ, we integrate equation 7.4 over $4\pi d\nu$ and obtain:

$$\epsilon = 1.4 \times 10^{-27} n_e n_i T^{\frac{1}{2}} \langle g_f f \rangle \text{ergcm}^{-3}\text{s}^{-1}\text{sr}^{-1}\text{Hz}^{-1}, \tag{7.6}$$

where the mean Gaunt factor, $\langle g_{ff} \rangle$, has a weak dependence on temperature, varying between 1.1 and 1.4 over reasonable HII temperature ranges.

We now need the radius of the Stromgren Sphere surrounding the star (which produces the free-electrons). This radius is a function of the star's spectral type. From Spitzer we have table 7.3.

Due to the rotational symmetry about the line of sight of the spheres we are considering

Table 7.1: Properties of HII Regions

Spectral Type	$T_{eff}[^{\circ}K]$	R/R_{sun}
O5	47,000	13.8
O9	34,500	7.9
B0	22,600	6.2

we expect that the intrinsic polarization produced by these clouds will be zero. However scattering of the CMB quadrupole (which is estimated to be that measured by the COBE DMR) by the free-electrons in the HII region will produce polarization with a magnitude of

$$Q \sim \frac{3\sigma_T}{8\pi}\sqrt{\frac{\pi}{5}}Q_{RMS} \sim 1 - 10\mu K \tag{7.7}$$

The polarization produced by this type of scattering will peak at angular scales comparable to the angle subtended by the HII regions, and thus for POLAR's 7° beam they are negligible. The locations and emissivities of galactic H II regions are not well known, but Bennett et al. [93] model the bremsstrahlung emission in the galaxy by subtracting a synchrotron model from microwave sky maps. In any case the polarization in the rescattered bremsstrahlung emission will be at least an order of magnitude smaller than the polarized synchrotron signal at frequencies greater than 10 GHz. We quote the result of Bennett et al. [93] that

$$T_{bremsstrahlung} \propto \nu^{-2.15}, \tag{7.8}$$

with total intensity $\sim 40\mu$K at 30 GHz ([94], [93]).

Dust grains are known to be present in HII regions. Since we know from the previous section that interstellar dust polarizes starlight, we also expect that the dust associated with HII regions may produce polarization in addition the polarization we have considered

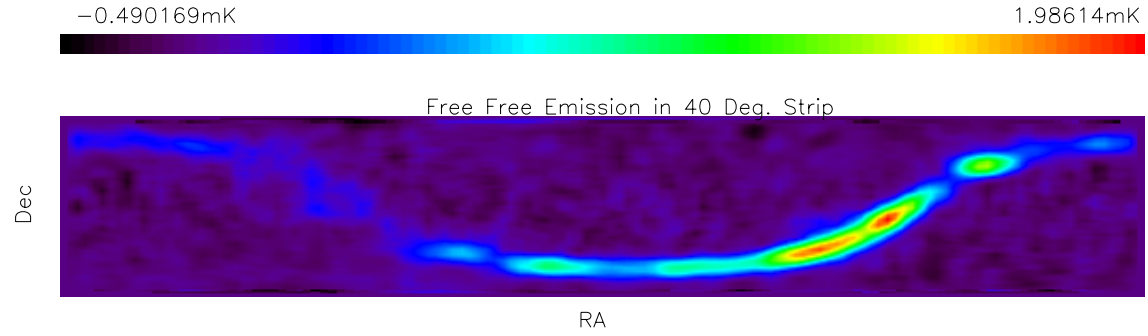

Figure 7.3: COBE Estimated Free-Free Antenna Temperature Map Centered on Declination $\delta = 43°$. From right to left the range of RA is $0h \leq RA < 24h$, and from top to bottom the range of Declination is $20° \leq \delta < 60°$. POLAR's observing strip appears in the middle of the figure.

by Thomson scattering. We have not estimated this effect, however.

7.4 Extragalactic Point Sources

The dominant radiation mechanism for extragalactic radio sources is synchrotron emission [100]. These sources have a net polarization of $< 20\%$. Calculations made by Franceschini et al. [101] of the temperature fluctuations in measurements of anisotropy of the CMB arising from unresolved, randomly distributed sources show that they contribute negligibly at 30 GHz to a 7° anisotropy experiment. If the orientations of the polarization vectors of these sources are uncorrelated over 7° regions, we would also expect a negligible contribution to the signal observed POLAR.

7.5 Atmospheric Contamination

Although strictly not a foreground, emission from the atmosphere provides an equally formidable obstacle to the detection of polarization of the CMB. The antenna temperature of the earth's atmosphere between 10 and 60 GHz is dominated by an emission feature at ~ 22 GHz caused by atmospheric water vapor, and a series of emission lines at ~ 60

GHz due to molecular oxygen. We now investigate whether or not this emission is linearly polarized.

7.5.1 Polarized Emission from the Earth's Atmosphere in the $K_{\rm a}$ Band

In the absence of external fields, neither of these atmospheric components is known to emit polarized radiation in the frequency range of interest. However, Zeeman splitting of the energy levels of atmospheric molecules by the magnetic field of the earth can produce polarized emission. The valence band of water is completely full, and thus, does not exhibit Zeeman splitting. However, the O_2 molecule has a non-zero magnetic moment due to its two unpaired valence electrons which interact with the Earth's magnetic field. We here discuss polarized emission from mesospheric oxygen, and show that it is negligible in comparison with the expected polarized intensity of the CMB.

The Zeeman effect breaks the energy degeneracy of the two unpaired valence electrons of molecular oxygen. The total angular momentum quantum number of the oxygen molecule is $j = 1$, which implies that the oxygen molecule's rotational spectral lines are Zeeman split into $2j + 1 = 3$ distinct lines. Dipole radiation selection rules for transitions between these levels permit transitions as long as the change in magnetic quantum number, m, is: $\Delta m = 0, \pm 1$. Transitions with $\Delta m = +1$, for example, correspond to the absorption of a right circularly polarized photon or the emission of a left circularly polarized photon. The absorption and emission properties depend, therefore, on both the frequency and polarization of the radiation. The frequency of each Zeeman split level is [102], [103]:

$$\nu_Z = \nu_0 + 2.803 \times 10^{-3} B\eta(\Delta m)[\text{GHz}] \tag{7.9}$$

where ν_0 is the unperturbed frequency, η is a shift factor with $|\eta| \leq 1$, and B is the magnitude of the earth's magnetic field, typically 0.5 Gauss throughout the mesosphere. The largest possible frequency shifts occur for $\eta = \pm 1$, which imply that the center frequencies for the polarized emission components will be confined to within 1.4 MHz of the unsplit center frequency. In principle, emission at these split frequencies could be up to 100% circularly polarized. Away from the center frequencies, the total intensity of emitted radiation decays with frequency as: $I \sim \frac{1}{(\nu-\nu_0)^2}$ [104]. For a small shift in frequency, $\Delta\nu_0$, away from the center frequency, the first order fractional change in emissivity can be shown to be:

$$\frac{\Delta I}{I} = \frac{2\Delta\nu_0}{\nu - \nu_0}. \tag{7.10}$$

For a single Zeeman split component,

$$\frac{\Delta I}{I} = \frac{2\Delta\nu_{Z,\Delta m}}{\nu - \nu_Z},$$

where $\Delta\nu_{Z,\Delta m} = \nu_Z - \nu_0 = 2.803 \times 10^{-3} B\eta(\Delta m)$[GHz], from equation 7.9. To obtain the total contribution to the emission of both polarization components we must sum over left-handed and right-handed contributions:

$$\frac{\Delta I_{\text{tot}}}{I} = \sum_{\Delta m = \pm 1} \frac{2\Delta\nu_{Z,\Delta m}}{\nu - \nu_Z} \tag{7.11}$$

However, we have for the shift factor in equation 7.9: $\eta(\Delta m = +1) = -\eta(\Delta m = -1)$ so the net effect on the emissivity is exactly canceled out by the two circularly polarized components [104]. Any second order contributions to the emission scale as

$$\sim \frac{1}{(\nu - \nu_Z)^2},$$

which implies a contribution of $< 10^{-8}$K for $26 \leq \nu \leq 46$ GHz, i.e. the frequency band which POLAR will probe. For these frequencies of observation there is also a small Faraday rotation of the plane of polarization of the CMB. Rosencranz & Staelin [105] show that the rotation of the plane of polarization will be less than $\sim 10^{-2}$ degrees for these frequencies. Therefore, both the polarized emission and Faraday rotation of the atmosphere are negligible effects in the range of frequencies which POLAR probes.

7.6 Summary of Astrophysical Foregrounds

Of all the relevant foreground sources, only diffuse galactic synchrotron radiation and rotating dust are expected to appear at a level comparable to the anticipated polarized CMB signals. We have simulated the performance of POLAR attempting to measure polarization in the presence of foregrounds based upon the general least squares method developed by [106]. To corroborate the results of the analytic error calculation, we have also performed a more explicit foreground removal simulation similar to that of [89]. We find that the effect of the foregrounds is to increase effective per-pixel noise on the recovered Stokes parameters by a factor of ~ 3 [107]. If POLAR can achieve a per-pixel noise lower than 1 μK it will be capable of discriminating a $\sim 1 - 3\mu$K CMB polarization signal from polarized galactic synchrotron radiation.

Chapter 8

Observations

8.1 Site

POLAR's observations are conducted from a custom-built observatory located at the University of Wisconsin's Pine Bluff Observatory, (PBO). PBO is located at Longitude $+89°45'$, Latitude $+43°01'$, approximately 10 miles west of the campus and downtown Madison . Its bucolic location places it in a relatively RF quiet region. The observing platform itself is leftover from the UW Astronomy department's Wisconsin H-Alpha Mapper (WHAM).

A motorized dome encloses the radiometer and rotating ground screen, keeping precipitation out, and maintaining a moderately thermally stabilized enclosure. The dome itself can be operated manually, or remotely via a WWW page in case of inclement weather developing while the experimentalist is elsewhere. The platform has a high-voltage power supply for operation of the CTI 8500 compressor, which requires 220V at roughly 10A. Also running to and from the pad is an Ethernet hub and cables which provide an intranet for data to be transferred from the rotating computer attached to the radiometer

to a desktop workstation located $\sim$ 100' away in a separate building.

8.2 Atmospheric effects

Although the atmosphere is not expected to produce appreciable linearly polarized radiation, it produces a non-negligible contribution to the system temperature of the radiometer. Additionally, significant fluctuations of atmospheric loading increase the low-frequency noise spectrum of the receiver. We summarize the contribution to the antenna temperature seen by the radiometer in the $K_{\rm a}$ band by computing the power spectrum of the atmosphere using a commercial code, AT[1]. To compute the antenna temperature AT requires as input the desired level of precipitable water vapor (PWV). With this specified, AT can compute the antenna temperature vs. frequency using a standard model of the earth's atmosphere. Figure 8.1 shows the atmospheric antenna temperature vs. frequency for various levels of PWV [2].

POLAR convolves the spectrum of the atmosphere with the (power) its transfer function. From this we can compute a direct relationship between PWV and T_{atm}; see figure 8.2.

Since the dominant contribution to the atmospheric temperature comes from the 22 GHz H_2O line rather than on the O_2 line at $\sim$ 60GHz, the dependence on PWV is quite noticeable. Data on PWV is provided by the FAA which uses atmospheric weather balloons (radiosondes) launched at regular intervals, from several major US airports. In figure 8.3 we show a plot of PVW vs. date for 1998 from the nearest sounding balloon

[1]written by Erich Grossmann, Airhead Software, Boulder, Co.

[2]The author wishes to thank Chris O'Dell for the preparation of the AT figures

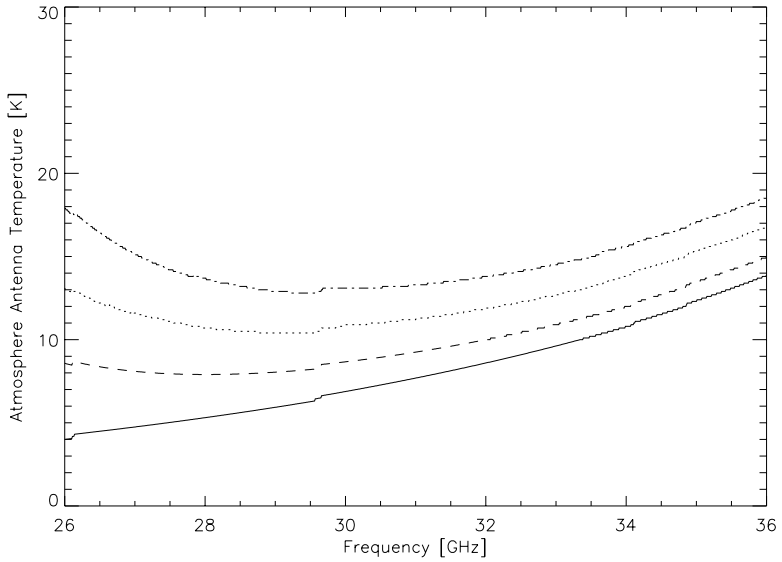

Figure 8.1: Spectrum of Atmospheric Antenna Temperature in the K_a band vs. Precipitable Water Vapor (PWV) . From the top down, the four levels of PWV are: 30mm, 20mm, 10mm, 0mm.

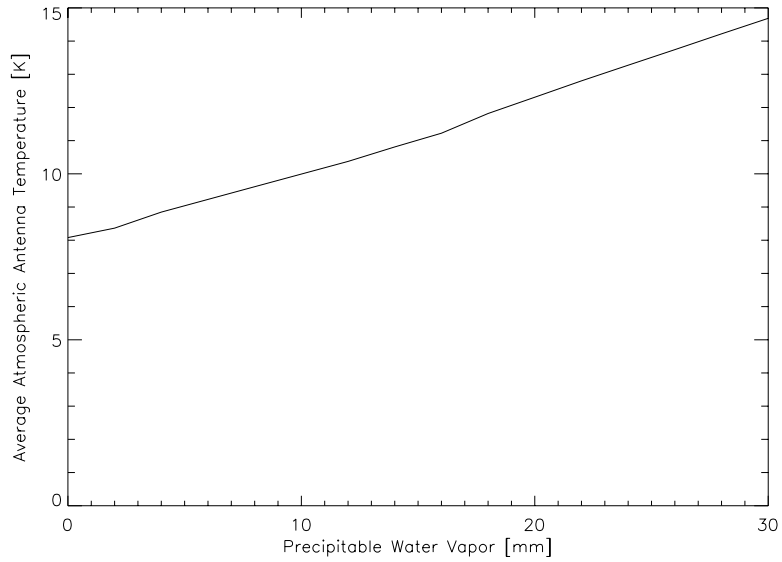

Figure 8.2: Integrated Atmospheric Antenna Temperature in the K_a band vs. Precipitable Water Vapor (PWV)

site in Green Bay, WI. Clearly, observation in the winter is preferred as water vapor in the atmosphere "freezes out", resulting in a low PWV and equivalently, a low atmospheric contribution to our antenna temperature.

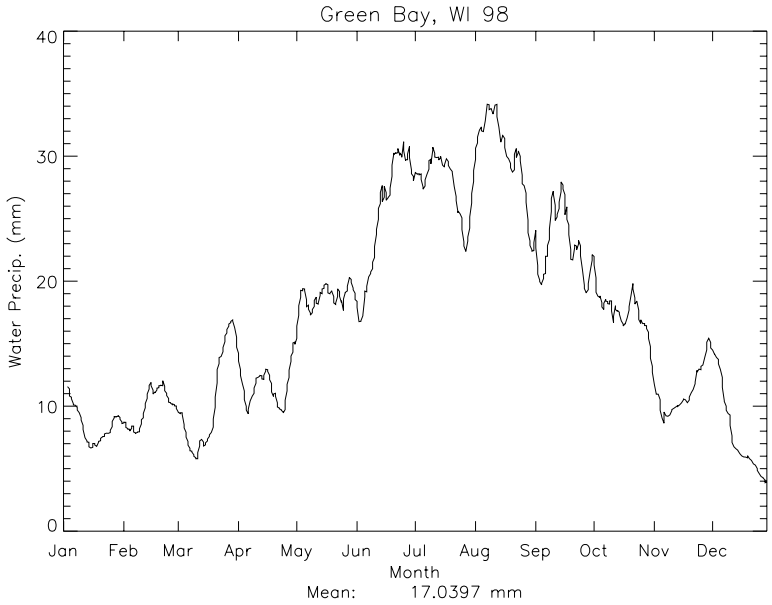

Figure 8.3: Radiosonde-measured Precipitable Water Vapor (PWV) vs. day of 1998 from Green Bay, WI.

As far as the stability of the atmosphere is concerned, we are guided only by theory as we have not yet compiled records of the power spectrum of atmospheric fluctuations at PBO. It is well known that the atmosphere obeys a Kolomogorev spectrum [108], [109]. We can compare the power spectrum of data taken on days which appear to be stable vs. unstable. The effect of atmospheric fluctuations can also be estimated by comparing data taken with the internal cold load, as in Chapter 5, with real data taken while observing.

8.3 Observation Strategy and Sky Coverage

Over a single night, POLAR sweeps out a $7^\circ \times 360^\circ \times \cos 43^\circ = 1844^{\circ 2} FWHM$ swath of the sky. The 36 7° FWHM pixels comprise 5% of the sky. The data is binned in to Stokes

Q and U vs. RA, and multiple nights of data are coadded. The scan passes through the galaxy twice per day at RA$\sim 19h$ and again at RA$\sim 6h$.

Constraints on, or detection of, the polarization of the CMB and its associated power spectrum depend greatly on the amount of sky coverage of the observation as well as the sensitivity of the radiometer. Sensitivity considerations are common to all CMB observations: time limitations restrict signal integration, and constrain the amount of sky coverage. We must reach a compromise between the integration time required to achieve the desired signal-to-noise ratio while also sampling a representative distribution of celestial regions. We now discuss our observing strategy in the context of the achievable level of sensitivity of POLAR.

8.3.1 Sensitivity to the Power Spectrum

POLAR's sensitivity to polarized CMB fluctuations is quantified by its window function, W_ℓ. The observed two-point correlation function is related to the power spectrum and window function as follows:

$$\langle Q(\hat{\mathbf{n}}_1)Q(\hat{\mathbf{n}}_2) + U(\hat{\mathbf{n}}_1)U(\hat{\mathbf{n}}_2)\rangle = \frac{1}{4\pi}\sum_{l=0}^{\infty}(2\ell+1)\times C_\ell^\Pi W_\ell^\theta \times P_\ell(\cos\theta), \qquad (8.1)$$

where, for example, $Q(\hat{\mathbf{n}})$ is the Stokes parameter measured for a pixel located in the direction $\hat{\mathbf{n}}$. C_ℓ^Π is the power spectrum describing the degree of polarization on angular scales characterized by multipole ℓ, W_ℓ^θ is the window function of this observing scheme, and $\cos(\theta) = \hat{\mathbf{n}}_1 \cdot \hat{\mathbf{n}}_2$ is the separation between pixels in this observing scheme.

The analysis of POLAR differs from that of most anisotropy experiments in several respects. The primary difference is that the observations are total-power in nature, rather

than differential. The window functions for this experiment will reflect the fact that there is no "chopping" of the beam in sky position inherent in the observation. Single pixels will be formed by binning the acquired data, and differencing between pixels can be performed during analysis of the data; not during acquisition. This approach avoids systematic effects which can arise from mechanical chopping mechanisms. Data from POLAR will be analyzed using a variety of synthesized window functions, each sensitive to a different angular scale. In this respect the analysis will be similar to that of the Saskatoon Big Plate observations [18, 69].

Window functions for observations with less than full-sky coverage are specified by three functions: the beam profile function, the beam position function, and the weighting or 'lock-in' function [110]. The beam profile function, $G(\theta, \theta_i, \sigma_B)$, where σ_B is the beamwidth, quantifies the directional response of the antenna, which is roughly Gaussian as seen from the beam-maps of Chapter 4. $G(\theta, \theta_i, \sigma_B)$ effectively samples all angular scales larger than, approximately, the angular size of the beam. The angular coordinates of the center of the beam are specified by the beam position function, θ_i. The lock-in function, w_i^α, is the weighting of each of the N binned pixels indexed by i, for the scan strategy denoted by α. We have $G(\theta, \theta_i, \sigma_B) = \frac{1}{2\pi\sigma_B^2} \exp\left(-\frac{(\theta-\theta_i)^2}{2\sigma_B^2}\right)$, where $\sigma_B = FWHM/2\sqrt{2\ln 2} = 0.052$.

Following (White & Srednicki), the window functions are:

$$W_\ell^{\alpha\beta} \equiv \int d\hat{\mathbf{x}}_1 \int d\hat{\mathbf{x}}_2 H^\alpha(\hat{\mathbf{x}}_1) H^\beta(\hat{\mathbf{x}}_2) P_\ell(\hat{\mathbf{x}}_1 \cdot \hat{\mathbf{x}}_1) \tag{8.2}$$

where P_ℓ are the Legendre polynomials, and $H^\alpha(\hat{\mathbf{x}} = \sum_i w_i^\alpha G(\theta, \theta_i, \sigma_B)$ quantifies the response of the antenna (for a differencing strategy indexed by α), when pointed in the

direction of $\hat{\mathbf{x}}$. For a gaussian beam: $H^{\alpha}(\hat{\mathbf{x}}) = \sum_i w_i^{\alpha} \frac{1}{2\pi\sigma_B^2} \exp\left(-\frac{(\theta-\theta_i)^2}{2\sigma_B^2}\right)$.

The ultimate sensitivity of the instrument to the power spectrum, C_ℓ is given by [111]:

$$\frac{\Delta C_\ell}{C_\ell} \sim \Big[\frac{2}{(2\ell+1)}\Big]^{\frac{1}{2}} \Big[1 + \frac{(\Delta Q_{RMS}\theta_{FWHM})^2}{C_\ell} e^{\ell^2\sigma_b^2}\Big] \frac{1}{\sqrt{f_{sky}}} \tag{8.3}$$

where: $\sigma_b = 0.425\theta_{FWHM}$, ΔQ_{RMS} is the per-pixel Stokes parameter sensitivity, and the fraction of the sky covered, f_{sky}, for POLAR is $\sim 5\%$, as mentioned above. At large angular scales, ℓ is small, and since there are only $2\ell + 1$ $a_{\ell,m}$ to estimate C_ℓ, the contribution to the variance in the recovered C_ℓ is large ("Cosmic Variance"). This is the ultimate limit to the error in the power spectra as the per-pixel instrument noise is reduced – there is no gain made by integrating for longer times. However, since POLAR has a large instrument noise, we must integrate for long periods of time such that the second term in equation 8.3 is reduced to the level of $1\mu K$. The long term stability of POLAR is crucial to achieving the levels of instrument noise per-pixel required to make detections of non-zero low-ℓ values of C_ℓ.

Chapter 9

Data Reduction and Analysis

9.1 Data Analysis Methodology

The raw data from the polarimeter consists of eight data channels (2 total power diode detectors, 3 correlators $\times$ two lock-in phase references: in-phase and quadrature phase), the absolute one-bit encoder (AOE) and encoder signals, and numerous housekeeping signals (temperatures of both HEMTs, the horn temperature, the cold stage temperature, the dewar's pressure, and 2 temperature sensors in the room-temperature receiver box, and RTRB heater PID monitor channel). The raw data from the total power detectors are sampled at 20 Hz after leaving the 5 Hz low-pass anti-aliasing filter. For the correlators the raw signal is amplified then sent to a modulator/demodulator which is driven synchronously by either the in-phase or out-phase reference waveform, and then low-pass filters at 5 Hz. Data is collected for 7.5 minutes and then stored to an ASCII file.

The signal processing procedure is composed of the following steps:

- Binning of data by rotation angle and corresponding initial estimation of noise at this bin size.

- Estimates/removal of atmospheric contamination in the correlators using the total power detectors.
- Fits to recover Stokes Q and U for each rotation.
- Binning timestream data into R.A. pixels on the sky, and estimation of noise for a single night of data.
- Co-adding of RA pixels for all nights of data

9.2 Binning of Data

The raw data contains an average of 600 samples per rotation taken at a sampling rate of 20 Hz. The first step in the analysis is to bin the data from the natural sampling angular binsize, $\frac{360^\circ}{600} = 0.6^\circ$ to larger bins in order to have enough data points to have an accurate noise estimate for the subsequent minimum-χ^2-fits. Clearly, it would be nice to have many samples per bin to estimate the noise on the timescale of the bin. However, with a constant rotation rate of $\nu \sim 2$RPM, "smearing" or correlation between bins would be appreciable as we increase the binsize. With the fundamental integration time of 0.2 sec defined by the anti-aliasing filters, there are only $20/\sqrt{5} \sim 9$ independent samples per second. Figure 9.1 shows the first level of binning: into rotation angle only, for ten rotations of the polarimeter ($\simeq$ 5 minutes of data). The data plotted here are from a single high-galactic latitude pixel during excellent observing conditions.

The next step is to co-add all such rotations (within a given time period, thus defining our pixel on the sky) to form a "single-rotation" (for that pixel). This data is then fit for the Stokes parameters, as shown in figure 9.2.

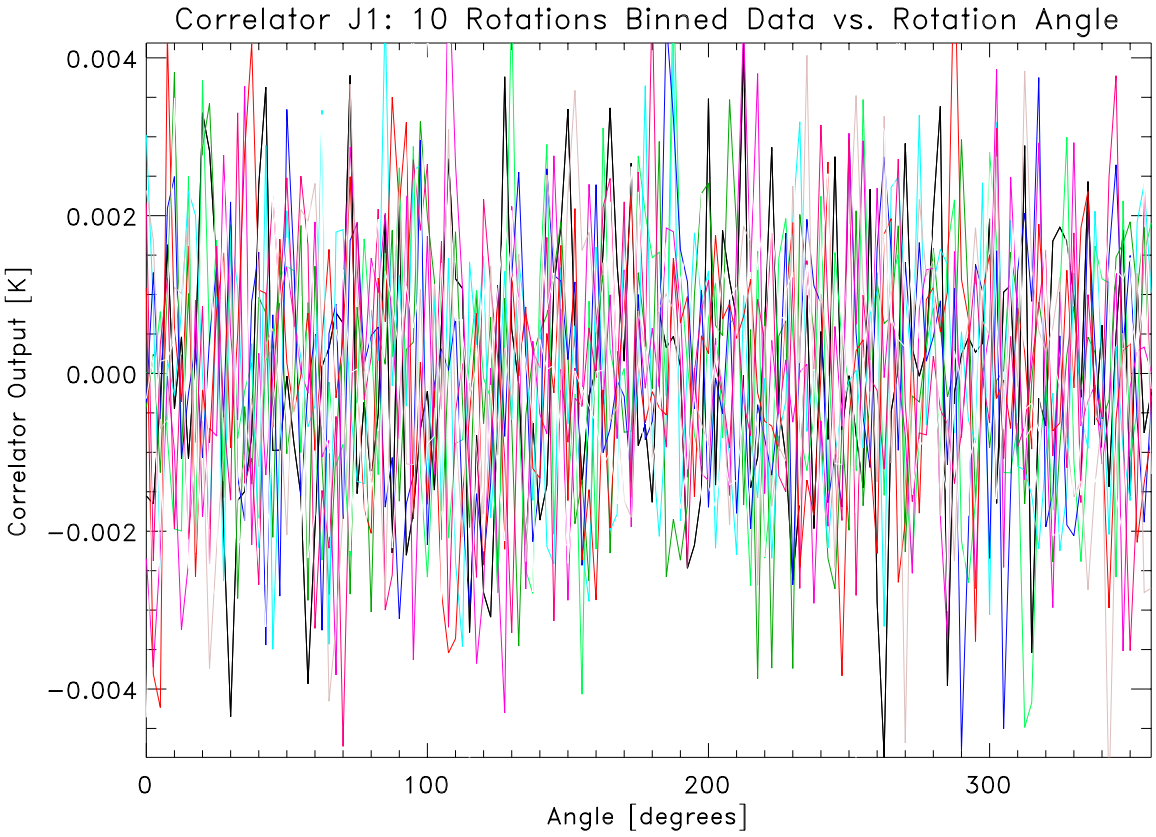

Figure 9.1: Shown here is the output of correlator J1 for ten rotations of the polarimeter. The data are binned into angle, and all rotations are overplotted. No other averaging of the data has been performed .

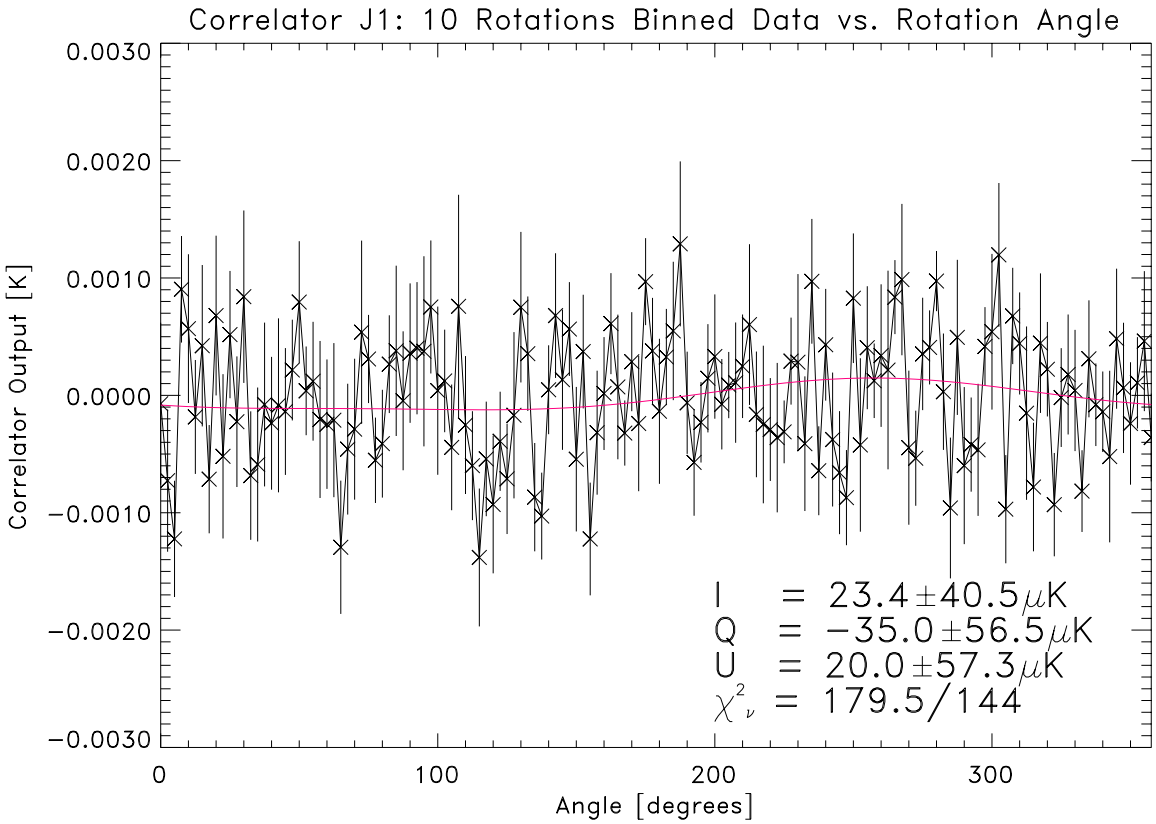

Figure 9.2: Shown here is the output of correlator J1 for ten rotations of the polarimeter, with all rotations averaged and fitted to obtain the Stokes parameters as shown. The data are first binned into angle for each rotation, and then all rotations are co-added to form a single-rotation. The solid line is the fit to the model $S(\theta) = I + Q\cos 2\theta + U \sin 2\theta$. No rotation synchronous *e.g.*, $\cos\theta$ or $\sin\theta$ components have been removed.

9.2.1 Inter-bin Correlations caused by rotation of the polarimeter

Let us model the output of the polarimeter viewing a polarized source as:

$$v(t) = P(t)\sin 2\nu t + n(t) \tag{9.1}$$

where $P = \sqrt{Q^2 + U^2}$. We defer for the moment the "beam-smearing" and its effect on sky pixel-pixel correlation . Also here $P(t) \equiv \texttt{constant} = P_o$, and $n(t)$ is Gaussian distributed noise with variance σ^2.

With $\nu = 0.03$ Hz, we sample $v(t)$ 600 times per rotation and average the results into N bins: $v_i = \frac{1}{\Delta}\int_{t_i-\Delta/2}^{t_i+\Delta/2} v(t)dt$, with $\Delta = 30/N$ (binsize in seconds). From Chapter 1, the convolution theorem asserts that if $y(t) = \int_{-\infty}^{\infty} h(t-t')x(t')dt'$, then :

$$y(t) = \int_{-\infty}^{\infty} \hat{H}(\omega)\hat{X}(\omega)e^{i\omega t}, \tag{9.2}$$

where $\hat{H}(\omega)$ & $\hat{X}(\omega)$ are the Fourier transforms of $h(t)$ & $x(t)$, respectively. In the present case, $h(t) = \frac{1}{\Delta}$ for $t \in \{-\Delta/2, \Delta/2\}$, and is zero elsewhere. Therefore, $\hat{H}(\omega) = \frac{e^{-i\omega\Delta/2}}{\Delta}\frac{\sin\omega\Delta/2}{\omega/2}$. Now we need the spectrum of $v(t) = P_o\sin 2\nu t + n(t)$:

$$\hat{V}(\omega) = \int_{-\infty}^{\infty} v(t)e^{i\omega t}dt \tag{9.3}$$

$$= \int_{-\infty}^{\infty} [P_o\sin 2\nu t + n(t)]e^{i\omega t}dt \tag{9.4}$$

$$= P_o\Big[\tfrac{1}{2i}(\delta(2\nu-\omega) - \delta(2\nu+\omega)) + \hat{N}(t)\Big] \tag{9.5}$$

Our ultimate goal is the power spectrum, $S_y(\omega)$, of the binned data, $S_y(\omega) = |\hat{Y}|^2 = |\hat{H}|^2|\hat{V}|^2 \equiv S_h(\omega)S_v(\omega)$.

This is easily seen to be:

$$S_y(\omega) = \frac{1}{\Delta}\Big[\frac{\sin \omega\Delta/2}{\omega/2}\Big]^2 \Big[\frac{P_o^2}{4}[\delta(2\nu-\omega)+\delta(2\nu+\omega)] + \frac{\sigma^2}{2}\Big]. \tag{9.6}$$

To determine the effect of the binning on our signal and noise, we examine the auto-correlation function (ACF), $R_y(t)$, of $y(t)$ by Fourier transforming $S_y(\omega) - S_n(\omega)$, (where $S_n(\omega)$ is the PSD of the noise):

$$R_v(t) = \textstyle\int_{-\infty}^{\infty} \Big[\frac{\sin \omega\Delta/2}{\omega/2}\Big]^2 \Big[\frac{P_o^2}{4}[\delta(2\nu-\omega)] + \delta(2\nu+\omega)]\Big] e^{i\omega t} d\omega \tag{9.7}$$

$$= \Big[\frac{P_o \sin \nu\Delta}{2\nu\Delta}\Big]^2 \cos 2\nu t. \tag{9.8}$$

The ACF of the binned noise is :

$$R_n(t) = \int_{-\infty}^{\infty} \Big[\frac{\sin \omega\Delta/2}{\Delta\omega/2}\Big]^2 \frac{\sigma^2}{2} e^{i\omega t} d\omega. \tag{9.9}$$

We now define $q(t)$ such that:

$$\int_{-\infty}^{\infty} q(t) dt = \int_{-\Delta/2}^{\Delta/2} dt. \tag{9.10}$$

Then:

$$\tfrac{1}{\Delta}\textstyle\int_{-\infty}^{\infty} q(t) e^{i\omega t} d\omega = \tfrac{1}{\Delta}\int_{-\Delta/2}^{\Delta/2} e^{i\omega t} d\omega \tag{9.11}$$

$$= \tfrac{e^{-i\omega\Delta/2}}{\Delta} \tfrac{\sin \omega\Delta/2}{\omega/2}, \tag{9.12}$$

and then:

$$\int_{-\infty}^{\infty} q(t)q(t')dt = \int_{-\infty}^{\infty} \Big[\frac{\sin \omega\Delta/2}{\omega/2}\Big]^2 e^{i\omega t} d\omega. \tag{9.13}$$

So we need to compute the ACF of $q(t)$, with:

$$q(t) = 1, t \in \{-\frac{\Delta}{2}, \frac{\Delta}{2}\},\ \&\ q(t') = 1, t' \in \{-\frac{\Delta}{2}, \frac{\Delta}{2}\},$$

and:

$$\int_{-\infty}^{\infty} q(t)q(t')dt = \Delta q(t'). \tag{9.14}$$

Substituting into eq. 9.9, we have:

$$\begin{aligned} R_n(t) &= \textstyle\int_{-\infty}^{\infty} \Big[\frac{\sin \omega\Delta/2}{\omega/2}\Big]^2 \sigma^2 e^{i\omega t} d\omega \\ &= \sigma^2 \Big[1 - \Big|\frac{t}{\Delta}\Big|\Big]\ ,\ |t| \le \Delta, \\ &= 0 \quad \text{otherwise.} \end{aligned} \tag{9.15}$$

The best way to quantify the effect of the binning is to look at the signal-to-noise ratio of the binned data, and compare it to the SNR of the unbinned data which is just $\frac{P_o^2}{2\sigma^2}$. The SNR is :

$$SNR = \sqrt{\sigma_v^2/\sigma_n^2}. \tag{9.16}$$

First, we have for the signal:

$$\sigma_v^2 = \int_{-\infty}^{\infty} S_v(\omega) d\omega$$

$$= \frac{2}{\Delta^2} \int_0^{\infty} \left[\frac{\sin \omega\Delta/2}{\omega/2}\right]^2 \left[\frac{P_o^2}{4}[\delta(2\nu - \omega)]\right] d\omega$$

$$= \frac{P_o^2}{2\Delta^2} \left[\frac{\sin 2\pi\nu\Delta}{2\pi\nu}\right]^2$$

for $\nu = 0.03$Hz and $\Delta = \frac{30\text{sec}}{144\text{bins}} = 0.2$ sec/bin , $\sigma_v^2 = 0.04 P_o^2$. Note that if we integrated for a multiple of $\frac{n}{2\nu} \Rightarrow \sigma^2 = 0$, as expected since we would be averaging our signal to zero.

The variance of the noise is:

$$\sigma_n^2 = \int_{-\infty}^{\infty} \Delta |\hat{N}(\omega)|^2 d\omega$$

$$= 2 \int_0^{\infty} \left[\frac{\sin \omega\Delta/2}{\Delta\omega/2}\right]^2 \frac{\sigma^2}{2} d\omega$$

$$\simeq \sigma^2 \int_0^{\infty} \left[\frac{\sin \omega\Delta/2}{\Delta\omega/2}\right]^2 \frac{\sigma^2}{2} d\omega.$$

The SNR^2 then becomes:

$$\frac{\sigma_v^2}{\sigma_n^2} = \frac{P_o^2 \left[\frac{\sin \nu\Delta}{\nu}\right]^2}{\sigma^2 \int_0^{\infty} \left[\frac{\sin \omega\Delta/2}{\omega/2}\right]^2 d\omega}. \tag{9.17}$$

We see that $\Delta \sim 2$ implies that $SNR \sim 1$. This bin size would give us only about 10 points per rotation to recover Q and U, so to be conservative, we take $\Delta = 0.2$s which gives 144 points per rotation.

9.2.2 Is Our Binning Strategy Optimal?

We can now compare the performance of our binning technique with that of our fore bearers Lubin and Smoot [15], hereafter LS, by asking the following: given a rotation time of T_{spin}, what is the optimal distribution of N samples of the output of the polarimeter? For a polarized source, the output of the radiometer is given by: $v(t) = Q\cos 2\psi(t) + U\sin 2\psi(t)$. LS measured the output at 8 locations in angle separated by 45°. To recover the Stokes parameters LS effectively perform a linear least-squares fit to a model, which is parameterized by a model of their expected output. Their observables are essentially two eight-dimensional vectors, one for Q and one for U. To project out the Q (U) content of the eight-dimensional data vector which they observe they multiply by X_1 (X_2):

$$X_1 = \frac{1}{\sqrt{2}}\begin{pmatrix} 1 \\ 0 \\ -1 \\ 0 \\ 1 \\ 0 \\ -1 \\ 0 \end{pmatrix}, \quad X_2 = \frac{1}{\sqrt{2}}\begin{pmatrix} 0 \\ 1 \\ 0 \\ -1 \\ 0 \\ 1 \\ 0 \\ -1 \end{pmatrix}. \tag{9.18}$$

To perform the linear least-squares fit, LS form the *design matrix* [112]: $A_{ij} = \frac{X_i(t_j)}{\sigma(t_j)}$, with $i \in \{1,2\}$ and $j \in \{1,\ldots 8\}$. This results in the following covariance matrix, $C_{ij} = [\alpha_{ij}]^{-1}$, where $\alpha_{ij} = \sum_{k=1}^{8} \frac{X_i(t_k)X_j(t_k)}{\sigma_k^2}$. Assuming equal noise per integration at each position, $\sigma_k = \sigma/\sqrt{T_{spin}/8}$, we have:

$$C_{ij} = \frac{1}{8}\frac{8\sigma^2}{T_{spin}} \begin{pmatrix} 2 & 0 \\ 0 & 2 \end{pmatrix}, \tag{9.19}$$

showing that the estimates for Q and U are uncorrelated.

For POLAR binned to 144 points per rotation, the corresponding design matrix is determined by:

$$X_1 = \begin{pmatrix} \cos 2\nu t_1 \\ \vdots \\ \cos 2\nu t_{144} \end{pmatrix}, \quad X_2 = \begin{pmatrix} \sin 2\nu t_1 \\ \vdots \\ \sin 2\nu t_{144} \end{pmatrix}. \tag{9.20}$$

We find:

$$A_{ij} = \frac{X_i(t_j)}{\sigma(t_j)} = \frac{1}{\sigma_k} \left(\begin{pmatrix} \cos 2\nu t_1 \\ \vdots \\ \cos 2\nu t_{144} \end{pmatrix} \quad \begin{pmatrix} \sin 2\nu t_1 \\ \vdots \\ \sin 2\nu t_{144} \end{pmatrix} \right). \tag{9.21}$$

Now we construct $\hat{\alpha} = \mathbf{\hat{A}^T \hat{A}}$, and the associated covariance matrix $C_{ij} = [\alpha_{ij}]^{-1}$:

$$C_{ij}^{POLAR} = \frac{144\sigma^2}{T_{spin}} \times \begin{pmatrix} \frac{1}{2}(144 - \sum_{i=1}^{144} \cos 4\nu t_i) & \frac{1}{2}\sum_{i=1}^{144} \sin 4\nu t_i \\ \frac{1}{2}\sum_{i=1}^{144} \sin 4\nu t_i & \frac{1}{2}(144 + \sum_{i=1}^{144} \cos 4\nu t_i \end{pmatrix}). \tag{9.22}$$

At first glance this covariance matrix appears to have off-diagonal elements – *i.e.*, we seem to have correlated our errors on Q and U. However, by symmetry [1], all of the sums in equation 9.22 are equal to zero, leaving us with the resulting diagonal covariance matrix:

$$C_{ij}^{POLAR} = \frac{1}{144}\frac{144\sigma^2}{T_{spin}} \begin{pmatrix} 2 & 0 \\ 0 & 2 \end{pmatrix}. \tag{9.23}$$

[1] $\sum_{i=1}^{N} \sin 2\pi i/N = 0$

Now we can compare equations 9.19 and 9.23. We assume that the entire rotation time is used for integrations for each method. The LS method will combine 8 measurements, with variance $8 \times \sigma^2/T_{spin}$ to achieve a final variance of $2 \times \sigma^2$. Similarly, POLAR will combine 144 samples with variance $144 \times \sigma^2/T_{spin}$ to obtain final variance of $2 \times \sigma^2$, which is equivalent to the minimum detectable temperature for the LS method. Thus, for both LS and POLAR the standard deviations of Q or U will be a factor of $\sqrt{2}$ times larger than would be obtained for an intensity measurement given the same length of time.

In practice, not all of the time for a given rotation can be used for integrations in the LS method. Time is lost moving between angular positions, and the polarimeter is not capable of stopping instantaneously so it must be slowed to a stop. Therefore, given a fixed time per revolution, set perhaps by the characteristic timescale of fluctuations of atmospheric emission, the method used for POLAR is preferable.

Finally, although the errors on Q and U are uncorrelated, the noise in the time stream *is* correlated between adjacent bins for two reasons:

- the anti aliasing filter has non-vanishing correlation on timescales less than 0.2 sec.
- the output from the correlator is correlated with the output from the total power channels due to the presence of the correlated atmospheric component present in each total power channel.

We will expand upon the abrogation of the second of these phenomena in the following section.

9.3 Correlation Between Sky Pixels

A deficiency of the drift scan method employed by POLAR is that adjacent pixels share significant correlated signal. We now present a formalism to address this concern, and estimate its effect on our results. Let us model the output of the polarimeter when viewing in the direction θ as:

$$P(t) = P(\theta)\sin\phi(\Omega t) + n(\Omega t) \tag{9.24}$$

where $\Pi = \sqrt{Q^2 + U^2}$ and ϕ is the RA, Ω is the rotation rate of the earth. The zenith in Madison, WI corresponds to a declination of $\delta = 43^\circ$. In 24 hours of right ascension there are $360^\circ \cos 43^\circ \simeq 255^\circ$ along our scan. With the angular rotation rate of the earth: $\omega \simeq 1.2 \times 10^{-5}$Hz, we co-add 7.5 minutes of data to form a single bin of angular size $1^\circ.32$. Our beam size is $\sim 7^\circ$ which implies that adjacent bins will share significantly correlated signal, upto a lag of ~ 5 bins. From the individual bins we therefore co-add several bins to form a single larger bin with (hopefully) larger signal and lower noise. The behavior of the noise during this binning is our first indication of the performance of the instrument, as the signal contribution is clearly subdominant.

First we model the output signal as the convolution of the true sky signal, $\Pi(\theta)$, with the normalized antenna power response function[2], $B(\theta)$:

$$P(\theta) = \int_{-\infty}^{\infty} \Pi(\theta) B(\theta - \psi) d\psi. \tag{9.25}$$

[2]assumed to be azimuthally symmetric

From the convolution theorem we have:

$$P(\theta) = \int_{-\infty}^{\infty} \hat{\Pi}(k)\hat{B}(k)e^{2\pi ik\theta}dk, \tag{9.26}$$

where $\hat{\Pi}(k)$ and $\hat{B}(k)$ are the Fourier transforms of $\Pi(\theta)$ and $B(\theta)$.

We would like to know how much correlation our binned pixels have between them. The binning in angle effectively introduces a low-pass filter, $H(k)$. The spectrum of the binned pixels will be given by: $P(k) = H(k)\Pi(k)$. The binned pixels are then $P(\theta) = \frac{1}{\Delta}\int_{-\infty}^{\infty} P(k)e^{2\pi ik\theta}dk$. $H(k)$ is given by:

$$H(k) = \frac{1}{\Delta}\int_{\theta_i-\Delta}^{\theta_i+\Delta} e^{2\pi ik\theta'}d\theta' = \frac{1}{\Delta}\frac{\Delta e^{2\pi i\theta_i}}{2\pi k}\frac{\sin 2\pi k\Delta}{2\pi k\Delta} \tag{9.27}$$

where $2\Delta = 200\text{bins}/255^\circ \times 5 \simeq 1^\circ.32$.

The most direct method is to compute the autocorrelation function of the measured sky data $P_i(\theta)$ and find the lag in degrees where it falls to zero. The autocorrelation function of $P_i, \langle P_i(\theta)P_i(\theta')\rangle$, assuming statistical isotropy of $P_i(\theta)$ is only dependent on the angular *separation* $\theta - \theta'$, and is given by:

$$\langle P_i(0)P_i(\theta')\rangle = \int_{-\infty}^{\infty} P_i(\theta)P_i(\theta-\theta')d\theta \tag{9.28}$$

$$= \int_{-\infty}^{\infty} \hat{\Pi}(k)\hat{\Pi}(k)\hat{B}(k)\hat{B}(k)e^{2\pi ik\theta}dk \tag{9.29}$$

$$= \int_{-\infty}^{\infty} C_k W_k e^{2\pi ik\theta}dk, \tag{9.30}$$

where the wavenumber $k \sim \ell$.

An alternative method to check for non-vanishing correlation between sky pixels is to

examine the power spectra of the binned data. We can think of the averaging procedure used during construction of the sky bins as a low-pass filter, and then convolve the filter response function with the data of the 7.5 minute bins. This is best done in the frequency domain where the convolution is the inverse Fourier transform of the product of the equivalent transfer function (*i.e.* spectrum) of the filter and the angular/time spectrum of the 7.5 minute data. This Fourier analysis will also allow us to identify periodicities in the raw 7.5 minute bins which, since the astronomical signal is negligible, can only be attributed to systematic effects in our data. By looking at the measured power spectrum we can determine the range of angles over which our binning strategy introduces correlations, just as in the case of an RC low-pass filter where frequencies less than the reciprocal of the time-constant can be considered independent.

$$\begin{aligned} \langle P_i(0)P_i(\theta')\rangle &= \int_{-\infty}^{\infty} P_i(\theta)P_i(\theta-\theta')d\theta \\ &= \int_{-\infty}^{\infty} \hat{\Pi}(k)\hat{\Pi}(k)\hat{B}(k)\hat{B}(k)e^{2\pi ik\theta}dk \\ &= \int_{-\infty}^{\infty} C_k W_k e^{2\pi ik\theta}dk. \end{aligned} \tag{9.31}$$

Here we have introduced the notation $C_k = \hat{\Pi}^2(k)$ and $W_k = \hat{B}^2(k)$. Of course C_k is our main quarry, so it is not possible to substitute its value into eq. 9.31 *a priori*. However, over a small range of angular scales (in POLAR's case, *at* large angular scales), we take $C_k = \texttt{constant} = C_\Pi$.

The measured power spectrum in terms of the true power spectrum is given by:

$$C_k^{meas} = C_\Pi \frac{\sin^2 2\pi k\Delta}{4\pi^2 k^2} W_k. \tag{9.32}$$

The measured window function, W_k, is given by:

$$\begin{aligned} W_k &= \left|B(k)\right|^2 = \left| \int_{-\infty}^{\infty} B(\theta) e^{2\pi i k\theta} d\theta \right|^2 \\ &= \left| \int_{-\infty}^{\infty} e^{-(\theta^2/2\theta_o^2)} e^{2\pi i k\theta} d\theta \right|^2 \\ &\propto e^{-8\pi^2 k^2 \theta_o^2}, \end{aligned} \tag{9.33}$$

showing the correlation induced by "beam smearing" is largest at small scales since the power spectrum is largest at large angular scales. This window leads to:

$$C_k^{meas} = C_\Pi \frac{\sin^2 2\pi k\Delta}{4\pi^2 k^2} e^{-k^2\theta_o^2/2}. \tag{9.34}$$

Notice that it is not possible to choose a binning which completely removes pixel-pixel correlations. On bins of $3^\circ.5$ which correspond to the timescale of the individual data files, we see that the correlation is $\sim 50\%$, as intuition would predict.

Chapter 10

Results

This thesis has described a work in progress: the $K_{\rm a}$ band incarnation of POLAR. POLAR is currently acquiring data and the performance of the instrument can now be assessed. Preliminary indications suggest that the instrument is functioning quite well, though only by conducting long-term observations will we be able to determine low-level systematic effects "lurking" in the data set.

In this Chapter we present results of an initial data run of POLAR observing the sky during the late summer months of 1999. Finally, we present calculations of the expected signal level for models with early reionizatoin and outline an analysis formalism which will be implemented in an effort to cross-correlate the future POLAR dataset with the existing COBE DMR data set. This latter analysis is expected to give us a significant signal-to-noise advantage over the calculation of the polarization auto-correlation alone.

10.1 Expected Long-Term Performance of POLAR

As mentioned in Chapter 4, the sensitivity of the polarimeter is primarily determined by its cooled HEMT amplifiers which have noise temperatures of ~ 65 K; far greater than the state-of-the art devices which now achieve noise temperatures of $\sim$ 10K in the $K_{\rm a}$ band [113], [114]. This noise temperature is comparable to the antenna temperature of the atmosphere at a good observing site. As shown in Chapter 5, POLAR's $K_{\rm a}$-band HEMTs are much noisier, resulting in a contribution to the system noise temperature of nearly five times the atmospheric level in the $K_{\rm a}$ band.

However, even with these devices we believe POLAR will be able to produce cosmologically significant upper limits on the polarization of the CMB for a universe with no reionization, or possibly a detection of polarization for a universe with early reionization. Long integration periods will be required to reach a sensitivity level $\simeq 1-10\mu$K per-pixel, which would allow us to produce these results. We recall that the RMS noise in a measurement of either Q or U (in antenna temperature) is given by the radiometer equation [20], which for the Q Stokes parameter is:

$$\Delta Q_{RMS} = \frac{\kappa(T_{rec} + T_{atm} + T_{CMB})}{\sqrt{\Delta\nu\tau/2}}, \tag{10.1}$$

where T_{rec} and T_{atm} are the receiver and atmospheric noise temperatures, respectively. τ is the total time spent observing the CMB; the time spent either Q or U is $\tau/2$. $\Delta\nu$ is the radio frequency (RF) bandwidth and as we have shown in Chapter 3, $\kappa = \sqrt{2}$ for a correlation radiometer. For the K_a polarimeter, $T_{rec} \simeq 75$K and $T_{atm} \simeq 12$K. If all three correlators can be combined $\Delta\nu$ is ~ 6 GHz, resulting in a sensitivity to Q or U of $NET = \Delta Q_{rms} \simeq 2\text{mK}s^{1/2}$. For the total polarized intensity we have: $I_{\rm pol} = \sqrt{Q^2 + U^2}$.

The error in $I_{\rm pol}$ is $\Delta I_{\rm pol} = \sqrt{2}\Delta Q_{rms}$, before foreground subtraction.

10.2 Long-Term Integration Tests

We note that equation 10.1 indicates that $\log[\Delta T_{RMS}(\tau)]$ vs. τ should be linear with slope equal to $-\frac{1}{2}$. Figure 10.1 shows a plot of $\log[\Delta Q_{RMS}(\tau)]$ and $\log[\Delta U_{RMS}(\tau)]$ vs. τ formed by combining correlator channels J1 and J2 for a single night of data. The data points are compared with the theoretical expectation values. Judging from the continuing trend towards decreasing noise in POLAR's correlator channels we fully expect that the long-term stability of the instrument will allow us to set the most restrictive limits on the polarization of the CMB.

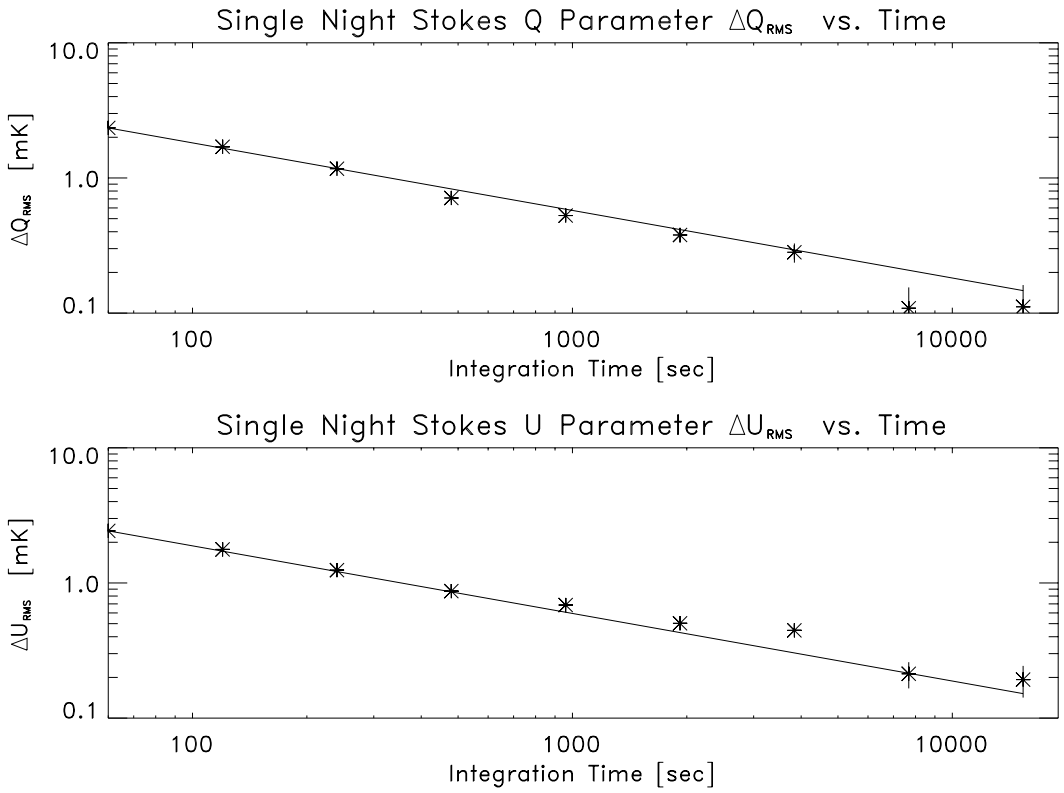

Figure 10.1: Long term integration behavior of the noise in the Stokes Q and U parameters for one night $\sim$ 10 hours of data. The solid line indicated the expected behavior of the noise vs. integration time ΔQ_{RMS} or $U_{RMS} \propto 1/\sqrt{t}$.

10.3 Estimated Polarized Signal Level and Uncertainty

10.3.1 Estimated Total Signal Level in Models with Early Reionization

To simulate the performance of POLAR, we have used the state-of-the-art Boltzmann code CMBFAST to generate all relevant power-spectra. Since the power spectra are not immediately useful we have invoked the standard procedure of map-generation; see *e.g.* [115]. Polarization maps are traditionally plotted as "sticks" with amplitude $(Q^2+U^2)^{1/2}$ and orientation angle $(1/2)\tan^{-1}(U/Q)$, following from the definitions of the Stokes parameters. For all figures which depict the polarization we plot the polarization amplitude, not Q or U directly. The maps[1] are quite helpfull for use in simulations of the instrument's performance in the presence of foregrounds and other experimental non-idealities.

First we show the temperature anisotropy sky realization for a "standard CDM" model with no reionization in figure 10.2.

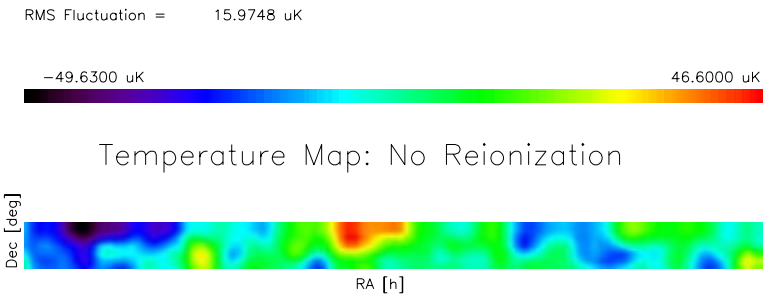

Figure 10.2: Simulated temperature anisotropy map made using CMBFAST. A "standard CDM" model with no reionization produces the underlying power spectrum which is used to generate a realization of the sky which is subsequently convolved with the beam pattern of POLAR to create this figure. From right to left the range of RA is $0h \leq RA < 24h$, and from top to bottom the range of Declination is $20° \leq \delta < 60°$. POLAR's observing strip appears in the middle of the figure.

Next we show the temperature anisotropy sky realization for a "standard CDM" model with reionization at $z = 50$ in figure 10.3.

[1]Prepared by Nate Stebor

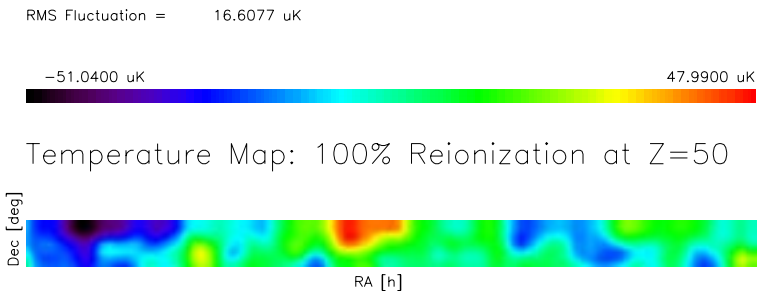

Figure 10.3: Simulated temperature anisotropy map made using CMBFAST. A "standard CDM" model with reionization at $z = 50$ produces the underlying power spectrum which is used to generate a realization of the sky which is subsequently convolved with the beam pattern of POLAR to create this figure. From right to left the range of RA is $0h \leq RA < 24h$, and from top to bottom the range of Declination is $20° \leq \delta < 60°$. POLAR's observing strip appears in the middle of the figure.

From figures 10.2 and 10.3 we see that the effect of early reionization on the temperature anisotropy at large angular scales is undetectable. This is to be expected as the primary effect of reionization is to suppress the temperature anisotropy at sub-degree angular scales [57]. Now we show the polarization sky realization for a "standard CDM" model with no reionization in figure 10.4.

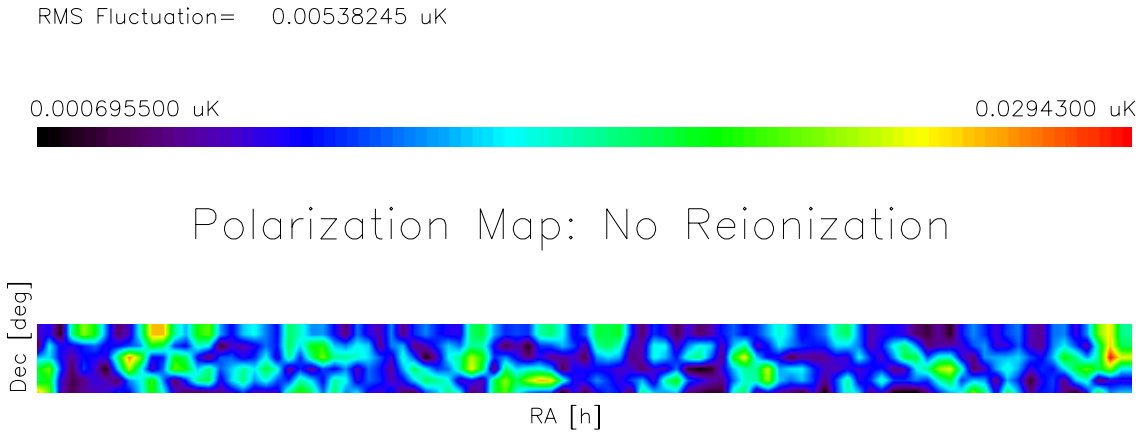

Figure 10.4: Simulated polarization map made using CMBFAST. A "standard CDM" model no reionization produces the underlying power spectrum which is used to generate a realization of the sky which is subsequently convolved with the beam pattern of POLAR to create this figure. From right to left the range of RA is $0h \leq RA < 24h$, and from top to bottom the range of Declination is $20° \leq \delta < 60°$. POLAR's observing strip appears in the middle of the figure.

Finally we show the dramatic enhancement of the polarization for a model with early reionization at a redshift of $z = 50$ in 10.5.

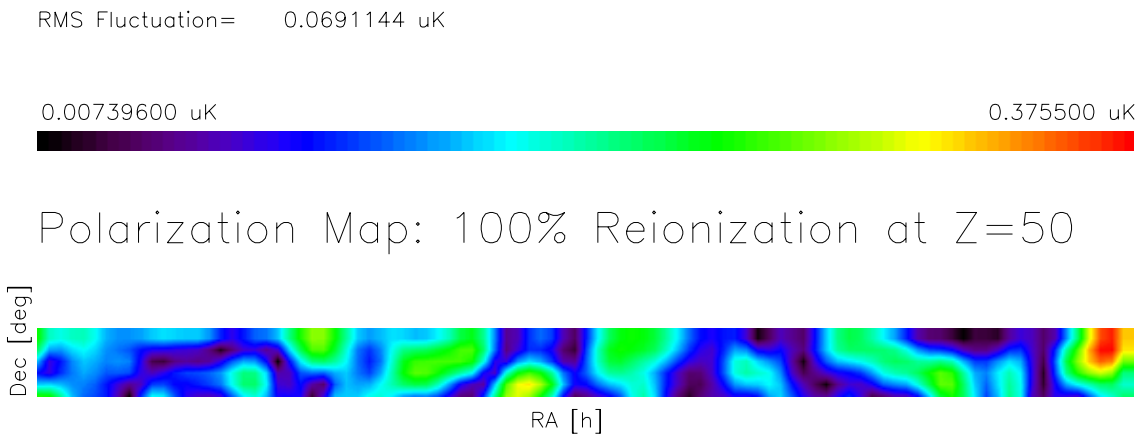

Figure 10.5: Simulated polarization map made using CMBFAST. A "standard CDM" model with reionization at $z = 50$ produces the underlying power spectrum which is used to generate a realization of the sky and subsequently convolved with the beam pattern of POLAR to create this figure. From right to left the range of RA is $0h \leq RA < 24h$, and from top to bottom the range of Declination is $20^\circ \leq \delta < 60^\circ$. POLAR's observing strip appears in the middle of the figure.

Comparing figures 10.4 and 10.5, we see that the polarization of the CMB is enhanced by a factor of ten, to levels which are within reach of POLAR assuming a sensitivity of $\sim 1\mu$K per-pixel for all 36 pixels. This figure reinforces the conclusions of Chapter 2: the level of polarization is extremely sensitive to the ionization history of the universe, both before and after recombination. We expect, then, that the observed polarization signal will depend critically on the optical depth, τ, for photons back to the last scattering surface. A preliminary estimate of the effect of reionization can be obtained by computing the expected RMS polarization and associated experimental uncertainty for models of a reionized universe. Figure 10.6 reinforces our claims that the effect of reionization is most pronounced in the polarization, not the CMB. This effect allows the degeneracy between parameters such as H_o and τ to be broken , which will ultimately allow [57] for higher-precison estimates of both [57].

Recall in Chapter 2 we presenteed figure 2.5 which displayed C_ℓ^Π, for the power spectrum computed using CMBFAST for various totally reionized (ionized fraction $x = 1$) scenarios, parameterized by the redshift of reionization $z_{\rm ri}$. In Figure 10.7 we plot the expected RMS polarization vs. $z_{\rm ri}$, for $0 < z_{\rm ri} < 105$, along with the statistical 1σ un-

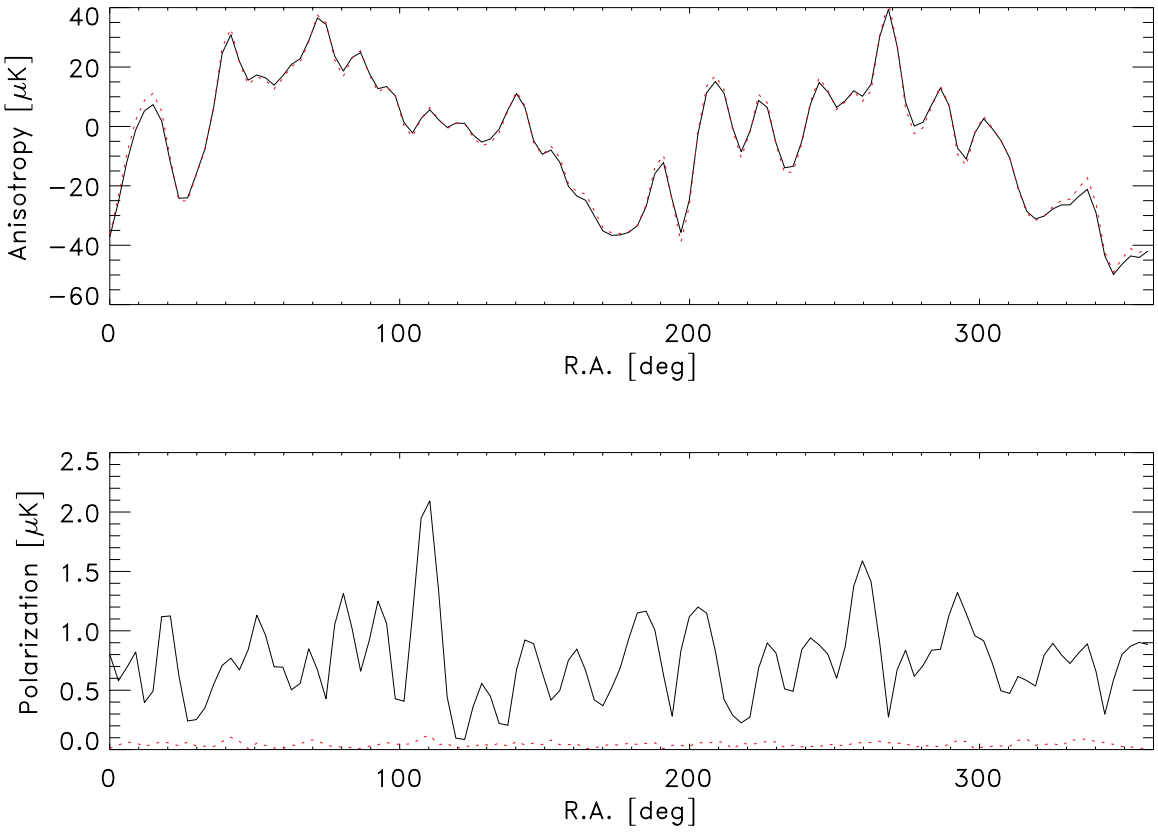

Figure 10.6: Simulated observations of CMB anisotropy and polarization from Madison, WI. Power spectra are generated using CMBFAST and convolved with the POLAR beam size and observing strategy to create realizations of the sky as seen from our observing location. Correlation between anisotropy and polarization is taken into account. The solid lines correspond to total reionization at $z = 50$, and the dotted lines correspond to no reionization. Note that the effect of reionization is nearly unnoticeable for the anisotropy, while for the polarization its effect is quite dramatic.

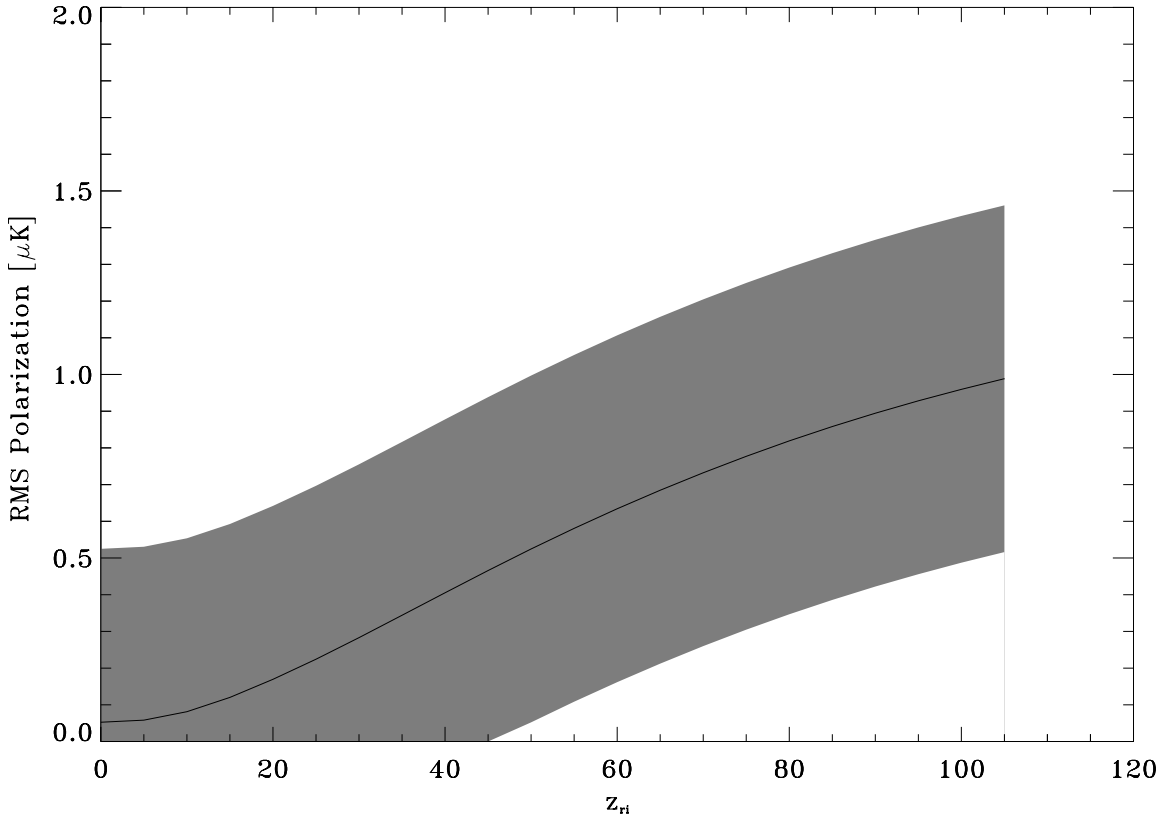

Figure 10.7: Simulated Per-Pixel RMS polarization vs. redshift of reionization. Also shown is POLAR's expected 1σ per-pixel error bars for $\sim$ one-year of observations. No correlations have been taken into account. Combining all 36 pixels would result in a reduction in the errors by a factor of ~ 6.

certainties we expect based on our NET and observation time. The underlying power spectrum is a generic CDM model with $\Omega = 1, \Omega_B = 0.05, h = 0.65, \Lambda = 0$, and pure scalar perturbations. The inclusion of a tensor component should enhance the large angular scale polarization [47], [116], so this figure underestimates the RMS polarization predicted by some cosmological models. This figure suggests that POLAR could begin to detect polarization of the CMB at the 1σ level if the universe became completely reionized at a redshift $z_{\rm ri} > 45$.

10.4 Temperature-Polarization Cross-Correlation and COBE

CMB polarization can be decomposed into two components: one of which is spatially correlated with the temperature anisotropy, and another, larger component which is uncorrelated. Ng & Ng [45] and Crittenden, Coulson, & Turok [116], demonstrate that, given a high-resolution CMB temperature map, it would be possible to identify celestial regions which are statistically more likely to posses higher levels of the correlated polarization component. As shown in [117], the uncorrelated polarization component dominates the correlated component by a factor of at least three.

For detector-noise limited polarization experiments, it can be advantageous to search for polarization-anisotropy $\langle QT \rangle$ correlation in addition to polarization-polarization $\langle QQ \rangle$ cross-correlation. If the noise in the temperature anisotropy map is negligible in comparison with the noise of the polarization measurement, σ, the error in $\langle QT \rangle$ will be linear in σ while the variance in the polarization auto-correlation function grows as σ^2. In this limit it becomes advantageous to search for cross-correlation.

10.4.1 Correlations Between Temperature and Stokes Parameters

Due to the assumption that the universe is statistically isotropic we expect that two-point correlation functions of the Stokes parameters will only depend on the angular separation between the two points. This assumption is implicit, for example, when we expand the temperature autocorrelation function into Legendre Polynomials rather that spherical harmonics. Unfortunately, due the explicit reference to a particular coordinate system for the definition of our experimentally measured Stokes Parameters, *i.e.*, $Q \equiv T_{NS} - T_{EW}$, simply correlating Q and U in a particular coordinate system gives correlation functions which depend on the positions of the points being correlated as well the angular

separation [118]. This was the situation prior to Kamionkowski, Kosowsky, and Stebbins (KKS) and Seljak and Zaldarriaga [55], [52].

As mentioned in Chapter 2, two prescriptions to specify coordinate independent parameters exist, either the expansion into rank-2 symmetric tensors on the celestial 2-sphere, or into spin-weighted spherical harmonics. To obtain the real-space correlation functions of Stokes parameters we define Q and U with respect to axes which are parallel and perpendicular to the great arc (or geodesic) connecting the two points being correlated. So Q_r is the difference in intensities in two linear-polarization states parallel and perpendicular to the great arc connecting the two points, and U_r is the difference in two linear-polarization states which lie 45° away from the parallel and perpendicular[57]. This is reminiscent of the more familiar notion of parallel transport in differential geometry, except now we are computing the derivative of a spinor on a curved manifold rather than a (more-simple) vector.

Since we have three observables T, Q, U we expect 3! different two-point correlation functions to be relevant if the CMB can be treated as a gaussian random field. We denote the six correlation functions as:

$\langle TT\rangle$, $\langle U_r U_r\rangle$, $\langle Q_r Q_r\rangle$, $\langle Q_r T\rangle$, $\langle Q_r U_r\rangle$, and $\langle U_r T\rangle$. Due to the expected symmetry of the universe under parity transformations we will find that Q_r is invariant under reflection along the great arc connecting the two points being correlated, U_r will change sign under this symmetry transformation. T, being a scalar function, will obviously be invariant.

So we expect that the ensemble averages $\langle Q_r U_r\rangle$ and $\langle U_r T\rangle$ will be zero. A hint in this direction was provided in Chapter 2 where we found that there were only four nonzero sets of moments $C_l^{\rm T}$, $C_l^{\rm G}$, $C_l^{\rm C}$, and $C_l^{\rm TG}$. Correspondingly, four nonzero correlation functions provide an equivalent statistical description.

Following KKS, we now examine the auto and cross-correlation functions. First, for reference, we start with the temperature auto-correlation function: $\langle TT \rangle$:

$$C^{\rm T}(\theta) = \left\langle \frac{T(\hat{\mathbf{n}}_1)}{T_0} \frac{T(\hat{\mathbf{n}}_2)}{T_0} \right\rangle_{\hat{\mathbf{n}}_1 \cdot \hat{\mathbf{n}}_2 = \cos\theta}. \tag{10.2}$$

Since, as mentioned above, the correlation function depends only on the angular separation of the two points, without loss of generality, we may choose one point to be at the north pole, $(0,0)$, and the other to be on the $\phi = 0$ longitude at a distance θ from the north pole, $(\theta, 0)$. Next we expand $T(\hat{\mathbf{n}})$ in terms of spherical harmonics and note that $Y_{(lm)}(0,0) = \delta_{m0}\sqrt{(2l+1)/(4\pi)}$. So

$$\begin{aligned} C^{\rm T}(\theta) &= \left\langle \frac{T(0,0)}{T_0} \frac{T(\theta,0)}{T_0} \right\rangle \\ &= \sum_{lml'm'} \left\langle a^{{\rm T}\,*}_{(lm)} a^{\rm T}_{l'm'} \right\rangle Y^*_{(lm)}(0,0) Y_{(l'm')}(\theta,0) \\ &= \sum_{lml'm'} C^{\rm T}_l \delta_{ll'} \delta_{mm'} \sqrt{\frac{2l+1}{4\pi}} \delta_{m0} Y_{(l'm')}(\theta,0) \\ &= \sum_l \frac{2l+1}{4\pi} C^{\rm T}_l \, P_l(\cos\theta). \end{aligned} \tag{10.3}$$

For the $\langle QQ \rangle$ correlation function we have that:

$$C^Q(\theta) = \left\langle \frac{Q_r(\hat{\mathbf{n}}_1)}{T_0} \frac{Q_r(\hat{\mathbf{n}}_2)}{T_0} \right\rangle_{\hat{\mathbf{n}}_1 \cdot \hat{\mathbf{n}}_2 = \cos\theta}, \tag{10.4}$$

where the Stokes parameter Q_r is defined as the difference in brightness between axes parallel and perpendicular to the great arc connecting $\hat{\mathbf{n}}_1$ and $\hat{\mathbf{n}}_2$. Again we are free to choose one point to be at the north pole and another a distance θ away along the $\phi = 0$ longitude. This choice has the added advantage that the great arc connecting these two

points is along the θ direction, so we can use the Q defined in the $(\hat{\theta}, \hat{\phi})$ coordinate system. As a consequence of the "hairy-ball" theorem of topology [119], in *all* choices of spherical coordinate systems there will be two points (poles) where the azimuthal coordinate is ill-defined. In the particular spherical coordinate system we are considering, the definition of Q at the north pole is ambiguous. As long as we agree not to discuss the polarization at the pole we can always consider a point on the $\phi = 0$ longitude which is infinitesimally close to the north pole; in other words, $Q(0,0)$ really means $\lim_{\theta\to 0} Q(\theta, 0)$. For the $\langle UU \rangle$ correlation function, the derivation is similar, giving

$$C^U(\theta) = -\sum_l \frac{2l+1}{2\pi} N_l^2 [C_l^{\rm C} G^+_{(l2)}(\cos\theta) + C_l^{\rm G} G^-_{(l2)}(\cos\theta)]. \tag{10.5}$$

For the $\langle TQ \rangle$ cross-correlation function,

$$\begin{aligned} C^{\rm TQ}(\theta) &= \left\langle \frac{T(\hat{\mathbf{n}}_1)}{T_0} \frac{Q_r(\hat{\mathbf{n}}_2)}{T_0} \right\rangle_{\hat{\mathbf{n}}_1 \cdot \hat{\mathbf{n}}_2 = \cos\theta} \\ &= \sum_l \frac{2l+1}{4\pi} N_l \, C_l^{\rm TG} \, P_l^2(\cos\theta). \end{aligned} \tag{10.6}$$

10.4.2 The COBE DMR Instrument

The COBE DMR experiment performed its primary task exceptionally well: it made the first unambiguous detection of the anisotropy of the CMB [120]. The success of the instrument is largely attributable to the robust construction of the instrument, the stable observing location, and observing strategy and analysis which were subsequently carried out. In addition to its ability to detect the anisotropy of the CMB, COBE also had the ability to detect the polarization of the CMB. Due to the complicated observation strategy implemented in an effort to glean maximum information regarding the anisotropy,

polarization results from COBE are not particularly restrictive [121].

The greatest usefulness of the COBE instrument towards a detection of polarization of the CMB may be yet to come. As we will show, it is possible for an instrument such as POLAR to detect the cross-correlation of polarization with the temperature anisotropy *without* detecting the polarization auto-correlation itself. In a loose sense, since the temperature anisotropy of the CMB observed today on all scales is the bears the imprint of the quadrupole anisotropy at decoupling, and the polarization of the CMB is correlated with the this quadrupole anisotropy as well, we expect that polarization and temperature anisotropy will be correlated. In fact, cross-correlation may provide the only link between previous detections (of anisotropy), and the proposed measurements discussed in this thesis.

10.4.3 Model and Data Input

To place interesting limits on the polarization-temperature cross-correlation function we require two inputs in addition to the POLAR dataset: a well-sampled temperature anisotropy map, and a theoretical model of the power spectrum. The power spectrum will depend upon several cosmological parameters, one of which τ – the optical depth due to reionization, has a dramatic effect on the large angular scale polarization, and not the temperature anisotropy. Thus, a significant detection of polarization-temperature cross-correlation may actually prove to be the initial observable detected by POLAR. To prepare for this analysis, in figure 10.8 we show the COBE temperature anisotropy map centered on POLAR's observing fields.

Given this map, we now require a model for the temperature-polarization cross-correlation function. In addition to the anisotropy and polarization spectra, CMBFAST also computes

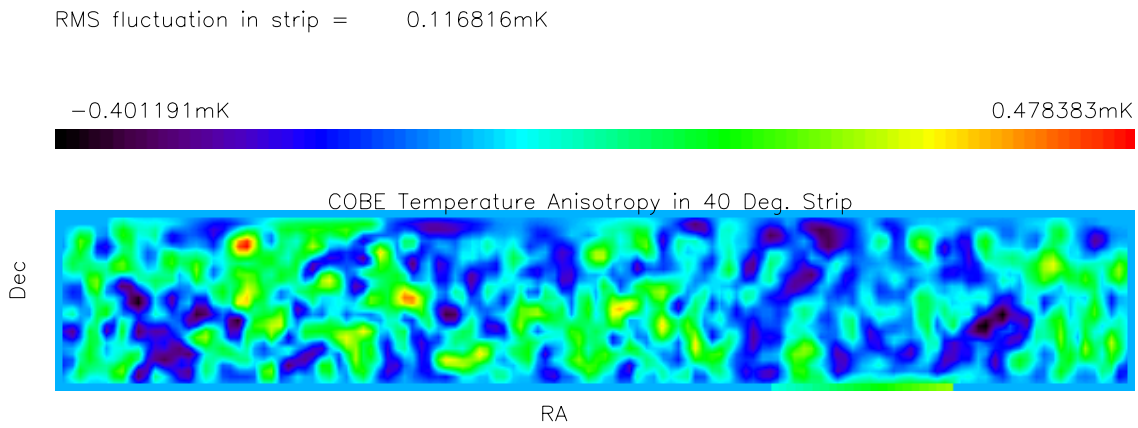

Figure 10.8: COBE Temperature Anisotropy Centered on POLAR's Observing Fields. From right to left the range of RA is $0h \leq RA < 24h$, and from top to bottom the range of Declination is $20° \leq \delta < 60°$. POLAR's observing strip appears in the middle of the figure.

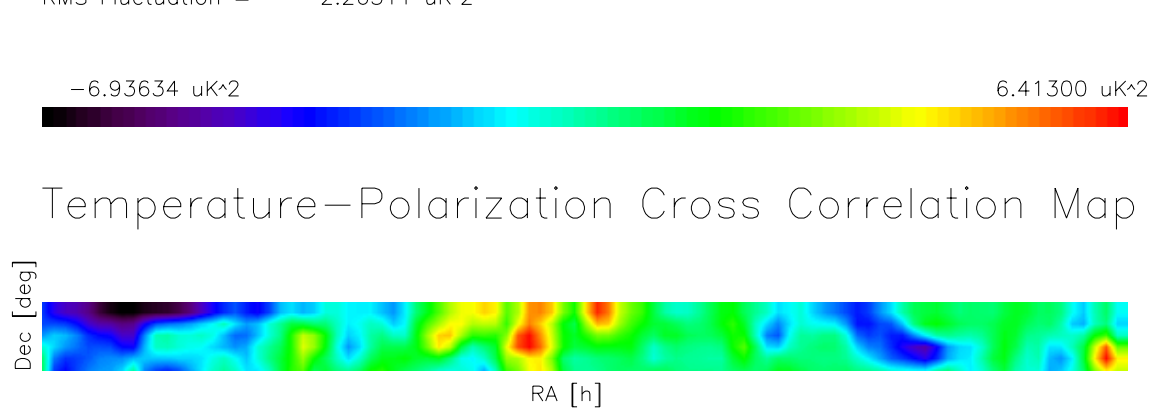

Figure 10.9: Simulated polarization-temperature cross-correlation map made using CMBFAST. Total reionization at z = 50 is assumed. From right to left the range of RA is $0h \leq RA < 24h$, and from top to bottom the range of Declination is $20° \leq \delta < 60°$. POLAR's observing strip appears in the middle of the figure.

$\langle QT \rangle$, which can be used to generate a sky-realization. Figure 10.9 shows a simulation of the polarization-temperature cross-correlation expected for a model with complete reionization at z = 50.

This completes the list of quantities needed to probe the existance of a cosmologically significant detection of polarization-temperature cross-correlation. Once a complete season of data from POLAR is obtained we will begin the process of probing the cross-correlation using a standard likelihood analysis such as that presented in [122].

Chapter 11

Conclusions

We have demonstrated that the detection of the polarization of the CMB is difficult but technologically feasible. A detection would permit the discrimination between heretofore degenerate theoretical predictions. Polarization of the CMB has a unique signature in both real and Fourier space, as well as distinct spectral characteristics. A detection of polarization, in conjunction with the current detections of CMB anisotropy could be the best available probe of the ionization history of the pre-galactic medium. This epoch of cosmic evolution is of great interest, and supplemental information from polarization detection could greatly advance our knowledge of the formation of structure in the early universe. The current generation of anisotropy measurements are sufficiently refined that the fundamental parameters of classical cosmology are beginning to be determined. Detection of polarization of the CMB also promises numerous dividends throughout cosmology, and one readily observes that the status of polarization observations today is reminiscent of the status of anisotropy measurements a decade ago.

"Better is the end of a thing than the beginning thereof." - Ecclesiastes

Bibliography

[1] A. A. Penzias and R. W. Wilson. A measurement of excess antenna temperature at 4080 Mc/s. *ApJ*, 142:419, 1965.

[2] J. C. Mather, D. J. Fixsen, R. A. Shafer, C. Mosier, and D. T. Wilkinson. Calibrator design for the cobe far-infrared absolute spectrophotometer (firas). *ApJ*, 512:511–520, February 1999.

[3] S. Staggs. *Astrophys. Lett. and Comm.*, 32:3, 1995.

[4] E. Wright et al. *ApJ*, 420:1, 1994.

[5] J. C. Mather, E. S. Cheng, D. A. Cottingham, Jr. R. E. Eplee, D. J. Fixsen, T. Hewagama, R. B. Isaacman, K. A. Jensen, S. S. Meyer, P. D. Noerdlinger, S. M. Read, L. P. Rosen, R. A. Shafer, E. L. Wright, C. L. Bennett, N. W. Boggess, M. G. Hauser, T. Kelsall, Jr. S. H. Moseley, R. F. Silverberg, G. F. Smoot, R. Weiss, and D. T. Wilkinson. Measurement of the cosmic microwave background spectrum by the *COBE* FIRAS instrument. *ApJ*, 420:439, 1994.

[6] Smoot, G., "The Cosmic Microwave Background Spectrum" , astro-ph 9705101.

[7] Smoot, G., "The Cosmic Microwave Background Anisotropy Experiments" , astro-ph 9705135.

[8] C. L. Bennett et al. Four-year *COBE* DMR cosmic microwave background observations: Maps and basic results. *ApJ Letters*, 464:L1, 1996.

[9] Barreiro, R., "The Cosmic Microwave Background: State of the Art", astro-ph 9907094.

[10] MAP Satellite Home Page: http://map.gsfc.nasa.gov.

[11] Visit the Planck Surveyor Homepage: http://astro.estec.esa.nl/SA-general/Projects/Planck/planck.html.

[12] N. Caderni, R. Fabbri, B. Melchiorri, F. Melchiorri, and V. Natale. Polarization of the microwave background radiation. i - anisotropic cosmological expansion and evolution of the polarization states. ii - an infrared survey of the sky. *Physical Review D*, 17:1901–1918, April 1978.

[13] Jr. Nanos, G. P. Polarization of the blackbody radiation at 3.2 centimeters. *ApJ*, 232:341–347, September 1979.

[14] G. F. Smoot and P. M. Lubin. Southern hemisphere measurements of the anisotropy in the cosmic microwave background radiation. *ApJ Letters*, 234:L83–L86, December 1979.

[15] P. M. Lubin and G. F. Smoot. Polarization of the cosmic background radiation. *ApJ*, 245:1–17, April 1981.

[16] R. B. Partridge, E. A. Richards, E. B. Fomalont, K. I. Kellermann, and R. A. Windhorst. Small-scale cosmic microwave background observations at 8.4 ghz. *ApJ*, 483:38+, July 1997.

[17] E. J. Wollack, N. C. Jarosik, C. B. Netterfield, L. A. Page, and D. Wilkinson. A measurement of the anisotropy in the cosmic microwave background radiation at degree angular scales. *ApJ Letters*, 419:L49–+, December 1993.

[18] C. B. Netterfield, M. J. Devlin, N. Jarosik, L. Page, and E. J. Wollack. A measurement of the angular power spectrum of the anisotropy in the cosmic microwave background. *ApJ*, 474:47, 1997.

[19] R.B. Partridge. *"3K: The Cosmic Microwave Background Radiation"*. Cambridge University Press, "New York", 1995.

[20] J. Krauss. *"Radio Astronomy"*. Cygnus-Quasar Books, New York, 1982.

[21] A. Kosowsky. *Annals of Phys.*, 246:49, 1996.

[22] Mc Donough and Whalen. *"Detection of Signals In Noise"*. Academic Press, New York, 1995.

[23] R. K. Sachs and A. M. Wolfe. Perturbations of a cosmological model and angular variations of the microwave background. *ApJ*, 147:73+, January 1967.

[24] S. Chandrasekhar. *"Radiative Transfer"*. Dover, New York, 1960.

[25] M. J. Rees. Polarization and spectrum of the primeval radiation in an anisotropic universe. *ApJ Letters*, 153:L1–+, July 1968.

[26] M. M. Basko and A. G. Polnarev. Polarization and anisotropy of the relict radiation in an anisotropic universe. *Monthly Notices of the Royal Astronomical Society*, 191:207–215, April 1980.

[27] J. Negroponte and J. Silk. Polarization of the primeval radiation in an anisotropic universe. *Physical Review Letters*, 44:1433–1437, May 1980.

[28] B. W. Tolman. The polarization of the microwave background in open universes. *ApJ*, 290:1–11, March 1985.

[29] W. Hu, N. Sugiyama, and J. Silk. The physics of microwave background anisotropies. *Nature*, 386:37–43, 1996.

[30] Kosowsky, A., "Introduction to Microwave Background Polarization", astro-ph 9904102.

[31] W. Hu and M. White. A cmb polarization primer. *New Astronomy*, 2:323–344, September 1997.

[32] J. Gunn and B. Peterson. *ApJ*, 142:1633, 1965.

[33] P. J. E Peebles. *Principles of Physical Cosmology*. Princeton Univ. Press, Princeton, NJ, 1993.

[34] L. Ozernoi and V. Chernomordik. *"Sov. Astron."*, 20:260, 1975.

[35] A. K. Gooding, N. Turok, and D. N. Spergel. The formation of galaxies and quasars in a texture-seeded cold dark matter cosmogony. *ApJ Letters*, 372:L5–L8, May 1991.

[36] R. Durrer. Early reionization in cosmology. *astro-ph 9311039*, November 1993.

[37] M. Tegmark, J. Silk, and A. Blanchard. *ApJ*, 420:486, 1994.

[38] M. Tegmark and J. Silk. *ApJ*, 441:486, 1995.

[39] M. Tegmark et al. *ApJ*, 474:1, 1997.

[40] D. J. Fixsen, E. S. Cheng, J. M. Gales, J. C. Mather, R. A. Shafer, and E. L. Wright. The cosmic microwave background spectrum from the full *COBE* FIRAS data set. *ApJ*, 473:576, 1996.

[41] Griffiths, L., et al., "Cosmic Microwave Background Constraints on the Epoch of Reionization", astro-ph 9812125.

[42] J. R. Bond and G. Efstathiou. Cosmic background radiation anisotropies in universes dominated by nonbaryonic dark matter. *ApJ Letters*, 285:L45–L48, October 1984.

[43] J. R. Bond and G. Efstathiou. The statistics of cosmic background radiation fluctuations. *Monthly Notices of the Royal Astronomical Society*, 226:655–687, June 1987.

[44] P. D. Nasel'Skii and A. G. Polnarev. Anisotropy and polarization of the microwave background radiation as a test of nonequilibrium ionization of the pregalactic plasma. *Astrofizika*, 26:543–555, November 1987.

[45] K. Ng and K. W. Ng. Large-angle polarization and anisotropy of the cosmic microwave background radiation and reionization. *ApJ*, 456:413+, January 1996.

[46] M. Zaldarriaga and D. Harrari. Analytic approach to the polarization of the cosmic microwave background in flat and open universes. *Physical Review D*, 52:3276, 1995.

[47] R. Crittenden, R. L. Davis, and P. J. Steinhardt. Polarization of the microwave background due to primordial gravitational waves. *ApJ Letters*, 417:L13–+, November 1993.

[48] R. A. Frewin, A. G. Polnarev, and P. Coles. Gravitational waves and the polarization of the cosmic microwave background. *Monthly Notices of the Royal Astronomical Society*, 266:L21–+, January 1994.

[49] A. G. Polnarev. Polarization and anisotropy induced in the microwave background by cosmological gravitational waves. *A.Zh*, 62:1041–1052, December 1985.

[50] D. Harrari and M. Zaldarriaga. Polarization of the microwave background in inflationary cosmology. *Phys. Lett. B*, 319:96, 1993.

[51] M. Zaldarriaga. Polarization of the microwave background in reionized models. *Physical Review D*, 55:1822, 1997.

[52] U. Seljak and M. Zaldarriaga. A line-of-sight integration approach to cosmic microwave background anisotropies. *ApJ*, 469:437+, October 1996.

[53] M. Zaldarriaga and U. Seljak. An all-sky analysis of polarization in the microwave background. *Physical Review D*, 55:1830, 1997.

[54] E. Newman and R. Penrose. Note on the bondi-metzner-sachs group. *J. Math. Phys.*, 7:863, may 1966.

[55] M. Kamionkowski, A. Kosowsky, and A. Stebbins. Statistics of cosmic microwave background polarization. *Physical Review D*, 55:7368, 1997.

[56] J.D. Jackson. *Classical Electrodynamics*. John Wiley & Sons, 1975.

[57] M. Zaldarriaga. *Fluctuations in the Cosmic Microwave Background*. PhD dissertation, Massachusetts Institute of Technology, 1998.

[58] R. H. Dicke. The measurement of thermal radiation at microwave frequencies. *Rev. Sci. Instr.*, 17, July 1946.

[59] K. Rohlfs. *"Tools of Radio Astronomy"*. Springer Verlag, New York, 1996.

[60] A. Thompson et al. *"Interferometry and Synthesis in Radio Astronomy"*. Krieger Publishing Co., Malabar, 1998.

[61] K. Fujimoto. On the correlation radiometer technique. *IEEE-MTT*, 1:203, 1964.

[62] D. Johnson. *Absolute Thermodynamic Temperature of the Cosmic Microwave Background Radiation Temperature at 24.8 GHz*. PhD dissertation, Princeton University, 1986.

[63] E. Cheng. *Large Scale Anisotropy Of The 3K Cosmic Microwave Background Radiation at 24.8, 31.4, and 46.0 GHz*. PhD dissertation, Princeton University, 1983.

[64] P. T. Timbie and D. T. Wilkinson. A search for anisotropy in the cosmic microwave radiation at medium angular scales. *ApJ*, 353:140–144, April 1990.

[65] S. Staggs. *An Absolute Measurement of the Cosmic Microwave Background Radiation Temperature at 1.4 GHz*. PhD dissertation, Princeton University, 1993.

[66] P. M. Lubin. *Polarization of the cosmic background radiation*. PhD thesis, California Univ., Berkeley., 1980.

[67] P. Lubin, P. Melese, and G. Smoot. Linear and circular polarization of the cosmic background radiation. *ApJ Letters*, 273:L51–L54, October 1983.

[68] C. B. Netterfield, N. Jarosik, L. Page, D. Wilkinson, and E. Wollack. The anisotropy in the cosmic microwave background at degree angular scales. *ApJ Letters*, 445:L69, 1995.

[69] E. J. Wollack, M. J. Devlin, N. Jarosik, C. B. Netterfield, L. Page, and D. Wilkinson. An instrument for investigation of the cosmic microwave background radiation at intermediate angular scales. *ApJ*, 476:440+, February 1997.

[70] J. Tinbergen. *"Astronomical Polarimetry"*. Cambridge University Press, New York, 1997.

[71] A.D. Olver, P.J.B. Clarricoats, A.A. Kishk, and L. Shafai. *Microwave Horns and Feeds*. The Institution of Electrical Engineers, London, UK, and the Institute of Electrical and Electronics Engineers, Inc. USA, 1994.

[72] X. Zhang. Design of conical corrugated feed horns for wide-band high-frequency applications. *IEEE Trans. on Microwave Theory and Techniques*, 41(8), August 1993.

[73] M. Janssen et al. *IEEE Trans. Ant. and Prop.*, 27:551, 1979.

[74] R.J. Wylde and D.H. Martin. Gaussian beam-mode analysis and phase-centers of corrugated feed horns. *IEEE Trans. on Microwave Theory and Techniques*, 41(10), 1993.

[75] G. Wilson. *An Instrument and Technique for Measuring Anisotropy of the CMBR*. PhD dissertation, Brown University, 1997.

[76] G.L. James. Design of wide-band compact corrugated horns. *IEEE Trans. on Antennas and Propagation*, AP-32(10), October 1984.

[77] B.M. Thomas, G.L. James, and K.J. Greene. Design of wide-band corrugated conical horns for cassegrain antennas. *IEEE Trans. on Antennas and Propagation*, AP-34(6), June 1986.

[78] E. Wollack. A full waveguide band orthomode junction. *NRAO Electronics Division Internal Report*, 303:1, may 1996.

[79] J. Pyle and R. Angley. Cutoff wavelengths of waveguides with unusual cross sections. *IEEE MMT*, 12-9:556–557, 1964.

[80] G. Chattopadhyay et al. *"IEEE Microwave and Guided Wave Letters"*, 1998.

[81] J. Faris. Sensitivity of correlation radiometer. *J. of Res. of the NBS - C. Eng. and Instr.*, 71C:153, 1966.

[82] S.A. Maas. *"Microwave Mixers"*. Artech House, London, 1993.

[83] B. Femenia, R. Rebolo, C. M. Gutierrez, M. Limon, and L. Piccirillo. The instituto astrofisica de canarias-bartol cosmic microwave background anisotropy experiment: Results of the 1994 campaign. *ApJ*, 498:117+, May 1998.

[84] J. W. Dreher, C. L. Carilli, and R. A. Perley. The faraday rotation of cygnus a - magnetic fields in cluster gas. *ApJ*, 316:611–625, may 1987.

[85] A. Gasiewski and D. Kunkee. Calibration and applications of polarization-correlating radiometers. *IEEE Trans.MTT*, 41:767, may 1993.

[86] T.S. Chu et al. Quasi-optical polarization diplexing of microwaves. *Bell System Technical Journal*, 54:1665, dec 1975.

[87] David Wilkinson. A warning label for cosmic microwave background anisotropy experiments. In A. Astbury et al., editors, *"Particle Physics and Cosmology, Proceedings of the Ninth Lake Louise Winter Institute"*, page 110, Singapore, 1995. World Scientific.

[88] A. Kogut, A. J. Banday, C. L. Bennett, K. M. Gorski, G. Hinshaw, P. D. Jackson, P. Keegstra, C. Lineweaver, G. F. Smoot, L. Tenorio, and E. L. Wright. Calibration and systematic error analysis for the cobe dmr 4 year sky maps. *ApJ*, 470:653+, October 1996.

[89] W. N. Brandt, C. R. Lawrence, A. C. S. Readhead, J. N. Pakianathan, and T. M. Fiola. Separation of foreground radiation from cosmic microwave background anisotropy using multifrequency measurements. *ApJ*, 424:1, 1994.

[90] G. Rybicki and A. Lightman. *"Radiative Processes in Astrophysics"*. Wiley, New York, 1979.

[91] S. Cortiglioni and T. A. T. Spoelstra. The limitations of cosmic-microwave-background measurements due to linear polarization of galactic radio emission. *Astronomy and Astrophysics*, 302:1+, October 1995.

[92] W. Brouw and T. Spoelstra. Linear polarization of the galactic background at frequencies between 408 and 1411 mhz. *Astronon. and Astrophys. Supp.*, 26:129, 1976.

[93] C. L. Bennett, G. F. Smoot, G. Hinshaw, E. L. Wright, A. Kogut, G. De Amici, S. S. Meyer, R. Weiss, D. T. Wilkinson, S. Gulkis, M. Janssen, N. W. Boggess, E. S. Cheng, M. G. Hauser, T. Kelsall, J. C. Mather, S. H. Moseley, T. L. Murdock, and

R. F. Silverberg. Preliminary separation of galactic and cosmic microwave emission for the *COBE* differential microwave radiometer. *ApJ Letters*, 396:L7, 1992.

[94] A. Kogut, A. J. Banday, C. L. Bennett, K. Górski, G. Hinshaw, G. F. Smoot, and E. L. Wright. Microwave emission at high galactic latitudes in the four-year DMR sky maps. *ApJ Letters*, 464:L5, 1996.

[95] Lyman Spitzer. *"Physical Processes in the Interstellar Medium"*. Wiley Classics Library, New York, 1978.

[96] E. L. Wright, J. C. Mather, C. L. Bennett, E. S. Cheng, R. A. Shafer, D. J. Fixsen, Jr. Eplee, R. E., R. B. Isaacman, S. M. Read, N. W. Boggess, S. Gulkis, M. G. Hauser, M. Janssen, T. Kelsall, P. M. Lubin, S. S. Meyer, Jr. Moseley, S. H., T. L. Murdock, R. F. Silverberg, G. F. Smoot, R. Weiss, and D. T. Wilkinson. Preliminary spectral observations of the galaxy with a 7 deg beam by the cosmic background explorer (cobe). *ApJ*, 381:200–209, November 1991.

[97] E. M. Leitch, A. C. S. Readhead, T. J. Pearson, and S. T. Myers. An anomalous component of galactic emission. *ApJ Letters*, 486:L23–+, September 1997.

[98] B. T. Draine and A. Lazarian. Diffuse galactic emission from spinning dust grains. *ApJ Letters*, 494:L19–+, February 1998.

[99] B. T. Draine and A. Lazarian. Magnetic dipole microwave emission from dust grains. *ApJ*, 512:740–754, February 1999.

[100] D. Sakia and C. Salter. *AAR&A*, 26:93, 1988.

[101] A. Franceschini, L. Toffolatti, L. Danese, and G. De Zotti. Discrete source contributions to small-scale anisotropies of the microwave background. *ApJ*, 344:35–45, 1989.

[102] H. Liebe. *"Radio Science"*, 16:1183, 1981.

[103] Brenden Crill, Senior Thesis, Brown University , 1995.

[104] Rosencranz, P.W. 1994, personal communication.

[105] P. Rosencranz and D. Staelin. *Radio Science*, 25:721, 1988.

[106] S. Dodelson. Determining cosmic microwave background anisotropies in the presence of foregrounds. *ApJ*, 482:577+, June 1997.

[107] B. Keating, P. Timbie, A. Polnarev, and J. Steinberger. Large angular scale polarization of the cosmic microwave background radiation and the feasibility of its detection. *ApJ*, 495:580+, 1998.

[108] O. P. Lay and N. W. Halverson. "the impact of atmospheric fluctuations on degree-scale imaging of the cosmic microwave background". *astro-ph 9905369*, May 1999.

[109] S. E. Church. Predicting residual levels of atmosphereic sky noise in ground based observations of the cosmic microwave background radiation. *Monthly Notices of the Royal Astronomical Society*, 272:551–569, February 1995.

[110] M. White and M. Srednicki. Window functions of cosmic microwave background experiments. *ApJ*, 443:6–10, April 1995.

[111] L. Knox. Cosmic microwave background anisotropy observing strategy assessment. *ApJ*, 480:72+, May 1997.

[112] W. H. Press, S. A. Teukolsky, W. T. Vetterling, and B. P. Flannery. *Numerical Recipes in FORTRAN: The Art of Scientific Computing*. Cambridge Univ., Cambridge, 2nd edition, 1992.

[113] M. W. Pospieszalski, W. J. Lakatosh, L. D. Nguyen, M. Lui, T. Liu, M. Le, M. A. Thompson, and M. J. Delaney. Cryogenically-cooled hfet amplifiers and receivers: State-of-the-art and future trends. In L. Kirby, editor, *1992 IEEE MTT-S Digest*, page 1369, Piscataway, NJ, 1992. IEEE.

[114] M. W. Pospieszalski, W. J. Lakatosh, L. D. Nguyen, M. Lui, T. Liu, M. Le, M. A. Thompson, and M. J. Delaney. Q and E-band cryogenically-coolable amplifiers using AlInAs/GaInAs/InP hemts. In L. Kirby, editor, *1995 IEEE MTT-S Digest*, page 1121, Piscataway, NJ, 1995. IEEE.

[115] U. Seljak. Measuring polarization in the cosmic microwave background. *ApJ*, 482:6+, June 1997.

[116] R. Crittenden, D. Coulson, and N. Turok. *Physical Review D*, 52:r5402, 1995.

[117] D. Coulson, R. Crittenden, and N. Turok. *Phys. Rev. Lett.*, 73:2390, 1994.

[118] K. Ng and K. W. Ng. Gravity wave-induced polarization of the cosmic microwave background radiation. *ApJ*, 445:521–525, June 1995.

[119] R. Darling. *"Differential Forms and Connections"*. Cambridge University Press, New York, 1995.

[120] G. F. Smoot et al. Structure in the *COBE* differential microwave radiometer first-year maps. *ApJ Letters*, 396:L1, 1992.

[121] Smoot, G., "Summary of Results from COBE", astro-ph 9902027.

[122] A. C. S. Readhead, C. R. Lawrence, S. T. Myers, W. L. W. Sargent, and H. E. Hardebeck. *ApJ*, 346:566, 1989.